



Università degli studi di Pisa

DIPARTIMENTO DI FISICA 'E. FERMI'

TESI DI LAUREA MAGISTRALE IN FISICA

**Strain engineering of germanium surface states:
an ab-initio study**

Candidato
Francesco Macheda

Relatore
Prof. Giuseppe Grosso

Contents

Introduction	7
1 Geometrical structure of bulk germanium and of the (001)-(2x1) germanium surface	13
1.1 Ge bulk geometry	13
1.2 Ge (0, 0, 1) surface geometry	17
2 Ab-initio evaluation of the electronic band structure	25
2.1 Introduction	25
2.2 Density Functional one-electron Hamiltonian	26
2.3 Self-consistent solution of the Kohn-Sham equations	28
2.4 Exchange-correlation functionals and pseudopotential approximations	29
2.5 Solution of Kohn-Sham equations with localized basis functions	35
2.6 Solution of Kohn-Sham equations with plane waves basis functions	37
2.7 Special \mathbf{k} points and Monkhorst-Pach method	39
2.8 Surface band structure calculation	42
3 Ab-initio methods for geometric structure optimization	47
3.1 Internal coordinates	47
3.2 Adiabatic approximation	48
3.3 Optimization Method	49

4 Structural and electronic properties of bulk germanium crystal	53
4.1 Introductory considerations	53
4.2 Ab-initio calculation of Ge bulk structural and electronic properties	55
5 Structural and electronic properties of the (2x1)-(001) germanium surface	63
5.1 Introductory consideration	63
5.2 Ge-(001) surface properties	65
5.3 Preliminary study of the 5 layers germanium slab	66
5.4 Quantitative study of the 12-layers germanium slab	71
6 Theory of elastic deformations in crystals	77
6.1 Strain tensor	77
6.2 Stress tensor	79
6.3 Stress-strain relation	80
6.3.1 Application of elasticity theory to solids	81
6.4 Ab-initio computation of the Ge bulk elastic compliance moduli tensor	84
7 Strained Ge bulk crystal	85
7.1 Introductory considerations	85
7.2 Tetragonal cell choice for surface description	86
7.2.1 Elastic compliance tensor calculation	87
7.2.2 Hydrostatic strain on bulk Ge	91
7.2.3 Biaxial strain on Ge bulk	93
7.2.4 Uniaxial In-Plane Strain on Ge bulk	95
8 Strained Ge-(001) surface	99
8.1 Introductory considerations	99
8.2 In plane (X, Y) biaxial strained p(2x1) Ge (001) surface	99

8.3 Uniaxial strain along Y direction on p(2x1) Ge (001) surface	109
Conclusions and outlook	115
Bibliography	120

Introduction

Nanostructures have received growing interests in the last decade as consequence of their peculiar and fascinating properties, and applications often superior to their bulk counterparts. In the last few years surfaces and interfaces strongly influenced the electronic properties of semiconductor nanostructures, often revealing to be the dominant factor. Nanomembranes (NMs) [1] provide the opportunity for such quantitative investigations; they are two-dimensional crystalline films that can be shaped with precise surface orientations and sizes (lateral dimensions, thickness, defect-control).

In this perspective, among the most intriguing and frequently studied surfaces we find the semiconductor group IV (001) surfaces. These surfaces are produced by the termination of the diamond crystalline structure along the [001] crystallographic direction. Because of its technological importance, the majority of studies have been devoted to the silicon Si(001) surface rather than to the closely related germanium Ge(001) surface [2]. Nonetheless, heterostructures consisting of alternate Ge and Si layers grown on Si, Si-Ge waveguide design with Ge working as a signal amplifier, Ge detectors, Ge quantum dots-based light emitting devices and Ge lasers have received much attention in the last decade [3]. These germanium and silicon-germanium structures enable the creation of an entirely new class of materials based on modulated band-gap engineering; this motivates the detailed study of the Ge bulk and surface properties (with particular attention to the (001) surface). The present work connects with this widespread focus on two dimensional materials, with the aim of working out a novel understanding of the electronic band-gap engineering of the (2x1)-reconstructed Ge(001) surface, by means of ab-initio density functional theory techniques.

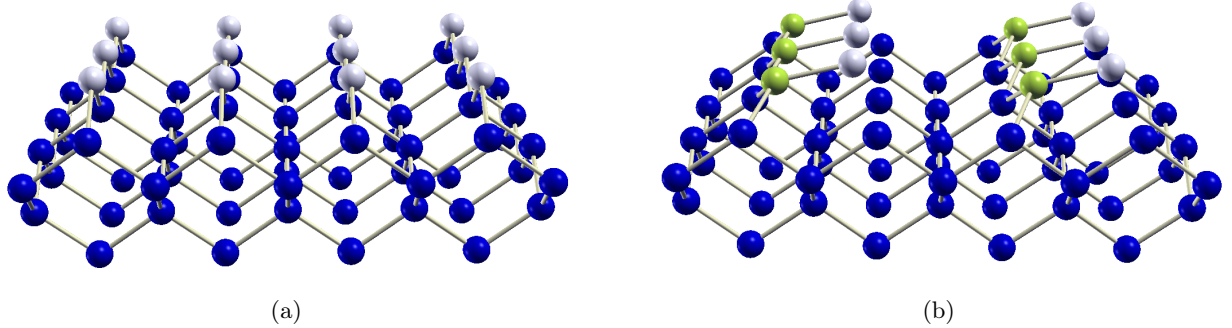


Figure 1: Schematic representation of the (a) ideal and of the (b) asymmetric dimer (2x1) Ge (001) reconstructed surface with the surface atoms coloured in light grey and light green. In the (2x1) reconstruction the Ge surface atoms are pulled together to form asymmetric dimers. In (b) light grey atoms are nearer to the surface than the yellow ones.

The truncation of the Ge crystalline structure along the [001] direction generates the (001)-oriented surface of germanium; at room temperature, this (ideal) surface is energetically unstable so that a process of atomic rearrangement occurs which leads to (2x1) reconstructions [4], where (2x1) means that the surface periodicity is doubled along the [110] or the [$\bar{1}10$] crystallographic directions. In fact, on ideally-terminated (001) surfaces of the diamond lattice, each surface atom exhibits two dangling bonds, partly occupied. The process of formation of dimers on the (001)-oriented surfaces of solids with the diamond structure is driven by the reduction of the number of dangling bonds by a factor of two (due to the formation of a chemical bond between neighbour Ge surface atoms) and thus by lowering the electronic energy of such surfaces. If no further relaxations occurs (i.e. if the process of dimerization is symmetric with respect to the two surface atoms) both dimer atoms would be equivalent and their dangling bonds would be partly occupied by one electron. Indeed, the dimers will spontaneously deform to lower their symmetry implying the degeneracy removal of the dangling bonds at the dimer atoms [5]. With dimers, asymmetry is most easily achieved by a simple tilt with respect to the surface plane. Such relaxations are accompanied by re-hybridization of the surface bonds and, as a consequence, a rearrangement of surface charge. Experimental investigations (by means of low-energy electrons [6],

high-energy electrons [7], surface core-level photoelectrons [8], X-rays [9] and many other experimental techniques) and total energy minimization calculations ([10, 11, 12]) indeed confirmed that the untilted dimers are energetically unstable. It is also experimentally acknowledged that the dimer-induced geometric perturbation of the ideal Ge surface, penetrates up to the fourth layer below the surface, confirming theoretical calculations [13].

The surface and the successive rearrangements of surface atoms leads to a change of the electronic band structure from the bulk material. Therefore, electronic surface-localized states may exist at the semiconductor surface. The energies of these surface states may occur in the bulk energy forbidden zone, in which case they are generally damped into the bulk region [14], but surface state can be also resonant with the bulk states. Occupied and empty surface states of the (2x1)-reconstructed Ge (001) surface were mostly studied by using angle resolved photoemission [15, 16, 17], angle resolved inverse photoemission [18] and scanning tunneling microscopy [19, 20], provided that a preliminary polishing of the surface is realized, for example, by means sputtering with argon atoms and annealing in ultra-vacuum conditions [21]. For the unstrained Ge (001) surface, the detected bands of occupied surface states are overlapping the top of bulk valence bands, giving rise to surface states lying -0.6eV and -1.3eV under the Fermi level [16, 19].

For two-dimensional, as well as for three-dimensional bulk crystalline materials, a wide family of performances can be tuned by strain-engineering, i.e., varying structural parameters by tensile or compressive stress [22]. Under this perspective, many efforts have been addressed to the study of strain effects on the three-dimensional Si and Ge bulk structures, whereas less literature has been produced for the corresponding (001) surfaces. It is known, by a wide experimental and theoretical investigation, that Si and Ge bulk electronic properties can be tuned (within a well defined range) as consequence of modification of structural configurations due to strain application [23, 24, 25, 26, 27, 28]. For instance, at the state of art it is widely accepted that the Ge bulk crystal electronic band structure dramatically changes when exposed to strains; in particular, in absence of strain, the minimum of the conduction band and the maximum of the valence bands of the electronic band structure occurs at

different electronic crystal momenta. On the contrary, as we will reproduce within our calculations, the position of the conduction minimum and of the valence maximum occurs at the same electronic crystal momentum under the application of more than 1.7% tensile biaxial strain orthogonal to the [001] direction. This example of band-engineering of the electronic energy gap has a lot of implications on the light emission and on the population inversion properties of the Ge crystal. Even if it is experimentally hard to achieve strain conditions (such as around 2% biaxial tensile strain) for the Ge crystal because of the easy birth of cracks and dislocations in the sample, the realization of Ge nanomembranes has overcome the traditional experimental limits, pushing the values of applicable strain to values never reached before [1]. As regards band-gap engineering for the Si (001) surface, numerical evidence of complete isolation of the surface states via tensile strain has been recently found in the work by Zhou et al. [29]. For the Ge (001) surface instead, no work has been produced up to now in this direction. This lack of results, in conjunction with the (above mentioned) technological allure of Ge crystal and Ge nanomembranes properties, has lead our attention to the ab-initio investigation of the electronic and structural properties of the Ge (001) surface in strained conditions.

Ab-initio techniques and simulations have revealed to be invaluable tools to investigate crystalline structures (three or low-dimensional), interpret experimental measurements, give fundamental support in many solid state physics fields and design new devices, also due to the everlasting increase of computational capabilities. In the present thesis we make use of DFT ab-initio numerical techniques (to which chapter 2 and chapter 3 are dedicated) by means of two computational codes, namely QUANTUM ESPRESSO [30] and CRYSTAL14 [31], respectively built for plane-waves and localized Gaussian orbitals calculations. In order to study the effects of strain (presented in chapter 6) on the structural and electronic properties of the Ge (001) surface we found necessary to start from the study of the Ge bulk crystal, under relaxed or strained conditions (chapter 4 and 7), and of the unstrained Ge (001) surface (chapter 5). These steps are necessary to rightly tune (by comparison with experimental results) the choices of the pseudopotential, of the exchange-correlation functionals and of the whole of the computational parameters and working procedures to be finally used in the study of the strained Ge

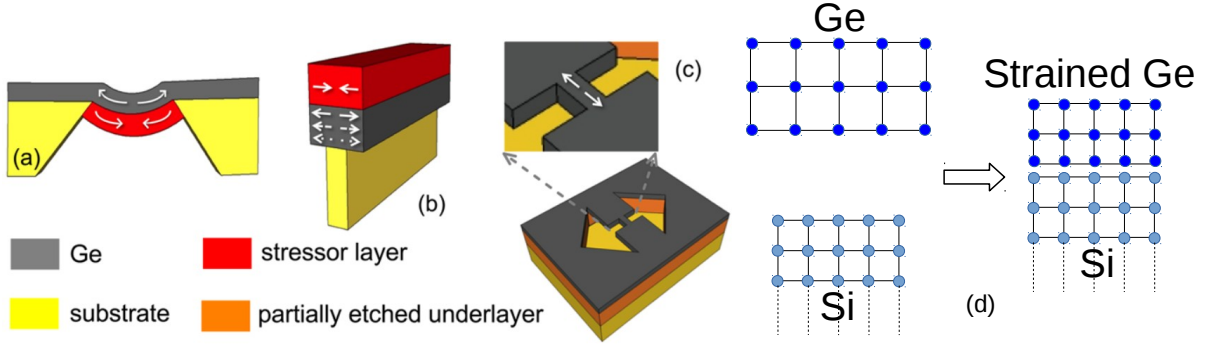


Figure 2: Schematic illustrations of the use of stressor layers to introduce tensile strain in Ge. (a) Cross-sectional image of the geometry used to obtain nominally biaxial tensile strain in an edge-clamped suspended Ge film. (b) Three-dimensional view of the uniaxially strained Ge photonic wires. (c) Uniaxially strained Ge microbridge geometry. In all figures, the arrows pointing outward (inward) indicate tensile (compressive) strain. [1] The solid, dashed, and dotted arrows in (b) indicate regions of progressively weaker tensile strain. (d) Schematic representation of the epitaxial deposition process of Ge atoms (blue dots) on a Si substrate (light blue dots) used to obtain biaxial compressive strain on the Ge crystal due to lattice mismatch. To obtain tensile strain, a substrate of Sn is often used.

(001) surface. For instance, despite of the Ge bulk apparent structural simplicity, we will show in chapter 4 that typical density functional exchange-correlation potentials fail to predict the equilibrium configuration and the electronic properties of the Ge crystal, leading instead to unphysical metallic behaviour. Thus we will need to implement some heavier formulation of the exchange-correlation potential capable of taking in account properly the electronic delocalization effects [32, 33], namely hybrid functionals and in particular the screened HSE06 functional [34, 35, 36]. This powerful numerical machinery, able to reproduce well the experimental data of the Ge bulk, presents the drawback of lengthy simulations and some technical limitation as regards its implementation in the computational codes, especially in the perspective of extending our calculations to the Ge (001) surface. Therefore, in this thesis we will present, also a suitable working procedure to reduce the simulation time and at the same time maintain the precision of the numerical results. Another important topic is that, when

dealing with the (2x1) reconstruction of the Ge (001) surface in relaxed or strained conditions, we will have to discuss how many atomic layers are necessary to simulate a surface (which is, in principle, a semi-infinite succession of planes) and which is the sensitivity of the simulation to the number of layers implemented, together with the question on how efficiently terminate the finite succession of planes in order to mimic the presence of the underlying bulk without affecting too much the rapidity of the simulation. This topic will be studied in the case of the unstrained (2x1) Ge (001) surface in chapter 5.

Once determined the best working strategy, we have studied in chapter 8 the effects of the strain, both in biaxial or uniaxial form, on the structural and electronic properties of the (2x1) Ge (001) surface, focusing the attention on the behaviour of the surface dimer bond length and angle, and on the electronic band structure with particular attention on the discovery of surface states. We will find that complete isolation of (2x1) Ge (001) valence band surface states occurs for values below -0.5% of in plane (compressive) strain, allowing opportunities for surface band-gap modulation and opening the door to surface transport separated from bulk transport. A wider overview on these and other future developments of this works is presented in the conclusions to this thesis.

Chapter 1

Geometrical structure of bulk germanium and of the (001)-(2x1) germanium surface

1.1 Ge bulk geometry

Germanium is a group IV semiconductor element. Its atomic number is 32 and the basic electronic configuration is $1s^2 2s^2 2p^6 3s^2 3p^6 3d^{10} 4s^2 4p^2$. It is well known that due to the sp^3 hybridization of 4s and 4p-orbitals, the single Ge atom in bulk crystal is surrounded by four Ge atoms in the tetrahedral diamond structure. We are now going to describe this structure.

The description of the pattern of a crystal structure requires the definition of primitive cell vectors $\mathbf{t}_i, i = 1, 2, 3$ (and whenever there is more than one atom per primitive cell, also of basis vectors \mathbf{d}_ν). The primitive cell is in fact defined as that elementary region whose repetition generates the whole lattice by translation operations; it contains one or more atoms depending on the simple or the composite structure of the crystal. More precisely, for a simple (Bravais) lattice, any vector joining the origin to a specific point of the lattice can be written as a linear superposition with integer coefficients of the primitive cell vectors. Sometimes it is also useful to display the so-called conventional cell, which contains an integer number of primitive cells and more atoms. The choice of the primitive cell is not

unique, provided that we keep the same volume. For the diamond structure we choose the following vectors:

$$\begin{aligned}\mathbf{t}_1 &= \frac{a}{2}(0, 1, 1), \mathbf{t}_2 = \frac{a}{2}(1, 0, 1), \mathbf{t}_3 = \frac{a}{2}(1, 1, 0) \\ \mathbf{d}_1 &= (0, 0, 0), \mathbf{d}_2 = \frac{a}{4}(1, 1, 1)\end{aligned}\quad (1.1)$$

where for Ge crystal $a = 5.65791\text{\AA}$ [37] and $\mathbf{t}_1, \mathbf{t}_2, \mathbf{t}_3$ represent the primitive vectors of the lattice while $\mathbf{d}_1, \mathbf{d}_2$ represent the basis vectors which indicate the positions of the atoms in the primitive cell. The volume of the primitive cell is $\Omega = \mathbf{t}_1 \cdot (\mathbf{t}_2 \wedge \mathbf{t}_3) = \frac{a^3}{4} = 181.12\text{\AA}^3$. We show in Figure 1.1 the primitive cell (shaded zone) for the Ge crystal and a most used conventional cubic cell:

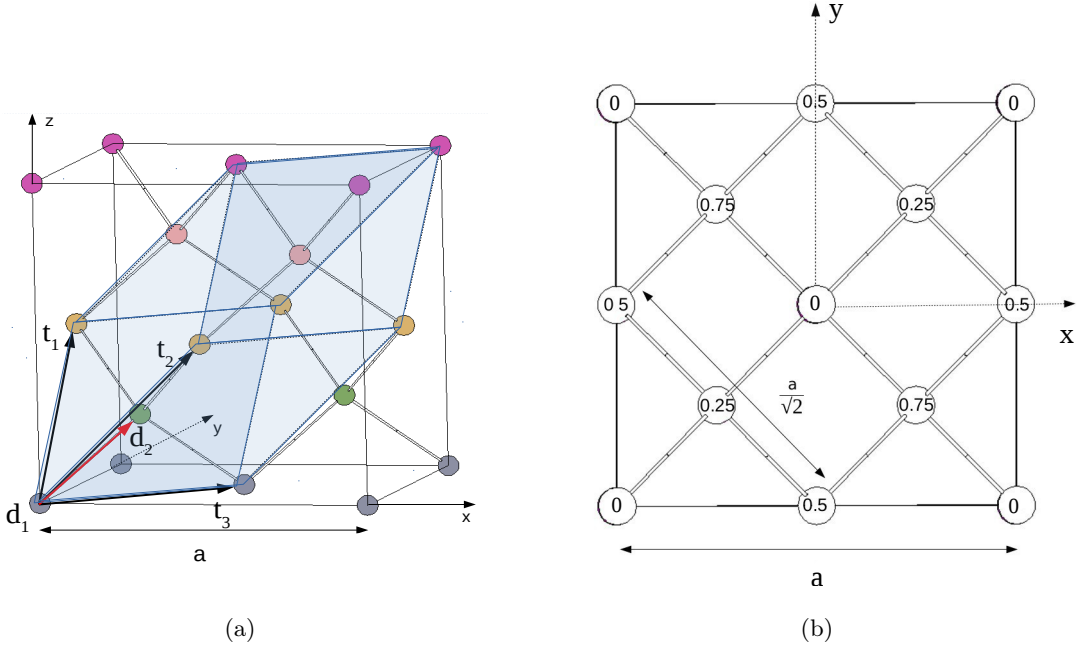


Figure 1.1: Ge conventional cell. a) Side view. Different colours indicate different atomic heights along z axis: blue at $z=0$, green at $z=\frac{a}{4}$, yellow at $z=\frac{a}{2}$, pink at $z=\frac{3a}{4}$. The plane at $z=a$ is equivalent to the plane at $z=0$. The light blue shaded zone is the primitive Ge cell. b) Top-view. In each circle the number indicates the z coordinate of the atom in the cell, in units of a . The origin of the reference system (x, y) has been shifted with respect to a) for convenience.

The primitive cell contains 2 Ge atoms while the conventional cell contains 8 atoms. It is really important to classify the number of neighbours surrounding one given atom depending on their distance. For

instance, in diamond structure the distance between an atom and its 4 first neighbours is $\frac{a}{4}\sqrt{3} = 2.445\text{\AA}$. The distance with the 12 second neighbours is $\frac{a}{2}\sqrt{2} = 3.993\text{\AA}$ and so on. This classification is important because, as we will see in the following sections, it is relevant to interpret of how many and how strong interactions act on a single atom. When dealing with periodic structures, in addition to the Bravais direct lattice, we need to describe its reciprocal lattice. To define it, we consider three vectors $\mathbf{g}_1, \mathbf{g}_2, \mathbf{g}_3$ which satisfy the following relation:

$$\mathbf{t}_i \cdot \mathbf{g}_j = 2\pi\delta_{ij} \quad (1.2)$$

where the factor 2π is introduced as a matter of convenience. In our case, from the vectors reported in equation (1.1), we have the following primitive vectors of the reciprocal lattice:

$$\mathbf{g}_1 = \frac{2\pi}{a}(-1, 1, 1), \mathbf{g}_2 = \frac{2\pi}{a}(1, -1, 1), \mathbf{g}_3 = \frac{2\pi}{a}(1, 1, -1). \quad (1.3)$$

The points of the reciprocal lattice are obtained as a linear combination with integer coefficients of the vectors of equation (1.3). Notice that the reciprocal lattice is related only to the translational properties of the crystal and not to the basis. The first Brillouin Zone is the Wigner-Seitz cell of the reciprocal lattice, i.e. it is defined as that region of points which are closer to a chosen lattice point (say the origin) than to any other. The first Brillouin zone can be obtained by bisecting with perpendicular planes nearest neighbours reciprocal lattice vectors; successive order of Brillouin zones are similarly obtained in terms of second nearest neighbours (and other orders of neighbours if necessary), and considering the smallest volume enclosed. For the diamond Ge structure, the first Brillouin Zone is the truncated octahedron shown in Figure 1.2. Since we will study a surface of the Ge crystal with given orientation, it is convenient to describe the bulk crystal with a conventional cell useful for the successive description of the given surface. In our case we use the conventional tetragonal cell shown by the shaded region in Figures 1.4 and 1.3, which evidences the planes orthogonal to the [0 0 1] direction. This cell includes 4 Ge atoms, and its volume is twice the volume of the primitive cell. We define the new lattice vectors:

$$\begin{aligned} \mathbf{w}_1 &= \frac{a}{2}(1, -1, 0), \mathbf{w}_2 = \frac{a}{2}(1, 1, 0), \mathbf{w}_3 = a(0, 0, 1) \\ \mathbf{b}_1 &= (0, 0, 0), \mathbf{b}_2 = \frac{a}{4}(1, 1, 1), \mathbf{b}_3 = \frac{a}{4}(2, 0, 2), \mathbf{b}_4 = \frac{a}{4}(1, -1, 3). \end{aligned} \quad (1.4)$$

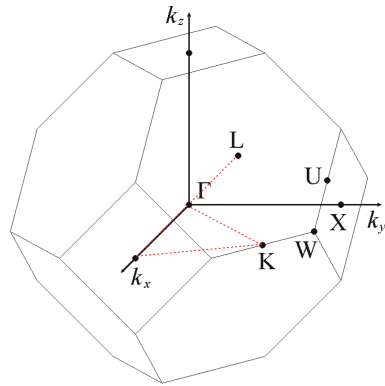


Figure 1.2: First Brillouin zone of Ge crystal with the \mathbf{k} -points and \mathbf{k} -lines that will be used in the following chapters to calculate the Ge bulk electronic band structure. Some high-symmetry points are indicated: $\Gamma = 0$, $X = \frac{2\pi}{a}(1, 0, 0)$, $L = \frac{\pi}{a}(1, 1, 1)$, $W = \frac{2\pi}{a}(\frac{1}{2}, 1, 0)$, $K = \frac{3\pi}{2a}(1, 1, 0)$, $U = \frac{2\pi}{a}(\frac{1}{4}, 1, \frac{1}{2})$.

We also define, for convenience, a new Cartesian reference system, (X, Y, Z) , rotated anti-clockwise by 45° around the z -axis with respect to the (x, y, z) reference system.

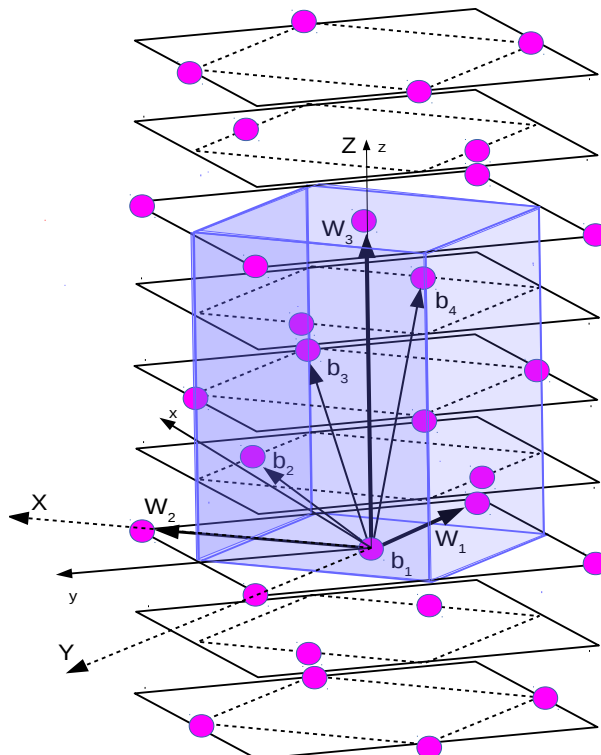


Figure 1.3: Side view of the Ge bulk tetragonal conventional cell (in blue shaded colour) evidencing the atomic planes orthogonal to the $[0 0 1]$ direction.

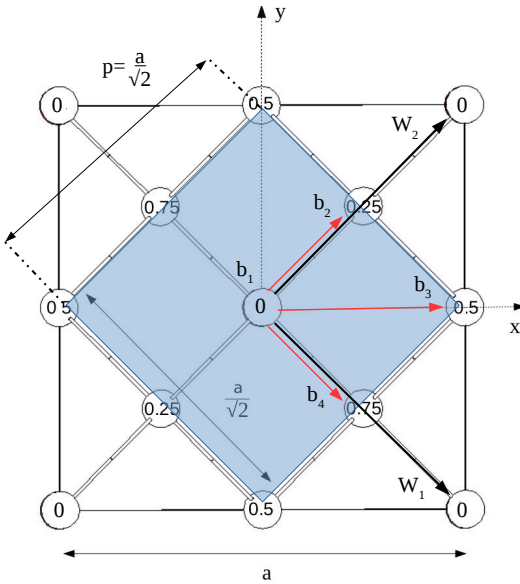


Figure 1.4: Top view of the Ge bulk tetragonal conventional cell.

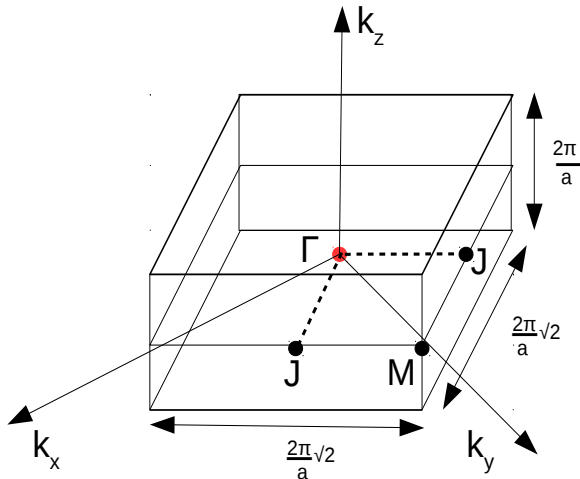


Figure 1.5: First Brillouin Zone of the Ge bulk tetragonal cell defined in Figures 1.3 and 1.4.

1.2 Ge (0, 0, 1) surface geometry

To investigate the surface properties of germanium, it is first useful to describe its bulk geometry along a specific direction. When we refer to a specific surface orthogonal to the [0 0 1] direction, we mean the lattice plane (001) orthogonal to that direction. The aim of this section is to first present the

ideal semi-infinite (001) surface geometry of germanium and then to discuss its modification from the ideal-cut structure.

Dimerization of the surface Ge atoms

If we cut a slab of germanium from an ideal infinite bulk crystal, orthogonally to the [0 0 1] direction, we obtain the geometry which can be described starting from Figures 1.4 and 1.3. If we just consider the top (surface) atoms, we see that the surface cell is a square lattice of parameter $a' = \frac{a}{\sqrt{2}} = 3.993\text{\AA}$, rotated anti-clockwise by 45° with respect to the cartesian plane (x, y). The area of the surface square cell is 15.92\AA^2 . The surface reciprocal lattice is a square lattice itself, as we will see in next section. When dealing with real surfaces we have to consider that each of the top surface Ge atoms has two covalent bonds saturated with atoms in the bulk and two dangling bonds with one electron in each. It is found that this structure is energetically unstable so that, in order to lower the total energy of the system, the surface Ge atoms go through a process of reconstruction, i.e. neighbouring Ge atoms approach towards one another forming a chemical bond. This leads to a "reconstruction" of the surface cell, with different periodicity. The coupling of the surface atoms is named "dimerization". Dimerization of surface atoms in germanium (as in silicon) has been first proposed in the late 1950's by Schlier and Farnsworth [4], based on low energy electron diffraction (LEED) measurements. The first imaging in real-space was obtained with scanning tunneling microscopy in the mid of 1980s by Tromp et al. [38]. The driving force for this dimerization is the reduction in the number of dangling bonds from two to one per surface atom. The conformation of this distortion may be symmetric or asymmetric with respect to the two Ge atoms. In fact, the two Ge atoms can group together maintaining the same z coordinate (symmetric distortion) or it may happen that one atom is nearer to the surface than the other (asymmetric distortion). The symmetry of the distortion has been longly debated, but eventually it was realized ([39, 40, 41]) that the asymmetric (buckled) configuration is observed experimentally.

Isolating the two top planes of Figure 1.4 containing the dimer atom, we show the arrangement of the asymmetric dimerization effect for the simplest (2x1) reconstruction of the Ge surface in Figures

1.6 (a) and (b).

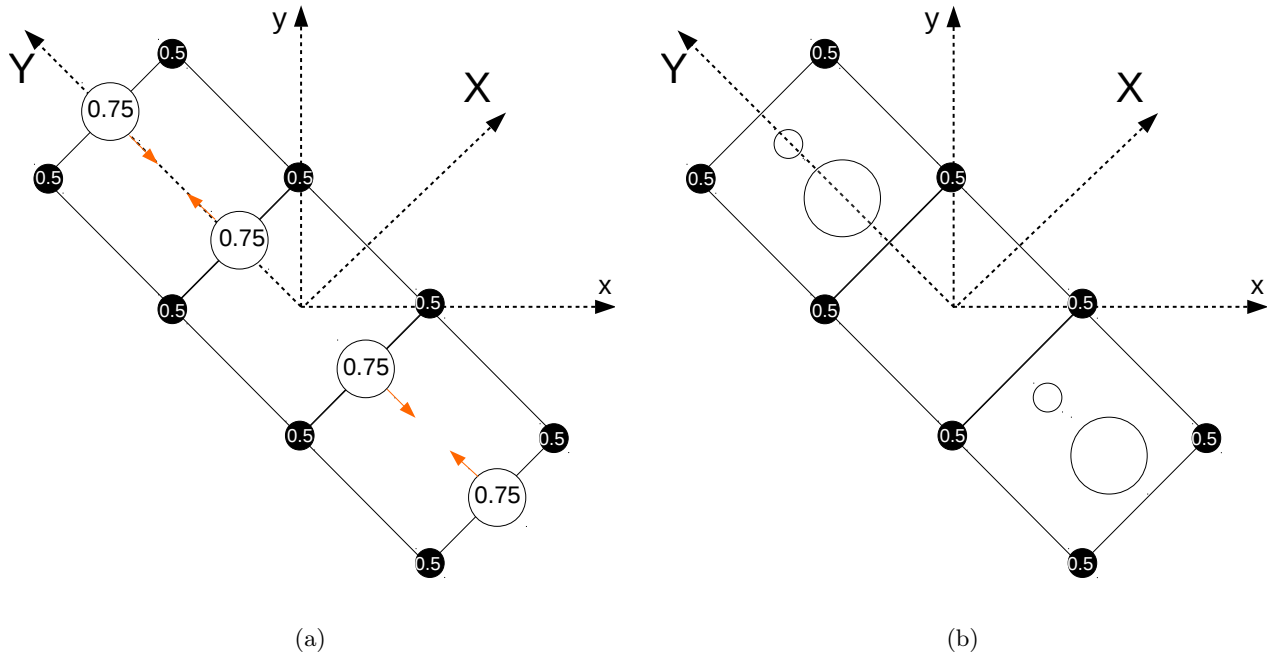


Figure 1.6: (a) before and (b) after process for the dimerization of the top Ge atoms (top-view). In each circle the number indicates the z coordinate of the atom in the surface cell, in unit of a . The large white circle represents the Ge "up" atom whereas the small white circle represents the Ge "down" atom.

The sideview of the dimer in the asymmetric configuration is shown in Figure 1.7.

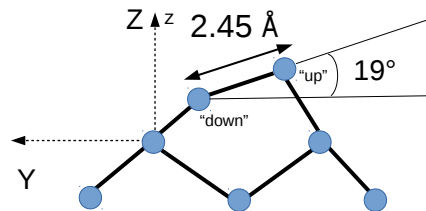


Figure 1.7: Side view of the asymmetric dimer arrangement. Experimental values of the dimer bond length and dimer tilt angle are displayed [2].

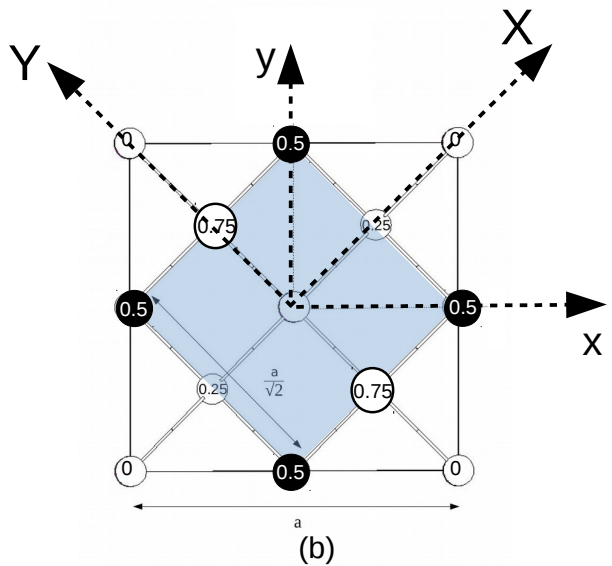
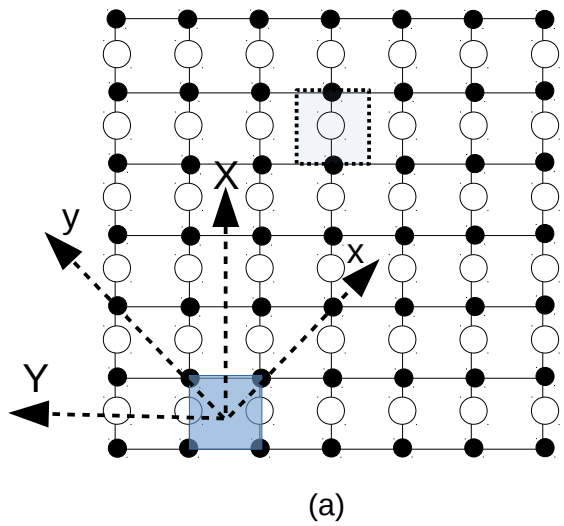
The Ge (001) surface asymmetric dimerization is of central importance not only for the description of the surface geometrical reconstruction, i.e. the rearrangements of surface atoms into patterns breaking the ideal Ge (001) surface symmetry, but also for its electronic properties. In fact, the presence of a

single unbound electron in the symmetric dimer situation, would lead to a metallic surface, whereas it is experimentally found that Ge (001) surface has a semiconductive behaviour. As we shall demonstrate in the next chapter, the buckling of the dimer with respect to the Ge (001) surface plane permits a net charge transfer from the "down" Ge dimer atom to the "up" Ge dimer atom, leading to a semiconductive behaviour of the surface, in agreement with the experimental evidence [2].

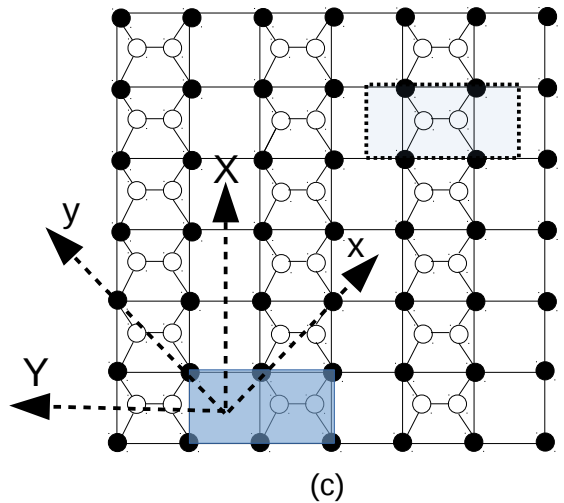
(001)-Ge surface reconstructions

As noted in the previous section, the reduction of surface dangling bonds is responsible of surface relaxation and reconstruction. Relaxation of the Ge surface atoms from the ideal-cut configuration leads to no change in the periodicity of the surface. Conversely, reconstruction of the surface is a much more readily observable effect, involving larger displacements of the surface atoms. Unlike relaxation, the phenomenon of reconstruction involves a change in the periodicity of the surface structure. The ordering of the Ge(001) surface at low temperatures has been investigated with a number of experimental techniques, showing that the Ge (001) surface may reconstruct into different patterns [2]. It is usually found that for a given sample there is experimental evidence of different reconstruction patterns. We show some of these patterns for Ge in the panels of Figure 1.8. In this Figure, we can see different patterns of the Ge (001) surface. The p(1x1) pattern is the unreconstructed ideal semi-infinite Ge (001) surface. The connection with the (001) planes of bulk Ge is shown in panel (b). This is evident from the "zoom" in Figure 1.8. In the p(2x1) asymmetric reconstruction ("p" stands for primitive) the two germanium atoms are buckled with respect to the surface plane, creating a tilt angle of approximatively 19° [2]. As discussed in section 1.2, one atom is nearer to the surface than the other one. The dimer orientation doesn't change moving along a "row" or along a "column" of p(2x1) asymmetric model of Figure 1.8. In the present thesis we shall study the (2x1) asymmetric (001)-surface reconstruction. We show in Figure 1.9 the first Brillouin zones of the surface cell of the p(1x1) ideal and of the p(2x1) asymmetric model of Figure 1.8 (a) and (d). It is evident the halving of the first Brillouin zone of the p(2x1) surface along the K_Y direction with respect to the p(1x1) ideal one, in consequence of the

Truncated
semi-infinite
 $p(1\times 1)$ ideal



Reconstructed
 $p(2\times 1)$ symmetric



Reconstructed
 $p(2\times 1)$ asymmetric

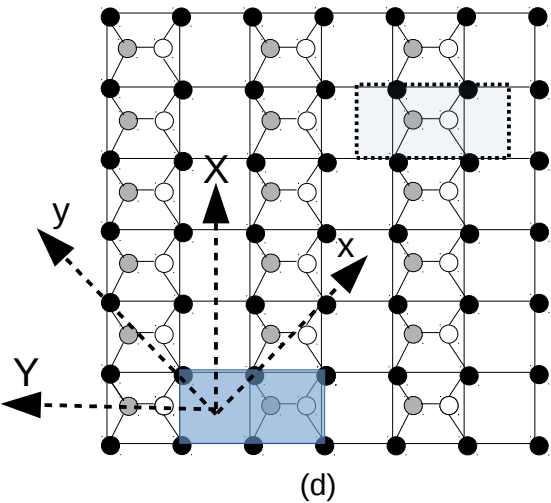


Figure 1.8: Ball and stick model of the Ge(001) surface: (a) $p(1\times 1)$ (unreconstructed) surface with (b) "zoom" to compare with Figure 1.4; (c) $p(2\times 1)$ symmetric dimer reconstruction; (d) $p(2\times 1)$ asymmetric dimer reconstruction. Grey atoms have lower z coordinate than the white ones. The shadowed areas are possible choices for the surface cells.

double length of the p(2x1) conventional cell along the Y direction.

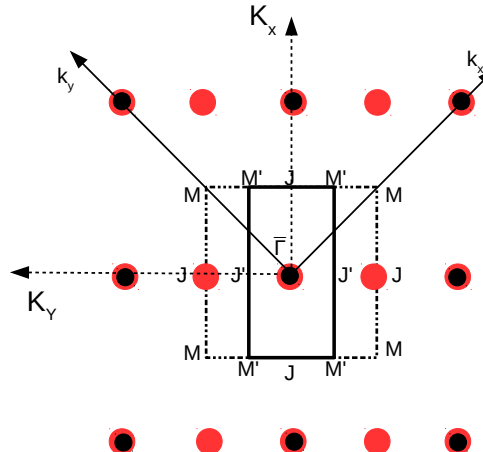


Figure 1.9: Comparison of reciprocal lattices and first Brillouin zones corresponding to p(1x1) and p(2x1) cells. The little black dots represent the reciprocal lattice points of the p(1x1) surface, the big red dots the reciprocal lattice of the p(2x1) reconstructed cell. The contour of the first Brillouin zone of p(2x1) is represented with a black continuous line, the one of the p(1x1) surface is represented with a black dotted line. Some high symmetry points are displayed.

It is worthwhile to mention other two possible reconstruction of the Ge (001) surface. We show them in Figure 1.10. The c(4x2) ("c" stands for "centred") and p(2x2) have larger surface cells than the cells of Figure 1.8. In the c(4x2) pattern the dimer orientation changes at each step if we move both along a "row" and a "column" of dimers. In the p(2x2) pattern the dimer orientation does not change along a "row" but changes at each step along a "column". Ab initio calculations [12, 42, 43] of the total energies show that the lowest energy reconstructions are the c(4x2) and the p(2x2), being nearly degenerate in energy. Anyway, all the patterns of Figures 1.8 and 1.10 are experimentally observed [44].

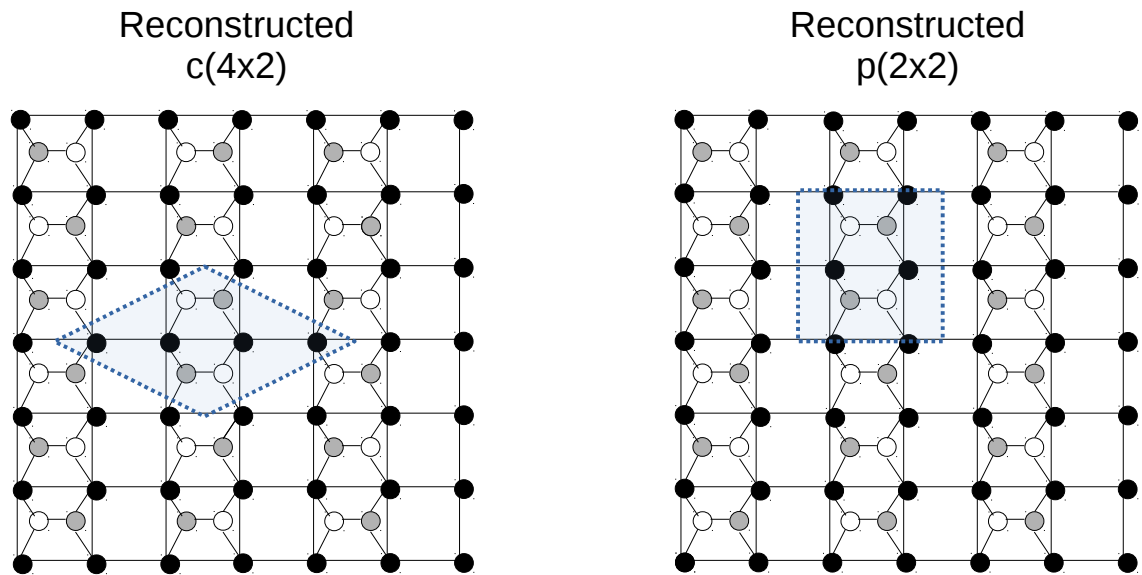


Figure 1.10: C(4x2) and p(2x2) Ge(001) surface asymmetric reconstructed surfaces. The shaded areas are the surface cells.

Chapter 2

Ab-initio evaluation of the electronic band structure

2.1 Introduction

Solids are composed by mutually interacting electrons and nuclei. The total non-relativistic Hamiltonian of a system of electrons (of coordinates \mathbf{r}_i , momenta \mathbf{p}_i , and charge $-e$) and nuclei (of coordinates \mathbf{R}_I , momenta \mathbf{P}_I , and charge $+z_I e$) in mutual interaction via Coulomb forces, can be written as:

$$H = \sum_i \frac{\mathbf{p}_i^2}{2m_e} + \sum_I \frac{\mathbf{P}_I^2}{2m_I} + \sum_i V_{nucl}(\mathbf{r}_i) + \frac{1}{2} \sum_{i \neq j} \frac{e^2}{|\mathbf{r}_i - \mathbf{r}_j|} + \frac{1}{2} \sum_{I \neq J} \frac{z_I z_J e^2}{|\mathbf{R}_I - \mathbf{R}_J|} \quad (2.1)$$

with:

$$V_{nucl}(\mathbf{r}) = - \sum_I \frac{z_I e^2}{|\mathbf{r} - \mathbf{R}_I|} \quad (2.2)$$

This Hamiltonian is impossible to be consistently resolved for the typical number of N particles in a solid, with $N \approx 10^{23}$. We present a brief summary of the most used ab-initio methods to solve the one-particle approximation to the crystal-many-body problem. The single particle Hamiltonian approximation that we will consider in this chapter is obtained by density functional theory.

2.2 Density Functional one-electron Hamiltonian

The working hypothesis on which we rely are frozen lattice and absence of relativistic effects (we will consider them separately when needed). The frozen lattice hypothesis consists in considering the nuclei fixed in the equilibrium positions \mathbf{R}_{eq} . This hypothesis is justified by the low temperature regime and with the high difference between nuclear and electronic masses. Thus the nuclear coordinates of equation (2.1) become classical parameters and we can throw away the nuclear kinetic term. Moreover, the total inter-nuclear Coulomb interaction becomes a constant and we can neglect it if we are interested in the difference of energies of the electronic states in the rigid lattice approximation. We are left with an Hamiltonian depending only on the electronic set of coordinates $\{\mathbf{r}_1, \mathbf{r}_2, \dots\}$.

In this section I shall briefly discuss how to obtain a suitable single particle Hamiltonian approximation to equation (2.1) under the previous working hypothesis by means of the *density functional theory* (DFT) scheme. Here I pick up only few points of the theory: a complete treatment can be found in the abundant literature, see e.g. [45, 46, 47, 48] and references therein.

- According to the theorems of Hohenberg-Kohn (HK) [49], for any system of interacting electrons in an external potential $V_{ext}(\mathbf{r})$, the potential $V_{ext}(\mathbf{r})$ is determined uniquely, except for an electrostatic constant, by the ground state density $n(\mathbf{r})$. Moreover, for any electronic system there exists a functional for the energy, $E[n]$, which has a global minimum for the exact ground state density $n(\mathbf{r})$. The minimization has to be performed with the constraint that $\int n(\mathbf{r})d\mathbf{r} = N$ where N is the number of particles of our system. The value $E[n(\mathbf{r})]$ is the ground state energy. Except for the part involving the external potential, the energy functional is universal. The focus of the calculation is moved from the wavefunction to the density, greatly reducing the number of degrees of freedom. If we consider a system of electron interacting via Coulomb forces and subject to an external potential, with the following Hamiltonian:

$$\hat{H}_e = T_e + V_{e-e} + V_{nucl}(\mathbf{r}) = \sum_i \frac{\mathbf{p}_i^2}{2m} + \frac{1}{2} \sum_{i \neq j} \frac{e^2}{|\mathbf{r}_i - \mathbf{r}_j|} + V_{nucl}(\mathbf{r}) \quad (2.3)$$

then the HK theory gives:

$$E^{HK}[n] = T_e[n] + V_{e-e}[n] + \int V_{nucl}(\mathbf{r})n(\mathbf{r})d\mathbf{r} = F[n] + \int V_{nucl}(\mathbf{r})n(\mathbf{r})d\mathbf{r} \quad (2.4)$$

- The practical implementation of the theory is due to Kohn-Sham [50]. The Kohn-Sham ansatz states that for each non-uniform ground-state density $n(\mathbf{r})$ of N interacting electron system there exists a non-interacting N -electron system with the same non-uniform ground-state density (this is called non-interacting v-representability). It follows that the density of the interacting system can be written as $n(\mathbf{r}) = \sum_i \phi_i^*(\mathbf{r})\phi_i(\mathbf{r})$ where $\phi_i(\mathbf{r})(i = 1, 2, \dots, N)$ are orthonormal orbitals to be determined. The Hamiltonian of the Kohn-Sham system is:

$$\hat{H}^{KS} = T_{KS} + V_{KS}(\mathbf{r}) = \sum_i \frac{\mathbf{p}_i^2}{2m} + V_{KS}(\mathbf{r}) \quad (2.5)$$

where V_{KS} is an appropriate potential to be determined (see below). Kohn-Sham ansatz is used progressing a variational procedure on the energy functional of equation (2.4). Before doing the variation, the functional of equation 2.4 is recast in the following form:

$$E[n] = T_{KS}[n] + V_H[n] + \int V_{nucl}(\mathbf{r})n(\mathbf{r})d\mathbf{r} + E_{xc}[n] \quad (2.6)$$

where $T_{KS}[n]$ is the kinetic term density functional for the non interacting system, and:

$$V_H[n] = \frac{1}{2} \int n(\mathbf{r}) \frac{e^2}{|\mathbf{r} - \mathbf{r}'|} n(\mathbf{r}') d\mathbf{r} d\mathbf{r}' \quad (2.7)$$

$$E_{xc}[n] \equiv T_e[n] - T_{KS}[n] + V_{e-e}[n] - V_H[n]$$

This procedure leads to the Kohn-Sham equations:

$$H^{KS}\phi_i(\mathbf{r}) = \left(-\frac{\nabla^2}{2m} + V^{KS}(\mathbf{r}) \right) \phi_i(\mathbf{r}) = \left(-\frac{\nabla^2}{2m} + V_{nucl}(\mathbf{r}) + V_{Coul}(\mathbf{r}) + V_{xc}(\mathbf{r}) \right) \phi_i(\mathbf{r}) = \epsilon_i \phi_i(\mathbf{r}) \quad (2.8)$$

where we have the non-interacting kinetic energy term $-\frac{\nabla^2}{2m}$, the external potential $V_{nucl}(\mathbf{r})$, the Hartree potential $V_{Coul}(\mathbf{r}) = \frac{\delta V_H[n(\mathbf{r})]}{\delta n(\mathbf{r})}$, and the exchange-correlation term $V_{xc}(\mathbf{r}) = \frac{\delta E_{xc}[n(\mathbf{r})]}{\delta n(\mathbf{r})}$ which contains statistical and dynamical correlations. Unfortunately, we don't have any explicit exact form for the $V_{xc}(\mathbf{r})$ term.

At the end of this procedure, we are finally left with equation (2.8) which is a single particle Hamiltonian approximation to equation (2.1). We are going to discuss in the following the solving procedure and the approximations to the ground-state exchange-correlation functional.

2.3 Self-consistent solution of the Kohn-Sham equations

Kohn-Sham equations (2.8) need a special solving treatment. The first problem that we encounter is that the Hamiltonian is a functional of the ground state electronic density $n(\mathbf{r})$, which in turn depends on the solutions of Kohn-Sham equations. Therefore, in order to compute the single-particle solutions $\phi_i(\mathbf{r})(i = 1\dots N)$, we should first know the one-electron density $n(\mathbf{r})$. As this is evidently impossible, one strategy is to start from a reasonable guess of to the density, say $n_0(\mathbf{r})$, to approximatively evaluate the Hamiltonian operator of equation (2.8). The single-particle solutions $\phi_i^0(\mathbf{r})(i = 1\dots N)$ corresponding to the density $n_0(\mathbf{r})$ can now be obtained solving the Kohn-Sham equations (2.8). The following step is to consistently calculate the output density $n_1(\mathbf{r})$ starting from the solutions $\phi_i^0(\mathbf{r})$ as $n_1(\mathbf{r}) = \sum_{i=1}^N \phi_i^{0,*}(\mathbf{r})\phi_i^0(\mathbf{r})$ (in general $n_1(\mathbf{r}) \neq n_0(\mathbf{r})$). Solution of equation (2.8) with the density $n_1(\mathbf{r})$ leads to the single-particle orbitals $\phi_i^1(\mathbf{r})(i = 1\dots N)$. The process is iterated until agreement between input and output densities at the (i)-th step is reached within a chosen precision. Anyway, self-consistency is hard to be achieved (if not impossible) if such simple strategies of solving algorithms are implemented. Therefore, many iteration schemes are present in the literature. One common and efficient procedure is to mix the output and the input densities of (i-1)-th step to create the input density for the (i+1)-th solving step. This mixing method can be presented in different forms, as the linear mixing [46], the Broyden method [51] and the Anderson method [52]. We can represent schematically the solving procedure with the flowchart of Figure 2.1. As we can see from the flowchart 2.1 the great power of DFT scheme is that, in principle, in the (i)-th step of the self-consistent cycle we only need the density $n_i(\mathbf{r})$ to get the solutions of equation (2.8), in contrast with other methods such as the Hartree-Fock one. Anyway, several precautions must be taken during the self-consistent cycle and we shall discuss them in the following.

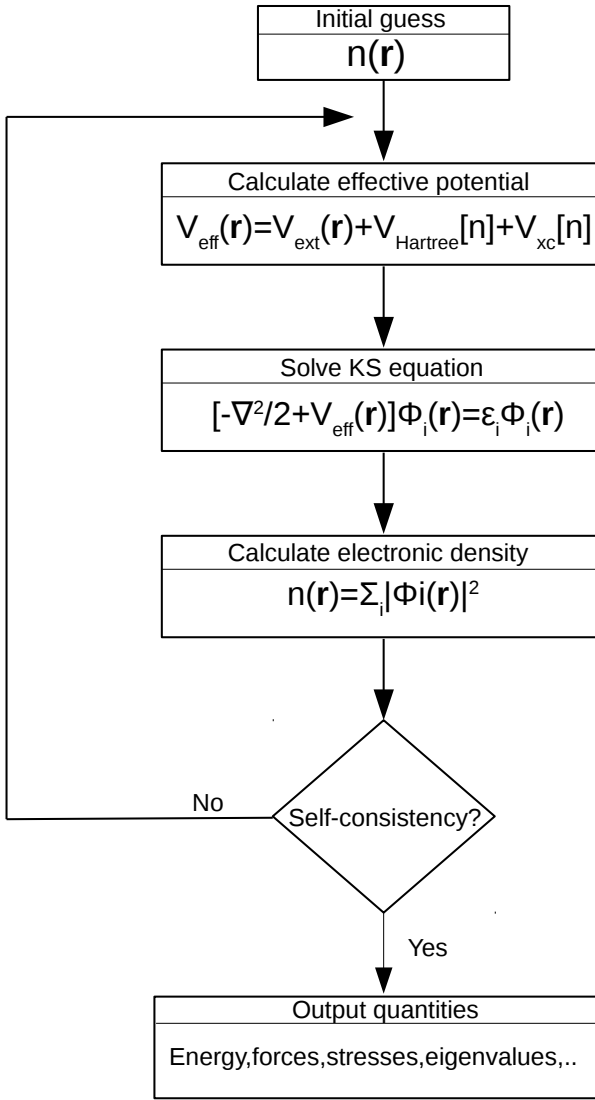


Figure 2.1: Flowchart of the self-consistent loop for the solution of Kohn-Sham equations.

2.4 Exchange-correlation functionals and pseudopotential approximations

Exchange-correlation functionals

The formal definition of the exchange-correlation functional $V_{\text{xc}}[n] = \frac{\delta E_{\text{xc}}[n]}{\delta n}$ would be of no practical use, unless workable expressions can be given for it. Therefore, many functional forms for the V_{xc} term of equation (2.8) have been presented in the literature. We find useful for the following of this work to concentrate on the LDA, the GGA and the hybrid functional expressions. In the Local Density

Approximation (LDA) the exchange-correlation functional energy is written in the form:

$$E_{xc}^{LDA}[n(\mathbf{r})] = \int \epsilon_{xc}(n(\mathbf{r})) n(\mathbf{r}) d\mathbf{r} \quad (2.9)$$

where $\epsilon_{xc}(n(\mathbf{r}))$ is the many-body exchange-correlation energy per electron of a three-dimensional uniform gas of interacting electrons of density $n(\mathbf{r})$. Among the various forms adopted for ϵ_{xc} , the parametrization given by Perdew and Zunger (PZ) [53] for the unpolarized electron gas, based on Montecarlo simulations by Ceperley and Alder, is one of the most used. It is analytically expressed as function of the dimensionless parameter r_s (local Seitz radius) defined by $(4\pi/3)(r_s a_{Bohr})^3 = 1/n$ in the form (energies expressed in Hartree):

$$\begin{aligned} \epsilon_{xc}[rs] &= \epsilon_x[rs] + \epsilon_c[rs] \\ \epsilon_x[rs] &= -\frac{0.4582}{r_s} \\ \epsilon_c[rs] &= \begin{cases} -0.1423/(1 + 1.0529\sqrt{r_s} + 0.3334r_s) & r_s \geq 1 \\ -0.0480 + 0.03111 \ln r_s - 0.0116r_s + 0.0020r_s \ln r_s & r_s \leq 1. \end{cases} \end{aligned} \quad (2.10)$$

An extension of the LDA scheme is represented by the Generalized Gradients Approximation (GGA). As in the LDA case, this is a class of exchange-correlation functionals which can be expressed as function of the density $n(\mathbf{r})$ in the following form:

$$E_{xc}^{GGA} = \int \epsilon_{xc}(n(\mathbf{r}), \nabla n(\mathbf{r})) n(\mathbf{r}) d\mathbf{r}. \quad (2.11)$$

One of the most used GGA formulations is the PBE exchange-correlation functional by Perdew, Burke and Ernzerhof [54], expressed as :

$$E_{xc}^{GGA-PBE} = \int n(\mathbf{r}) \epsilon_x^{unif}[r_s] F_{xc}(r_s, \zeta, S) \quad (2.12)$$

where ζ is the relative spin polarization $\zeta = \frac{n_{up} - n_{down}}{n}$, S is the adimensional fraction of the density gradient over the density, $S \propto \frac{\nabla n}{n}$, $\epsilon_x^{unif}[r_s]$ is the LDA expression of the exchange functional term and F_{xc} is the function reported in Figure 2.2 deduced from general considerations on the properties of the exact $E_{xc}[n]$. Indeed, there is a certain freedom in the formulation of the GGA-PBE functional, both

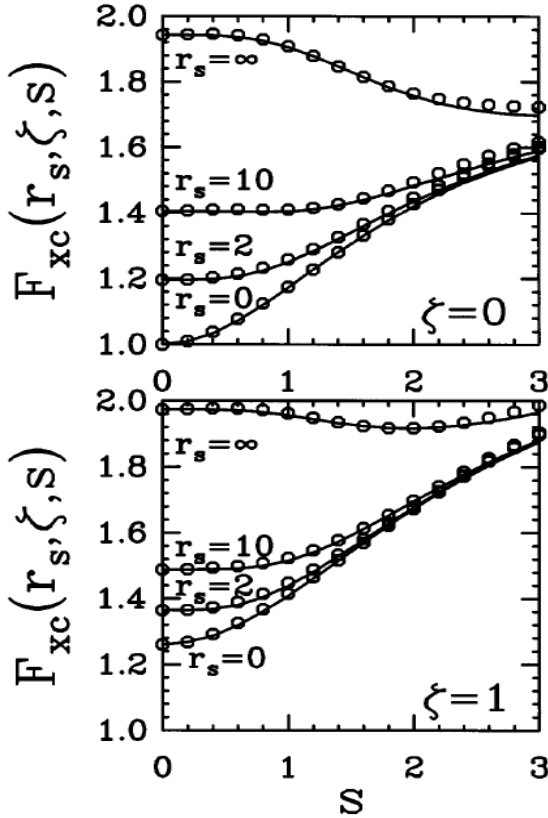


Figure 2.2: F_{xc} function of equation (2.12) as deduced in the work by Perdew, Burke and Ernzerhof [54]

in the choice of the LDA exchange functional and in some technicalities regarding the F_{xc} function. The freedom on the F_{xc} function can be exploited in order to slightly modify the behaviour of Figure 2.2 and therefore generate slightly different exchange-correlation potentials at will (for instance, the PBEsol functional is a slight modification of the PBE that better reproduces structural and electronic properties of solid state crystals).

The last class of approximations that we are going to discuss concerns hybrid functionals. They are a combination of the orbital-dependent Hartree-Fock exchange term and the explicit LDA or GGA density functionals. As they will be of central importance in our work, we give more details on their nature. Hybrid functionals originate from the following considerations:

- Consider the following Hamiltonian:

$$\hat{H}(\lambda) = \hat{T} + \lambda \hat{V}_{e-e} + \int V(\mathbf{r}, \lambda) \hat{n}(\mathbf{r}) d\mathbf{r} \quad (2.13)$$

where V_{e-e} is the Coulomb interaction between electrons, $V(\mathbf{r}, \lambda)$ is a generic external potential and λ is a tuning parameter such that $\lambda \in [0, 1]$. We assume that V is such that the eigenfunctions $\psi(\mathbf{r}, \lambda)$ of the Hamiltonian (2.13) are continuous and differentiable in λ . We will call $\psi_0(\mathbf{r}, \lambda)$ the ground state wavefunction, for given λ . We introduce the constraint that the ground-state wavefunction $\psi_0(\mathbf{r}, \lambda)$ gives the same one-electron density $n(\mathbf{r})$ for any λ , i.e. the ground-state density does not change under variation of λ . The presence of the parameter λ in (2.13) explicitly takes care of the strength of the interaction. Now we consider a potential $V(\mathbf{r}, \lambda)$ such that $V(\mathbf{r}, \lambda = 0)$ is the potential of the Kohn-Sham non-interacting electronic system of equation (2.5), while $V(\mathbf{r}, \lambda = 1)$ is the potential of the real system governed by equation (2.8), i.e. $V(\mathbf{r}, \lambda = 1) = V_{nucl}(\mathbf{r})$. For intermediate values of λ , $\hat{H}(\lambda)$ provides a smooth interpolation (called adiabatic connection) between Kohn-Sham and real system Hamiltonians.

- It can be shown [47] that applying the HK theorems to $\hat{H}(\lambda = 0), \hat{H}(\lambda = 1)$ and using the Helmann-Feynman theorem on the Hamiltonian (2.13) the following relations hold:

$$E_{xc}[n] = \frac{1}{2} \iiint_0^1 n(\mathbf{r})n(\mathbf{r}') \frac{e^2}{|\mathbf{r} - \mathbf{r}'|} [g_\lambda(\mathbf{r}, \mathbf{r}') - 1] d\mathbf{r} d\mathbf{r}' d\lambda \quad (2.14)$$

$$g_\lambda(\mathbf{r}, \mathbf{r}') = \frac{\langle \psi_0(\mathbf{r}, \lambda) | \sum_{i \neq j} \delta(\mathbf{r} - \mathbf{r}_i) \delta(\mathbf{r}' - \mathbf{r}_j) | \psi_0(\mathbf{r}, \lambda) \rangle}{n(\mathbf{r})n(\mathbf{r}')}$$

- The goal is now to approximate the exchange-correlation potential of equation (2.14) in the most realistic way, providing a workable expression of the integral in (2.14). When $\lambda = 0$ the exchange-correlation potential of equation 2.14 is simply the exchange term of HF equation (E_x^{HF}).

As argued by Becke [55], LDA or GGA functionals are the appropriate representation of the integrand for $\lambda = 1$. Following this arguments, the best approximation for $E_{xc}[n]$ should be a linear combination of LDA or GGA (or similar) and E_x^{HF} , with appropriate coefficients. Hybrid functionals are indeed formed by the implementation of these linear combinations.

There is plenty of examples of hybrid functional formulations. We cite here the Heyd-Scuseria-Ernzerhof HSE06 functional [34, 35, 36] as one of the most successful exchange-correlation potentials suitable for

solid state calculations. We report in Figure 2.3 the performance comparison between hybrid functionals and PBE exchange-correlation functional forms done by Clark and Robertson [56]; this comparison shows that hybrid functionals reproduce the fundamental electronic band-gap energies better than the ordinary PBE DFT exchange-correlation functionals.

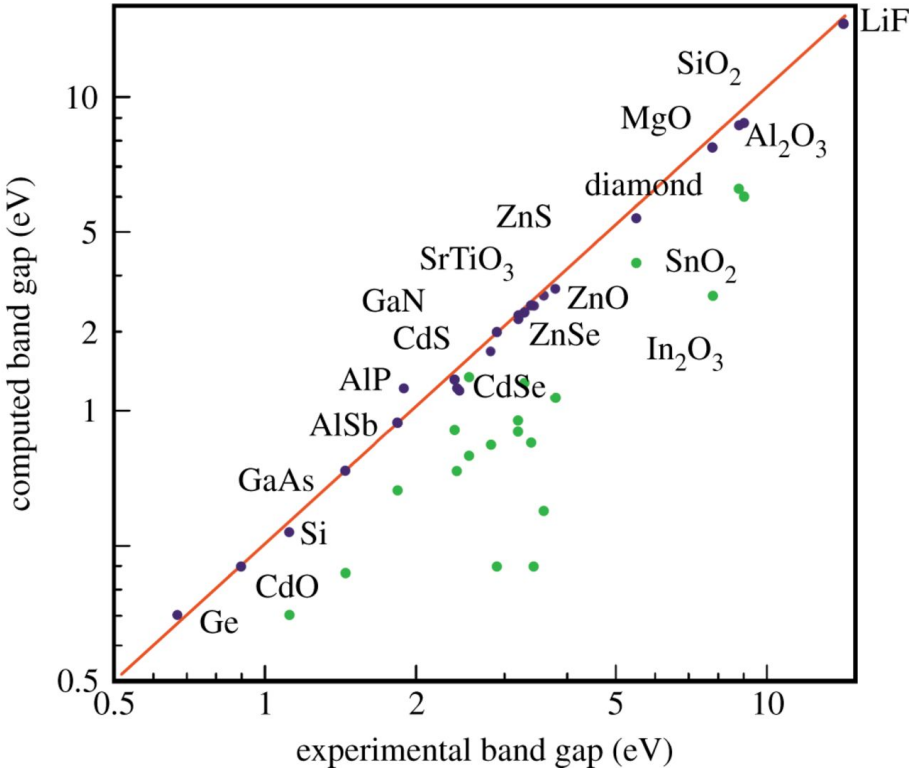


Figure 2.3: A comparison of experimental band gaps of different chemical elements with two different generations of DFT as presented in the work by Clark and Robertson [56]: computed fundamental band-gap energies from hybrid DFT calculations are dotted in blue, from PBE DFT ordinary calculations in green.

Pseudopotentials

The original application of the theory of the pseudopotentials in electronic structure calculations aims to replace the strong Coulomb potential of the nucleus and of the tightly bound core electrons by an effective ionic potential acting on the valence electrons of the atom. A pseudopotential is generally generated starting from an atomic calculation and then it is used to compute the electronic properties of

solids, since the core states remain almost unchanged from the isolated atom to the solid. Furthermore, the fact that pseudopotentials are not unique allows the freedom to choose forms that simplify the calculations and the interpretation of the resulting electronic structure. Different schemes for the generation of pseudo-potentials exist [48], such as norm-conserving pseudopotential method (NCP, scheme which will be exploited several times in this work) or ultrasoft pseudopotentials.

The first step to generate a pseudopotential is an all-electron self-consistent atomic calculation, i.e. the solution of the radial Schrödinger equation:

$$\left(-\frac{d^2}{dr^2} + \frac{l(l+1)}{r^2} + V_{all}(r) \right) r R_{nl}(r) = E_{nl} r R_{nl}(r) \quad (2.15)$$

where $V_{all}(r)$ is the atomic potential. Once the eigenvalues and eigenfunctions of equation (2.15) are known, one proceeds toward the determination of a pseudopotential $V_{pseudo}(r)$ for the pseudoatom free from the core states, and yet capable to describe the physics and chemistry of the external valence electron. One general feature of the pseudopotential $V_{pseudo}(r)$ is that outside the core region ($r > r_c$ where r_c is a suitable chosen core radius) it coincides with $V_{all}(r)$; then, in dependence on the number and on the types of electronic properties that one is willing to preserve, different generation schemes may be adopted. The concept of norm-conserving pseudopotentials starts from the technical constraint that in the region outside the core, where the true potential and the pseudopotential coincide, the atomic radial wavefunction $R_{all}(r)$ and the corresponding atomic pseudowavefunction $R_{pseudo}(r)$ are proportional to each other, but in general are not rigorously equal (as they should be). The basic principle of the norm-conserving pseudopotential is just to enforce the condition $R_{pseudo}(r) = R_{all}(r)$ for $r > r_c$; this assures that pseudo-charge density and true charge density outside the core region are perfectly equal, and, as shown by Chiang et al. [57], a strong reliability of this generating method. From equation (2.15) it is evident that the construction of pseudopotentials is to be done for each angular momentum. Under this perspective, NCPP method generates psudopotentials of simple representation: it can be shown that from KS equation it is easy to obtain semi-local atomic pseudo-potentials which act differently on states with different angular momentum, i.e in the form $V(\mathbf{r}) = \sum_l |l\rangle V_l(r) \langle l|$ [46].

2.5 Solution of Kohn-Sham equations with localized basis functions

Since in the following we will use the localized-Gaussian-orbitals code CRYSTAL14 [31] to calculate one-electron properties of our working systems, and since CRYSTAL14 adopts Linear Combination of Atomic Orbitals (LCAO) as basis functions for the solution of equation (2.8), I briefly discuss here this method.

LCAO is one of the most used methods to solve the one-electron Hamiltonian equation (2.8) when physical insight on the nature of the states suggests the use of atomic-like basis set. We can exemplify the method in the case of a crystal with one atom per primitive cell. We look for solutions $\Psi(\mathbf{k}, \mathbf{r})$ of equation (2.8) in terms of linear combinations of Bloch functions $\Phi_i(\mathbf{k}, \mathbf{r})$ built from atomic-like orbitals $\phi_i(\mathbf{r} - \mathbf{t}_n)$, corresponding to the wave-vector \mathbf{k} :

$$\begin{aligned}\Psi(\mathbf{k}, \mathbf{r}) &= \sum_{i=1}^{\lambda} c_i(\mathbf{k}) \Phi_i(\mathbf{k}, \mathbf{r}) \\ \Phi_i(\mathbf{k}, \mathbf{r}) &= \frac{1}{\sqrt{N}} \sum_{\mathbf{t}_n} e^{i\mathbf{k} \cdot \mathbf{t}_n} \phi_i(\mathbf{r} - \mathbf{t}_n)\end{aligned}\tag{2.16}$$

where λ is a reasonable cutoff, \mathbf{t}_n are the direct lattice vectors and $\phi_i(\mathbf{r} - \mathbf{t}_n)$ are the atomic orbitals of the element under study centred in the positions \mathbf{t}_n (in the case of many atoms of different species we just have to add another index); if we insert the trial form (2.16) of $\Psi(\mathbf{k}, \mathbf{r})$ in equation (2.8) and project on $\Phi_i(\mathbf{k}, \mathbf{r})$, we obtain an equation of the form:

$$\mathbf{F}^{KS}(\mathbf{k}) \mathbf{c}(\mathbf{k}) = \mathbf{S}(\mathbf{k}) \mathbf{c}(\mathbf{k}) E(k) \tag{2.17}$$

where $\mathbf{F}^{KS}(\mathbf{k})$ is the set of matrix elements of the Kohn-Sham Hamiltonian $\langle \Phi_i(\mathbf{k}, \mathbf{r}) | H^{KS} | \Phi_j(\mathbf{k}, \mathbf{r}) \rangle$ and $\mathbf{S}_{ij}(\mathbf{k}) = \langle \Phi_i(\mathbf{k}, \mathbf{r}) | \Phi_j(\mathbf{k}, \mathbf{r}) \rangle$ are the overlap matrix elements between Bloch functions. It is worthwhile to stress that the matrix equation (2.17) should be, in principle, solved at each step of the self-consisting procedure *for all the k-points of the first Brillouin zone*. In practice it is resolved on a finite set of \mathbf{k} points (suitably chosen as shown below) belonging to the first Brillouin zone. Many problems raise from the calculation of matrix elements of equation 2.17, and here we summarize the main ones and their solution as done by Saunders [58]:

- Problem: In principle, in equation (2.17) we have to deal with an infinite number of matrix elements of the type $\langle e^{i\mathbf{k}\cdot\mathbf{r}}\phi_i(\mathbf{r} - \mathbf{t}_n)|\hat{O}|e^{i\mathbf{k}\cdot\mathbf{r}}\phi_j(\mathbf{r} - \mathbf{t}_m)\rangle$, because we have such type of matrix element for each \mathbf{t}_n and \mathbf{t}_m .
 - ◊ Solution: The smallest matrix elements (smaller than a pre-set tolerance) are set to zero. If we fix one between \mathbf{t}_n and \mathbf{t}_m , say \mathbf{t}_n , we calculate the matrix elements between $e^{i\mathbf{k}\cdot\mathbf{r}}\phi_i(\mathbf{r} - \mathbf{t}_n)$ and $e^{i\mathbf{k}\cdot\mathbf{r}}\phi_i(\mathbf{r} - \mathbf{t}_m)$ only if \mathbf{t}_m belongs to a region (suitably chosen) *near* \mathbf{t}_n . Moreover, it is sufficient to calculate the matrix elements for only one reference fixed \mathbf{t}_n lattice vector because the translational invariance of operator \hat{O} ensure the matrix elements value does not change under the variation of \mathbf{t}_n .
- Problem: Even if we reduced the infinite matrix elements of the form $\langle\phi_i(\mathbf{r} - \mathbf{t}_n)|\hat{O}|\phi_j(\mathbf{r} - \mathbf{t}_m)\rangle$ to a finite number of matrix elements, the operator \hat{O} usually contains a sum on all lattice positions (for instance $\hat{O} = \sum_{\mathbf{t}_n} \hat{O}_{\mathbf{t}_n}$ when \hat{O} represent the crystal potential which is sum of the potentials from all the atoms).
 - ◊ Solution: Truncation criteria are used. For exchange operator this is simple because far away elements do not affect the value of the sum. For the Coulomb operator the convergence is really slow because of its long-range nature, so the series needs first to be rearranged by grouping together subsets of the total charge distribution, then a cutoff is applied.
- Problem: In principle, evaluations of many quantities through integrals need the solving equation (2.17) for each \mathbf{k} point of the First Brillouin Zone. We may wonder if it is possible to reasonably reduce the number of points where to solve equation (2.17) having control of the error due to the simplification.
 - ◊ Solution: Special \mathbf{k} -points (see next section).

Going deeper in the details of the nature of the atomic orbitals $\phi_i(\mathbf{r})$ entering in equation (2.16) as used in CRYSTAL14 code, we are going to discuss the localized-Gaussian-orbitals representation of atomic orbitals.

Two kinds of basis functions are generally used to expand the Atomic Orbitals (AOs) of equation (2.16) : Slater-type orbitals (STOs) and Gaussian-type orbitals (GTOs). CRYSTAL14 code makes use of the Gaussian functions. The basic form of a Gaussian function, for each angular momentum, is:

$$g(\mathbf{r}, \alpha, l) = r^l e^{-\alpha r^2} Y_{lm}(\theta, \phi) \quad (2.18)$$

where l is the value of the angular momentum, $Y_{lm}(\theta, \phi)$ are the spherical harmonics, and α a given coefficient. Even if STOs better reproduce the atomic wavefunction near the nucleus, GTOs are of practical use because numerical evaluation of integrals becomes really easy. In CRYSTAL14 the Atomic Orbitals $\phi_i(\mathbf{r})$ of equation (2.16) are expanded in terms of GTO as shown in equation (2.19).

$$\phi_i(\mathbf{r}) = \sum_{j=1}^{p_i} d_j g(\mathbf{r}, \alpha_j, l) \quad (2.19)$$

where $d_j, j(= 1...p_i)$ are often called contraction coefficients to be tuned for each type of atomic orbital, $\alpha_j, (j = 1...p_i)$ are appropriate choices for the α exponential factor of equation (2.18) and $p_i, (i = 1...\lambda)$ is a cutoff on the number of Gaussians used in the representation of one single orbital. It is worthwhile to stress that GTOs really simplify the calculation of integrals, especially the two-electron four-centre integrals of the coulomb/exchange term. Different choices of the d_j, α_j, p_i parameters determines different *localized basis set* to be used in the expansions of equation (2.16).

2.6 Solution of Kohn-Sham equations with plane waves basis functions

Since in the following of this thesis we will also use the plane-waves code QUANTUM ESPRESSO [30] to calculate one-electron properties of our working systems, and since that QUANTUM ESPRESSO exploits plane waves (PW) for the solution of equation (2.8), I briefly discuss this method in this section.

A plane wave basis set is formed by functions of the form $W_{\mathbf{h}_i}(\mathbf{k}, r) = \frac{1}{\sqrt{V}} e^{i(\mathbf{k} + \mathbf{h}_i) \cdot \mathbf{r}}$, where \mathbf{k} is a generic point of the first Brillouin zone of the crystalline system under consideration and \mathbf{h}_i are reciprocal lattice vectors. An important parameter associated with a plane waves basis set is the *energy*

cutoff. The energy cutoff indicates the maximum value of the wave-vector moduli $|\mathbf{k} + \mathbf{h}_i|$ characterizing the basis set. Therefore, the number of elements composing the basis set is related to the energy cutoff value. It follows that in dependence of different values of the energy cutoff we can create different plane waves basis sets. This manageability of the basis set choice is one of the most valuable benefits due to the use of the plane wave method.

If we adopt a plane waves basis set for the calculation of matrix elements of equation (2.8), without any pseudopotential approximation, we encounter the so-called "variational collapse" problem. In fact, differently from LCAO method, PWs cannot well describe the core part of the wavefunction within a reasonable value of the basis cutoff, invalidating energy calculation. Thousands of plane waves or even more are typically needed to describe the sharp shape of the wave function inside the core of the nuclear potential. This problem is generally solved adopting an appropriate pseudopotential approximation to the nuclear potential.

In the plane waves basis set framework we look for solutions to equation (2.8) of the form:

$$\phi(\mathbf{k}, \mathbf{r}) = \frac{1}{\sqrt{V}} \sum_{\mathbf{h}_l}^{cutoff} c(\mathbf{k}, \mathbf{h}_l) e^{i(\mathbf{k} + \mathbf{h}_l) \cdot \mathbf{r}} \quad (2.20)$$

where the sum on the reciprocal lattice vectors \mathbf{h}_l includes all the plane waves belonging to the basis set according to the energy cutoff value. Once chosen an energy cutoff and adopted an appropriate pseudopotential for the atoms of the system under consideration, we have that the matrix elements of equation (2.8) between plane waves with different \mathbf{k} (and not related by any reciprocal lattice) vanish due to the Bloch theorem. We are finally left with the following equation:

$$\mathbf{H}^{KS}(\mathbf{k}) \mathbf{c}(\mathbf{k}) = \mathbf{c}(\mathbf{k}) E(k) \quad (2.21)$$

where $H^{KS}(\mathbf{k})$ is the set of matrix elements of the Kohn-Sham Hamiltonian $\langle e^{i(\mathbf{k}) \cdot \mathbf{r}} | H^{KS} | e^{i(\mathbf{k}') \cdot \mathbf{r}} \rangle$ such that $\mathbf{k}' = \mathbf{k} + \mathbf{h}$ for some reciprocal lattice vector h . As in LCAO method we have to solve equation (2.21) for each \mathbf{k} belonging to the first Brillouin zone.

The main problem of plane waves method is that, even with pseudopotential method, evaluation of matrix elements with plane waves can be laborious. We mention for instance the problem of the

evaluation of Hartree-Fock like exchange terms (present for examples in hybrid functionals) in equation

(2.8) [59] even after the self-consistent field determination:

$$\begin{aligned} \langle e^{i(\mathbf{k}+\mathbf{h}_i) \cdot \mathbf{r}} | V_{exch} | e^{i(\mathbf{k}+\mathbf{h}_j) \cdot \mathbf{r}} \rangle &= -e^2 \sum_{m,\mathbf{q}} \int d\mathbf{r} d\mathbf{r}' e^{-i(\mathbf{k}+\mathbf{h}_i) \cdot \mathbf{r}} \phi_m^*(\mathbf{q}, \mathbf{r}') \phi_m(\mathbf{q}, \mathbf{r}) e^{i(\mathbf{k}+\mathbf{h}_j) \cdot \mathbf{r}} \frac{1}{|\mathbf{r} - \mathbf{r}'|} \\ &= -\frac{4\pi e^2}{V} \sum_{m,\mathbf{q}} \sum_{\mathbf{h}_k} \frac{c_m^*(\mathbf{q}, \mathbf{h}_j + \mathbf{h}_k) c_m(\mathbf{q}, \mathbf{h}_i + \mathbf{h}_k)}{|\mathbf{k} - \mathbf{q} - \mathbf{h}_k|^2} \end{aligned} \quad (2.22)$$

The above expression clearly contains a divergence when $\mathbf{k} - \mathbf{q} = \mathbf{h}$ for a certain reciprocal lattice vector \mathbf{h} . This require an appropriate treatment (Gygi-Baldereschi [59]). Moreover, we have a sum over the Brillouin zone for each matrix element. This can be really time consuming.

2.7 Special k points and Monkhorst-Pach method

A number of observable quantities need calculation of integrals of periodic functions over the Brillouin zone. This task may require a very high effort if no simplification is applied. The methods developed to deal with such integrals consist in smart sampling of the Brillouin zone through some algorithms. We briefly present the general features of the special-points technique and of the so-called Monkhorst and Pack method [60].

As stated before, we often have to deal with integrals, arising from the approximation of sums over the whole set of \mathbf{k} points belonging to the first Brillouin zone, of the type:

$$\bar{f} = \frac{\Omega}{(2\pi)^3} \int_{BZ} f(\mathbf{k}) d\mathbf{k} \quad (2.23)$$

where Ω is the unit cell volume and $f(\mathbf{k})$ is a periodic function with period given by the reciprocal lattice vectors. We also assume that $f(\mathbf{k})$ is left invariant under the action of the crystal symmetry group. This means that if we have a symmetry operator \hat{R} (for instance a rotation) and two points in the reciprocal space such that $\mathbf{k}_i = \hat{R}\mathbf{k}_j$, then $f(\mathbf{k}_i) = f(\mathbf{k}_j)$. We now expand $f(\mathbf{k})$ in the direct lattice components $f(\mathbf{k}) = \sum_{\mu} f_{\mathbf{t}_{\mu}} e^{i\mathbf{k}\cdot\mathbf{t}_{\mu}}$ and we note that, if $\mathbf{t}_i = \hat{R}\mathbf{t}_j$, then $f_{\mathbf{t}_i} = f_{\mathbf{t}_j}$ because f is symmetric under symmetry operations. We proof it explicitly:

$$f(\mathbf{k}) = \sum_{\mu} f_{\mathbf{t}_{\mu}} e^{i\mathbf{k}\cdot\mathbf{t}_{\mu}} = f(\hat{R}^T \mathbf{k}) = \sum_{\mu} f_{\mathbf{t}_{\mu}} e^{i(\hat{R}^T \mathbf{k}) \cdot \mathbf{t}_{\mu}} = \sum_{\mu} f_{\mathbf{t}_{\mu}} e^{i\mathbf{k} \cdot \hat{R}\mathbf{t}_{\mu}} \quad (2.24)$$

We thus obtain that:

$$\sum_{\mu} f_{\mathbf{t}_{\mu}} e^{i \mathbf{k} \cdot \mathbf{t}_{\mu}} = \sum_{\mu} f_{\mathbf{t}_{\mu}} e^{i \mathbf{k} \cdot \hat{R} \mathbf{t}_{\mu}} \quad (2.25)$$

Now, if we define $\hat{R} \mathbf{t}_{\mu} = \mathbf{t}_{\nu}$, we have:

$$\sum_{\mu} f_{\mathbf{t}_{\mu}} e^{i \mathbf{k} \cdot \mathbf{t}_{\mu}} = \sum_{\nu} f_{\hat{R} \mathbf{t}_{\nu}} e^{i \mathbf{k} \cdot \mathbf{t}_{\nu}} \quad (2.26)$$

Equating all the coefficients, we have the proof. This observation suggests to rearrange the sum into shells C_n of symmetry related vectors. This means that the vectors belonging to a shell transform amongst themselves under the operations of the symmetry group of the crystal. Moreover, we index these shells according to increasing modulus of the vectors \mathbf{t}_{ν} . Therefore we come up to the following expression:

$$\begin{aligned} f(\mathbf{k}) &= \sum_{n=0}^{\infty} f_n A_n(\mathbf{k}) \\ A_n(\mathbf{k}) &= \frac{1}{\sqrt{N_n}} \sum_{|\mathbf{t}| \in C_n} e^{i \mathbf{k} \cdot \mathbf{t}} \end{aligned} \quad (2.27)$$

where N_n is the number of vectors belonging to a single shell. If we sum both members of the first equation in (2.27) over the B.Z. and divide by N (the large number of allowed \mathbf{k} vectors in the first Brillouin zone), we obtain:

$$f_0 = \frac{1}{N} \sum_{\mathbf{k}}^{B.Z.} f(\mathbf{k}) \approx \frac{\Omega}{(2\pi)^3} \int_{BZ} f(\mathbf{k}) d\mathbf{k} \quad (2.28)$$

We finally find that $\bar{f} = f_0$. The interesting fact is that in equation (2.27) we factorized the contribution due to different Fourier components grouped in symmetry-related shells. The general idea of special-points techniques is to look for a point \mathbf{k}^* (or a set of points) that makes $A_n(\mathbf{k}^*) = 0 \quad \forall n \neq 0$, or at least for a finite number of n , so that $f(\mathbf{k}^*) \approx f_0$. The approximation of satisfying the equation for a finite number of n is justified if we know that the components $f_{\mathbf{t}_{\mu}}$ with highest $|\mathbf{t}_{\mu}|$ are negligible. Let us suppose that we can find a set of N_k points and relative weights (\mathbf{k}_i, w_i) such that:

$$\begin{aligned} \sum_{i=1}^{N_k} w_i &= 1 \\ \sum_{i=1}^{N_k} w_i A_n(\mathbf{k}_i) &= 0 \end{aligned} \quad (2.29)$$

where n goes from 1 to N_p ; N_p is the number of shells we can consistently put to zero altogether. In this case we can approximate f_0 in the following way:

$$f_0 \approx \sum_{i=1}^{N_k} w_i f(\mathbf{k}_i) \quad (2.30)$$

with an error that is under control and can be written as:

$$\epsilon = - \sum_{n=N_p+1}^{\infty} f_n \sqrt{N_n} \sum_{i=1}^{N_k} w_i A_n(\mathbf{k}_i) \quad (2.31)$$

The Monkhorst and Pack (MP) method consists in the creation of a mesh of points and appropriate weights satisfying the equations (2.29) in an efficient way. The MP method requires an integer number q as an input, to determine the size of the mesh. A grid of q^3 points $\mathbf{K}_{MP} = u_p \mathbf{g}_1 + u_r \mathbf{g}_2 + u_s \mathbf{g}_3$ is then generated, where u_p, u_r, u_s are appropriate coefficients and $\mathbf{g}_1, \mathbf{g}_2, \mathbf{g}_3$ are the reciprocal lattice basis vectors. The next step is to bring back the generated points to the Irreducible Brillouin Zone (IBZ) through symmetry operations, and if one point coincides with l other points of the mesh after this operation, it is given a weight l (default is 1). The weights must be renormalized to be consistent with the first equation in (2.29). The appropriate form of u_p, u_r, u_s permits the fulfilment of both conditions of equation (2.29). In the MP procedure the number N_p depends on the space group of the crystal. We mention that a problematic step of this procedure is the assumption of the rapid decay of the Fourier components. Indeed, this assumption usually fails in the case of metals because in the calculations of Fermi energy the presence of discontinuous functions as integrands (Fermi distribution at null temperature) imply that the even high Fourier components may be not negligible. Anyway, several methods are available even in this case. We finally can answer the question concerning the calculation of a physical observable within a certain precision, which in principle would require the solution the equation (2.17) for each \mathbf{k} point of the first Brillouin zone: it is sufficient to solve the eigenvalue problem of equation (2.17) for some special points with known weights inside the irreducible Brillouin zone.

2.8 Surface band structure calculation

The termination of an ideal crystal, due to the presence of a surface, obviously causes a reduction of periodicity of the system in the direction orthogonal to the truncation plane. In chapter 5, we will study the p(2x1) Ge (001) surface of Figure 1.8 (c); this system presents a 2-dimensional periodicity in the (X, Y) plane, the periodicity along [001] is truncated by the surface. In order to describe this 2-dimensional periodicity, we work with the simulation cell of Figure 5.1 (b), periodically repeated in the (X, Y) plane. The first Brillouin zone of the surface simulation cell is shown in Figure 1.9. We are now going to discuss how to solve the Kohn-Sham equations (2.8) in this case.

In the following of this section, we will call \mathbf{r}_{\parallel} the components of the direct space vector \mathbf{r} parallel to the Ge (001) surface (and therefore orthogonal to the [001] direction), and \mathbf{k}_{\parallel} the reciprocal space vectors belonging to the surface Brillouin zone of Figure 1.9 . In principle, for a system which presents two dimensional periodicity (in the (X, Y) plane in our case) we should apply Bloch theorem for each value of the coordinate Z along [001] direction, having that the one-particle solutions of equation (2.8) can be written as:

$$\phi(\mathbf{r}) = \phi(\mathbf{r}_{\parallel}, Z) = u_{\mathbf{k}_{\parallel}}(\mathbf{r}_{\parallel}, Z)e^{i\mathbf{k}_{\parallel}\cdot\mathbf{r}_{\parallel}} \quad (2.32)$$

In practice, as will be discussed in chapter 5, computational softwares are mostly built for 3-D calculations. This means that the system is (artificially) periodically reproduced in the direction of no periodicity, but separating the copies of the system by a sufficient amount of space in order to avoid any type of interaction between adjacent cells. The creation of a third direction of periodicity implies that the first Brillouin zone of the system becomes three-dimensional, but, if the periodically repeated copies of the system are distant enough in the reciprocal space, it can be nevertheless approximated as two-dimensional system (along the \mathbf{K}_X and \mathbf{K}_Y directions). It will be useful in our work to compare eigenvalues of equation (2.8) obtained for the Ge ideal bulk crystal, i.e. with perfect 3 dimensional periodicity, with the eigenvalues of the p(2x1) Ge (001) surface, which has two-dimensional periodicity. The importance of this comparison is highlighted: if, solving Kohn-Sham equations (2.8) for the p(2x1)

Ge (001) surface system, we find new eigenvalues which correspond to forbidden energies for the Ge bulk crystal or eigenvalues which are resonant with allowed energies of the bulk Ge crystal, then the corresponding states, which are often spatially localized, are called "surface states". The spatial and orbital classification of the eigenvalues and eigenfunctions of equations (2.8) is important if we want to individuate electronic states which are mainly localized on the crystal surface.

We now present the procedure adopted to compare the unstrained p(2x1) Ge (001) surface and unstrained Ge bulk crystal single-particle energies :

- We choose a reference system in which the Ge ideal bulk structure and the p(2x1) Ge (001) surface are coherently oriented. Consequently, the first Brillouin zones of the two systems can be coherently represented in the same momentum space (see Figure 2.4).
- We solve equation (2.8) for the Ge ideal bulk and we obtain the set of eigenvalues $\{\epsilon_{\mathbf{k}}\}_{k \in B.Z.}$, with \mathbf{k} belonging to Ge the crystal first Brillouin zone of Figure 2.4.
- We solve equation (2.8) for the surface system and we obtain the set of eigenvalues $\{\epsilon_{\mathbf{k}_{||}}\}_{k_{||} \in B.Z.}$, with $\mathbf{k}_{||}$ inside the p(2x1) Ge (001) surface first Brillouin zone of Figure 2.4.
- For each $\mathbf{k} = k_X \hat{K}_X + k_Y \hat{K}_Y + k_Z \hat{K}_Z$ belonging to the Ge bulk 3-D Brillouin zone, we define the two dimensional vector $\mathbf{k}' = k_X \hat{K}_X + k_Y \hat{K}_Y$. Clearly, all the first Brillouin zone vectors which differ only for the coordinate along \hat{K}_Z "correspond" to the same \mathbf{k}' .
- We define the set of energies formed by all the Ge bulk crystal eigenvalues $\epsilon_{\mathbf{k}}$ corresponding to the same \mathbf{k}' . We call this set $\{E(\mathbf{k}')\}$.
- We consider the points belonging to the surface first Brillouin zone such that $\mathbf{k}_{||} = \mathbf{k}'$ (a folding procedure may be necessary) and make the following association: $\mathbf{k}_{||} \rightarrow (\epsilon_{\mathbf{k}_{||}}, \{E(\mathbf{k}')\})$. We can now draw energy bands starting from the surface first Brillouin zone using the previous association. This operation will be called in the following as the *projection of the Ge bulk energy bands onto the p(2x1) Ge (001) surface Brillouin zone*.

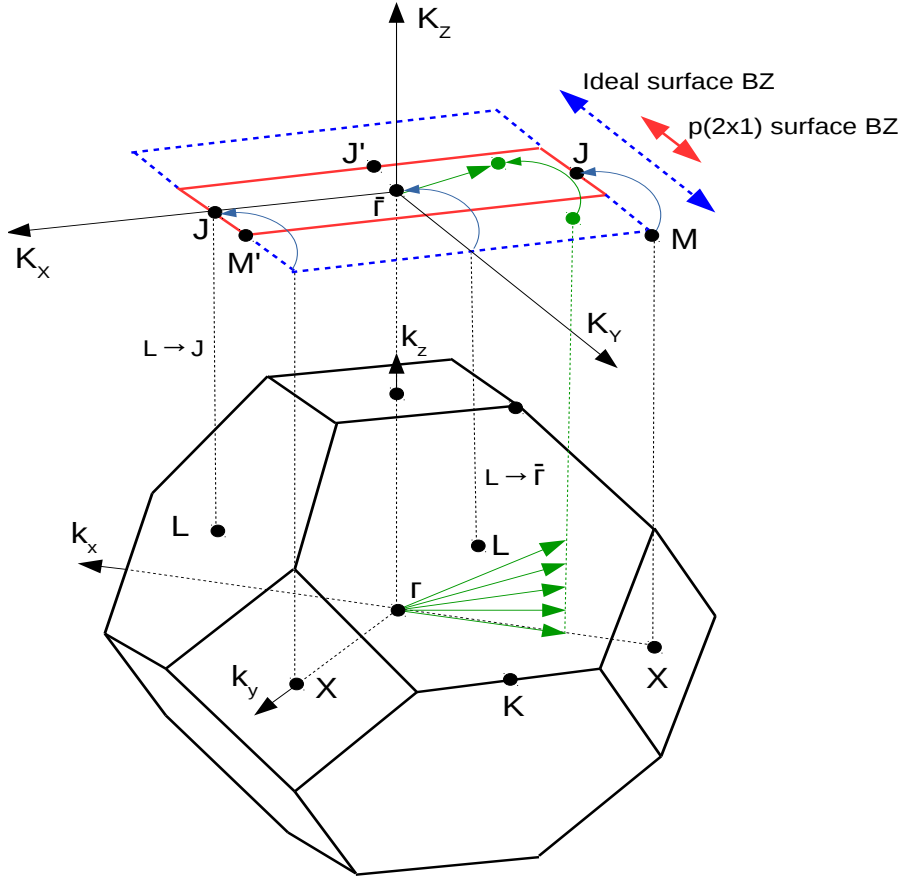


Figure 2.4: In the upper panel it is shown the folding of the ideal (001) surface Brillouin zone (contoured by dashed blue line) into the p(2x1) Ge (001) one (contoured by red line). We also report the projection of the Ge bulk Brillouin zone vectors (lower panel) onto the p(2x1) Ge (001) surface. The Ge bulk vectors (in green), having the same coordinates along the K_X and K_Y directions, are projected into the same point (in green) of the surface.

When we will deal with non-hydrostatic strains (in chapters 7 and 8), we have to consider that the Ge bulk crystal conventional cell and first Brillouin zone become tetragonal because of the reduction of the Hamiltonian symmetry group. Anyway, it is useful to double the conventional cell of the strained Ge bulk along the Y direction (see Figure 7.4), therefore halving the first Brillouin zone along the K_Y direction (as presented in the top panel in Figure 2.4 and in Figure 2.5). We will perform the comparison between the Ge bulk energies (calculated with a convenient conventional cell) and the

$p(2\times 1)$ Ge (001) surface energies when the two systems are *equally strained*. The procedure is equal to the one for the unstrained case and it is shown in Figure 2.5.

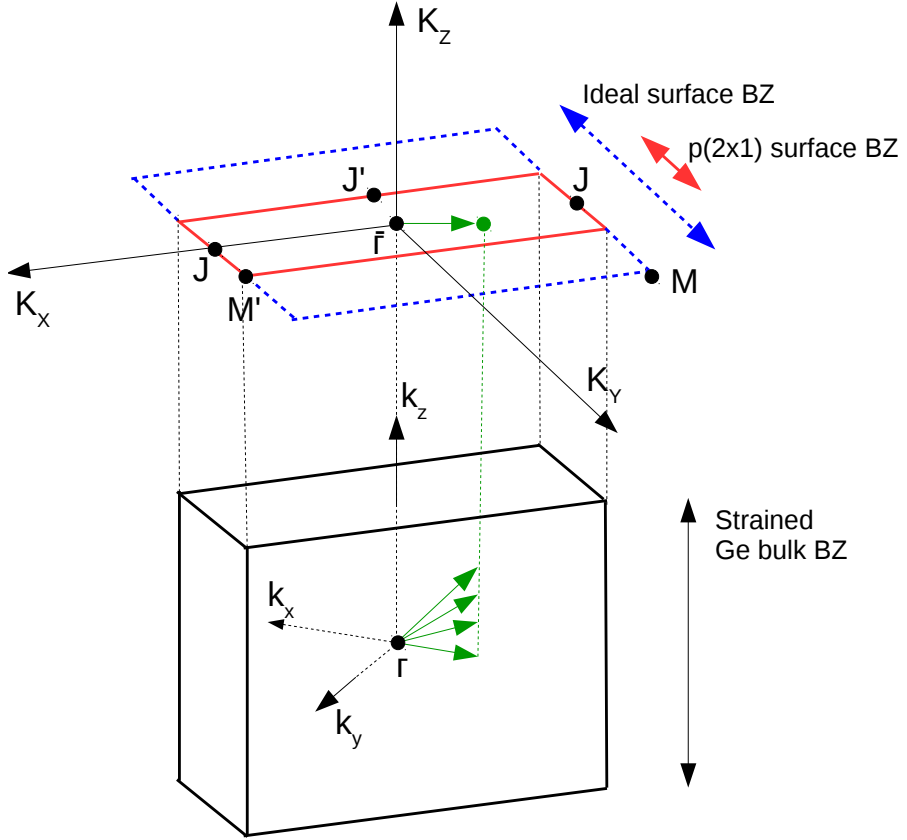


Figure 2.5: Schematic of the projection of the strained Ge bulk first Brillouin zone vectors onto the equally strained $p(2\times 1)$ Ge (001) surface first Brillouin zone. The Ge bulk vectors (in green), having the same coordinates along the K_X and K_Y directions, are projected into the same point (in green) of the surface.

Chapter 3

Ab-initio methods for geometric structure optimization

One of the major benefits of the use of the DFT scheme for the calculation of crystal electronic properties is the possibility to evaluate exactly (in principle) the value of the ground state energy of the electronic interacting system of the crystal under external potential. This fact, in conjunction with the adiabatic approximation (as we will see in the following), permits to determine the minimum energy spatial configuration of the atoms in the crystal. This task is exceptionally important when dealing with structures which detach from ideal configuration (as the case of the p(2x1) Ge (001) surface) or which are not accesible experimentally. Therefore, in this chapter we briefly present the main features of the procedure used to find the geometric minimum energy configuration. We will refer to this process in the following as *geometric optimization*.

3.1 Internal coordinates

The fist important remark is that, when dealing with a given spatial distribution of atoms, it is often useful to switch from cartesian coordinates to internal coordinates. Orthogonal Cartesian coordinates (x, y, z) are a set of $3N$ x-y-z numbers, where N is the number of atoms belonging to the material;

internal coordinates instead is a set of $3N - 6$ numbers, explicitly formed by bond lengths, bond angles and dihedral angles (the difference of 6 degrees of freedom with the cartesian coordinates is due to the disregard of position and orientation of the whole crystal in space). Bond angles are defined as the angles between two adjacent bonds. To define dihedral angles, we consider 4 consecutive atoms of our system, say A_1, A_2, A_3, A_4 and the planes passing through A_1, A_2, A_3 and A_2, A_3, A_4 . The dihedral angle is defined as the angle between these two (intersecting) planes.

We now link cartesian coordinates (which we will indicate with a generic vector \mathbf{x} of dimension $3N$) and internal coordinates (which we will indicate with a generic vector ζ) and see how gradients and Hessians are expressed in the two coordinate systems. We add 6 external coordinates to the internal ones in order to handle with square matrices, in fact we define the matrix B as the matrix that transforms Cartesian coordinates into internal coordinates :

$$\xi = B\mathbf{x} \quad (3.1)$$

3.2 Adiabatic approximation

When solving for the energy of a system made of nuclei and electrons, described by the Hamiltonian $H(\{\mathbf{r}\}, \{\mathbf{R}\})$ of equation (2.1), we can exploit the difference of the nuclear and electronic masses and treat perturbatively the kinetic energy operator of the nuclei, supposing as first step the nuclei fixed in a given spatial configuration (adiabatic approximation, [48]). In the search of the minimum energy (equilibrium) configuration of the system, we start considering a set of atomic position $\{R\}$ which are suitably guessed to be near the equilibrium ones and calculate the forces acting on nuclei; the set of equilibrium coordinates is then determined finding the atomic positions where the forces on the atoms are zero. Consider the Hamiltonian of equation (2.1). The eigenvalue equation is:

$$H(\{\mathbf{r}\}, \{\mathbf{R}\})\Psi_{mb}(\{\mathbf{r}\}, \{\mathbf{R}\}) = W\Psi_{mb}(\{\mathbf{r}\}, \{\mathbf{R}\}) \quad (3.2)$$

where W are the many-body eigenvalues and the subscript mb stands for "many-body". We now use the Born-Oppenheimer approximation for the ground-state configuration, which consists in approximating

the manybody wavefunction in the following way:

$$\Psi_{mb}(\{\mathbf{r}\}, \{\mathbf{R}\}) \approx \chi(\{\mathbf{R}\}) \Psi_0(\{\mathbf{r}\}, \{\mathbf{R}\}) \quad (3.3)$$

where $\chi(\{\mathbf{R}\})$ depends only on the nuclear coordinates and $\Psi_0(\mathbf{r})$ is the ground-state solution for the electronic problem for fixed $\{\mathbf{R}\}$. If we indicate with $E_0(\{\mathbf{R}\})$ the electronic ground state energy as function of the set of atomic coordinates, then inserting equation (3.3) into equation (3.2) we obtain the following equation for the nuclear dynamics:

$$\left[\sum_I \frac{\mathbf{P}_I^2}{2M_I} + E_0(\{\mathbf{R}\}) + \sum_{I \neq J} \frac{z_I z_J e^2}{|\mathbf{R}_I - \mathbf{R}_J|} \right] \chi(\{\mathbf{R}\}) = W \chi(\{\mathbf{R}\}) \quad (3.4)$$

where we have disregarded non-adiabatic terms [48]. $E_0(\{\mathbf{R}\})$ determines an energy surface which is called Potential Energy Surface (PES) and $V_{NN} = \sum_{I \neq J} \frac{z_I z_J e^2}{|\mathbf{R}_I - \mathbf{R}_J|}$ is the classic nuclear-nuclear interaction. The term $E_0(\{\mathbf{R}\}) + V_{NN}$ represents the potential energy acting on the nuclei. The real computational problem is to find a procedure which can, in the smallest amount of steps, give the right lowest minimum (and not, for example, a local minimum) within the needed precision. We will show an efficient procedure in the next section.

3.3 Optimization Method

One of the most efficient methods to derive the set of nuclear equilibrium coordinates $\{\mathbf{R}_{\text{eq}}\}$ is the so called Quasi-Newton approach. Quasi-Newton approach is a procedure to find the minima of the potential energy surface, which correspond to null forces on nuclei. Hereafter we will indicate the set of atomic and electronic coordinates dropping the braces, just to have a more handful notation. The procedure can be summarized in the following steps:

1. We calculate the electronic ground state energy $E_0(\mathbf{R})$ for a given atomic configuration, say \mathbf{R}_0 , keeping the nuclei fixed, by means of equation (2.8).

2. We expand the potential energy acting on nuclei up to the second order around \mathbf{R}_0 :

$$E_0(\mathbf{R}) + V_{NN}(\mathbf{R}) = E_0(\mathbf{R}_0) + V_{NN}(\mathbf{R}_0) + \sum_I \left(\frac{\partial(E_0 + V_{NN})}{\partial \mathbf{R}_I} \right)_0 \mathbf{u}_I + \frac{1}{2} \sum_{IJ} \left(\frac{\partial^2(E_0 + V_{NN})}{\partial \mathbf{R}_I \partial \mathbf{R}_J} \right)_0 \mathbf{u}_I \mathbf{u}_J \quad (3.5)$$

where $\mathbf{u}_I = \mathbf{R}_I - \mathbf{R}_0$, where the terms $\left(\frac{\partial^2(E_0 + V_{NN})}{\partial \mathbf{R}_I \partial \mathbf{R}_J} \right)_0$ are called Hessian matrix elements. The energy gradient is then calculated and put to zero to deduce the set of atomic equilibrium position.

3. To reach the minimum energy structure the procedure is iterated until the gradient is near to zero within a chosen precision at equilibrium (other checking conditions are often implemented in the codes which apply the Quasi-Newton procedure).

In this procedure we are assuming to start from a configuration which is near to the equilibrium one and that the potential energy surface is smooth and not degenerate, in order to justify the second order expansion. If this is not the case, codes often implement a step control to be given as an input, i.e. a limit on the maximum displacement that can be obtained in a single step, to avoid to skip the minimum. We still have not introduced the important computational features of the Quasi-Newton method: as the task of calculating directly the gradient and the Hessian elements is really demanding, the Quasi-Newton method goes through an analytical calculation of the gradient at each step of the procedure (which is the less demanding in terms of operations than the Hessian), while gives the Hessian an empirical form in the first step, which then is updated at each step of the procedure. The gradient and Hessian calculations are treated in the following sections.

Gradient calculation

We consider now the electronic Hamiltonian H_e of equation (2.8) and the nuclear-nuclear interaction term V_{NN} ; for the ground state energy we have:

$$\langle \Psi_0(\{\mathbf{r}\}, \{\mathbf{R}\}) | H_e + V_{NN} | \Psi_0(\{\mathbf{r}\}, \{\mathbf{R}\}) \rangle = E_0(\mathbf{R}) + V_{NN}(\mathbf{R}) \quad (3.6)$$

If we now derive expression (3.6) with respect the atomic positions and remember that the second member of equation (3.6) is the potential for the nuclei, we find that the force acting on the nuclei is:

$$\begin{aligned}\mathbf{F}_i = -\frac{d(E_0 + V_{NN})}{d\mathbf{R}_I} &= -\langle \Psi_0(\{\mathbf{r}\}, \{\mathbf{R}\}) | \frac{d(H_e + V_{NN})}{d\mathbf{R}_i} | \Psi_0(\{\mathbf{r}\}, \{\mathbf{R}\}) \rangle \\ &\quad - 2 \langle \frac{d\Psi_0(\{\mathbf{r}\}, \{\mathbf{R}\})}{d\mathbf{R}_i} | H_e + V_{NN} | \Psi_0(\{\mathbf{r}\}, \{\mathbf{R}\}) \rangle \quad (3.7)\end{aligned}$$

where the scalar product is meant to be on electron coordinates, and for simplicity we have assumed $\Psi_0(\mathbf{r}, \mathbf{R})$ to be a real valued function. Equation (3.6) is the working equation to find the energy gradient. It would be simpler to deal only with the first term of the second member of equation (3.7) (usually called Hellman-Feynman term [61]), i.e. if $\Psi_0(\mathbf{r}, \mathbf{R})$ is independent from atomic position, but this is quite never the case in a process of geometric optimization. A mismatch between the Hellman-Feynmann term and energy derivatives practically always arises, due to the second term of the second member of equation (3.7) (the so called Pulay-forces [61]).

Hessian calculation

In the quasi-Newton approach the Hessian matrix elements are often given an empirical form in the fist-step of geometric optimization process. If gradient calculation (as explained in the previous section) can be preformed directly in cartesian coordinates, a workable empirical form for the Hessian is often given in internal coordinates (introduced in the first section of this chapter). Some of the mostly used formula for the empirical matrix elements in internal coordinates has been given by Shlegel [62, 63] and Lindh [64]. One may guess that working in internal coordinates is computationally hard because, to coherently use the Hessian matrix element, we have to refer the Hessian to the cartesian axes. Indeed, it can be shown that this transformation is less expensive then the rough calculation of Hessian in Cartesian coordinates [65]. Even for the recalculation of the Hessian during each step of the geometric optimization different techniques have been developed: examples are given by Broyden technique [51], Schlegel technique [66] and symmetryc Powell scheme [67].

Chapter 4

Structural and electronic properties of bulk germanium crystal

4.1 Introductory considerations

Early experimental works on the electronic properties of germanium date back prior to the 50's. In those years, experimental efforts were mainly addressed to estimate the magnitude of germanium bulk lattice parameter and the behaviour of bulk energy bands, but the absence of highly purified germanium samples left open questions on the validity of the results. On the other hand, theoretical modelization of band structure often consisted in assuming the valence and the conduction band edges to occur at the central point of the first Brillouin zone [68]. With these methods the first crude but realistic fundamental band gap estimate was done by Bardeen in an unpublished article; the estimate was of about 0.72eV , as reported by Shockley [69]. It took few years to realize that the germanium bulk band structure could present an indirect fundamental gap [70], as successively demonstrated experimentally by Mcfarlane in 1957 [71].

One of the most important milestones in the experimental analysis of germanium bulk band structure dates back to 1953, when Dresselhaus, Kip and Kittel [72] observed for the first time cyclotron resonance

	Experimental value	Reference
Lattice parameter	5.658 Å	[80]
Fundamental gap	0.744 eV	[76]
Optical gap	0.898 eV	[76]

Table 4.1: Experimental values for the lattice parameter, fundamental and optical gaps for germanium crystal.

in germanium crystals. The study of this effect lead the authors to give one of the first complete experimental and theoretical description of germanium bulk valence band structure at $\mathbf{k} = \mathbf{0}$ of the first Brillouin zone in 1955 [73]. The general modellization of spin-orbit effect in zincblend and diamond structures was discussed in the same year by Dresselhaus [74]. Meanwhile, in 1952, Straumanis and Aka [75] studied for the first time germanium bulk structure in 99.99% purity conditions, deducing a lattice parameter $a = 5.645\text{\AA}$ at room temperature. In 1959 Zwerdling et al. [76] measured with magnetotransmission experiments the germanium bulk fundamental gap, giving a value of 0.744eV at 1.5 K, and for the optical (direct) gap a value of 0.898eV at 1.5 K. These experimental and theoretical efforts started a new era of study of germanium bulk properties. It took a decade from these pioneristic works to develop numberless new theoretical modelizations and calculations. Main examples of improved calculations are the works of Cardona and Pollack [77], that in 1966 used a mix of empirical and theoretical techniques within a $15 \mathbf{k} \cdot \mathbf{p}$ method to reproduce germanium bulk band structure, and of Chelikosky and Cohen [78], that in 1976 used an empirical non-local pseudopotential to reproduce germanium bulk band structure. With similar methods, in 1982 Yin and Cohen[79] reproduced theoretically, with very good precision, the experimental value of the germanium bulk lattice parameter. Refined experiments on the germanium bulk lattice parameter were performed in 1975 by Baker et al. [80], giving a value for the lattice parameter of 5.658 Å. We sum up some experimental data of germanium bulk properties in Table 4.1. Up to mid '80s the electronic band structure calculations, exploiting both extended or localized basis sets, were essentially semiempirical

in nature, i.e. they adjusted specific quantities to put to best the full band structure against suitable experimental information. The successive decades have seen the birth of ab-initio self-consistent theoretical calculations. In these ab-initio calculations the goal is the reproduction of experimental data without using, at least ideally, any type of empirical correction. Under this perspective, density functional theory and its features (born in the mid of the '60s and nowadays at the heart of heavy numerical calculations) have become essential tools also due to the increase of computational capabilities.

In spite of its geometrical simplicity, ab-initio calculations for germanium bulk often reached different results. We cite as examples of these ab-initio calculations the works of Yang et al. [81], Hummer et al. [82] and Sakata et al. [83]. Yang et al. evaluated Ge crystal indirect and direct gap values to be respectively 0.79eV and 0.96eV , within a hybrid functional calculation implementing spin orbit coupling, but without relaxing the geometrical structure; Hummer et al. instead found values of 0.85eV and 0.94eV for the Ge crystal indirect and direct gaps within a hybrid functional calculation with no spin orbit coupling, but without relaxing the geometrical structure because of the difficulty of reproduction of the lattice parameter from ab-initio techniques; Sakata et al. compared the results of HSE06, LDA, GGA and MGGA functionals finding that each of these functionals highly miscalculated either the lattice parameter or the band gaps if no empirical correction was implemented.

In the following of this chapter we will present our results for the ab-initio evaluation of the electronic band structure of Ge and show in depth the difficulties hidden in ab-initio calculations and the solutions to these problems.

4.2 Ab-initio calculation of Ge bulk structural and electronic properties

We describe in this section our calculation of germanium bulk properties obtained within the Density Functional Theory scheme, as introduced in section 2.2. Despite the Ge bulk geometrical structure of Figure 1.1 contains only two atoms per primitive cell, the reproduction of the experimental data of

table 4.1 is an hard task yet. In fact, it is widely known (see [84, 85, 86] for instance) that germanium is very difficult to be handled in density functional calculations, because great part of the available exchange-correlation functionals (LDA,GGA as presented in section 2.4) do not correctly reproduce basic properties such as lattice parameter and band gaps. Recent work has traced many of the errors in calculations to violations of conditions of the exact functional by certain formulations of LDA and GGA functionals [33]. These violations mainly imply a strong, but unphysical, electronic delocalization [32]. This great electronic delocalization leads toward a metallic behaviour, which is not compatible with the semiconductive nature of Ge bulk. We now present DFT calculations performed within LDA and GGA schemes as examples of these miscalculations.

LDA and GGA approximations for Ge-DFT calculation

We start from the Ge bulk configuration of Figure 1.1. We test LDA and GGA exchange-correlation functionals with QUANTUM ESPRESSO code. The GGA and LDA forms that we use are, respectively, the PBEsol (Perdew–Burke–Ernzerhof [54] functional optimized for solid-state calculations) and the PZ (Perdew-Zunger [53]) functional. For each functional, we need a properly generated pseudopotential to be used in equation 2.8. Usually, pseudopotentials for PBEsol and PZ are generated in Projector-Augmented-Waves (PAW) or Norm-Conserving (NC) schemes (see discussion in section 2.4). Projector-Augumented-Waves pseudopotentials for Ge bulk include 3d,4s and 4p atomic orbitals as valence states. Norm-Conserving pseudopotentials for Ge bulk include only 4s and 4p atomic orbitals as valence states. For both LDA and GGA exchange-correlation functionals we test the two pseudopotential generation schemes.

In any of the tested cases, our first calculation concerned convergence of the Ge bulk ground state energy with respect to the plane-waves basis-set energy cutoff, for the representation of the crystal wavefunctions, and \mathbf{k} -points grid dimension for the evaluation of the integrals. The energy cutoff, usually expressed in Rydberg, determines the maximum modulus of the wave-vector \mathbf{k} characterizing the plane-wave basis-set, therefore establishing its length. The \mathbf{k} -points grid in the first Brillouin zone

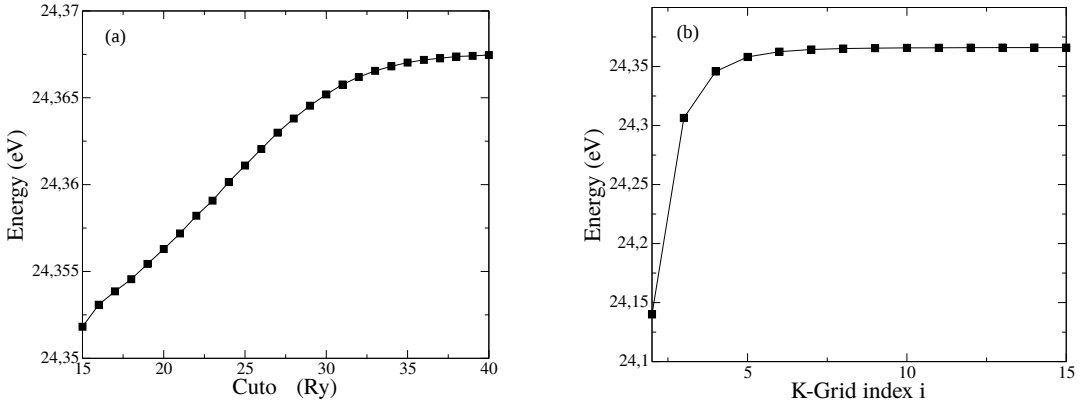


Figure 4.1: (a) Ge bulk ground-state energy (modulus) per simulation cell vs energy cutoff of the plane waves, for PZ functional with norm-conserving pseudopotential. (b) Ge bulk ground-state energy (modulus) per simulation cell vs Monkhorst-Pack mesh of dimensions $i \times i \times i$ along the axis $\mathbf{k}_x, \mathbf{k}_y, \mathbf{k}_z$ of Figure 1.2, for PZ functional with norm-conserving pseudopotential.

is generated within the Monkhorst-Pack method (see section 2.7) and it is of dimension $ixixi$, where i is an integer number that indicates the size of the mesh along the axes $\mathbf{k}_x, \mathbf{k}_y, \mathbf{k}_z$ of Figure 1.2. The convergence tests provide confidence of the Ge bulk ground state energy against change of basis-set cutoff and the \mathbf{k} -point grid index i . We should thus have a reasonable estimate of the precision of the calculation as function of the choice of two parameters.

For each value of the energy cutoff and mesh of the Monkhorst-Pack grid, we use the Ge bulk primitive cell of Figure 1.1 (a) as our simulation cell to solve the Kohn-Sham equations of equation (2.8). We then calculate the minimum of the Ge bulk ground-state total energy per simulation cell with no constraint on cell parameters. We find that values of cutoff around $35 - 40 Ry$ and of i around $5 - 6$ guarantee a good precision ($10^{-2} eV$) on the calculation of ground state energy per simulation cell. The results of the convergence tests in the case of PZ functional with norm-conserving pseudopotential are presented in Figures 4.1 (a) and (b). We can now proceed to evaluate the geometric optimization of the simulation cell edges (as explained in chapter 3) and the electronic band structure (as explained in chapter 2) for germanium bulk structure. Exploiting the PBEsol and PZ functionals and norm-conserving pseudopotentials, by the QUANTUM ESPRESSO code using a cutoff of 30 Rydberg and a

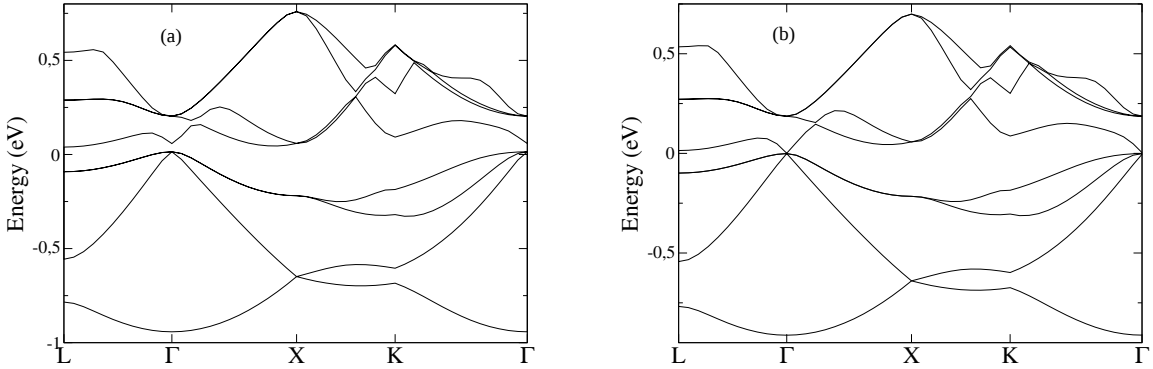


Figure 4.2: Ge bulk electronic band structure, obtained with a cutoff of 30 Rydberg and a 6x6x6 Monkhorst-Pack grid, using (a) the LDA-PZ functional and (b) the GGA-PBEsol functional.

Monkhorst-Pack grid mesh of dimensions 6x6x6 we have obtained the optimized geometrical structure of Ge given in Figure 1.1 with lattice parameter 5.728Å for PBEsol and 5.582 for PZ. For comparison, we notice that the experimental lattice parameter of Table 4.1 is 5.658Å. These result are compatible with the result obtained by Hummer et al. [82], showing that our calculation with GGA-PBEsol functional overestimates the lattice parameter of 1.2% whereas with LDA-PZ functional underestimates the lattice parameter of 1.3%. As the band structure is particularly sensitive to the lattice parameter value, we have the first prevision that we need to implement, as shown in the calculation below, a different exchange-correlation functional to reproduce the lattice parameter value within higher precision.

We now perform the band structure calculation for the Ge bulk configuration of Figure 1.1, as obtained with PBEsol and PZ functionals with norm-conserving pseudopotentials, along the \mathbf{k} -path inside the first Brillouin Zone shown in Figure 1.2. Using coherently, for each functional, the relaxed lattice parameters reported above, we obtain, for GGA-PBEsol functional a *metallic* band structure and for the LDA-GGA functional a very small fundamental band gap of 0.04eV. The result is the same for PAW pseudopotentials. This result is incompatible with germanium semiconductive nature and demonstrates that LDA and GGA exhang-correlation functionals are unable to describe the electronic properties of germanium. We show the results of band structure calculation with LDA-PZ and GGA-PBEsol and a norm-conserving pseudopotential in Figure 4.2. From Figure 4.2 we see that the values

of the direct and indirect gaps are $E_{\Gamma-\Gamma}^{PZ} = 0.04\text{eV}$, $E_{\Gamma-\Gamma}^{PBEsol} = 0\text{eV}$, $E_{L-\Gamma}^{PZ} = 0.015\text{eV}$, $E_{L-\Gamma}^{PBEsol} = 0\text{eV}$. For comparison, the experimental values are $E_{\Gamma-\Gamma}^{exp} = 0.898\text{eV}$, $E_{L-\Gamma}^{exp} = 0.744\text{eV}$. Having proved that LDA and GGA functionals are not able to reproduce one-electron germanium properties, we move toward a hybrid expression for the exchange-correlation functional for the calculation of Ge structural and electronic properties.

Hybrid functionals for Ge-DFT calculation

To test the effect and performance of hybrid functionals (introduced in section 2.4), we exploit now also the CRYSTAL14 code because, even if QUANTUM ESPRESSO implements hybrid functional calculations, it does not implement geometrical optimization with this type of functionals. As in LDA and GGA case, we start performing a geometrical optimization of the germanium bulk structure of Figure 1.1, using a Monkhorst-Pack grid of dimensions 6x6x6. The CRYSTAL14 code adopts localized-Gaussian-orbitals basis sets, as discussed in chapter 2. We use the Triple-valence basis set of reference [87] in our calculation, suitable for all-electron calculations, so that it does not use any pseudopotential. Our aim is to test different hybrid functionals to verify which one is the best to reproduce experimental data, so we perform geometric optimization with B3LYP[88], PBE0[89], HSEsol and HSE06[34, 35, 36, 90]. The results for the lattice parameter obtained after optimization of the geometric structure are reported in Table 4.2. We see from table 4.2 that the exchange-correlation functional which best reproduces the experimental lattice parameter is the HSE06 (within 0.1% error). After optimization of the geometrical structure, we compare the performances of the various hybrid functionals on the reproduction of the electronic band structures and the band gaps. We perform band calculations along high symmetry points and lines reported in Figure 1.2. For each functional we have evaluated the electronic band structure exploiting simulation cells with the appropriate lattice parameters of table 4.2. We present two examples of band structures (obtained with B3LYP and HSE06) in Figure 4.3.

Functional	Optimized lattice parameter (\AA)
B3LYP	5.696
HSE06	5.642
HSEsol	5.604
PBE0	5.632

Table 4.2: Relaxed lattice parameters for bulk Ge corresponding to different hybrid functionals, obtained using basis set of reference [87] with a Monkhorst-Pack grid of dimensions 6x6x6.

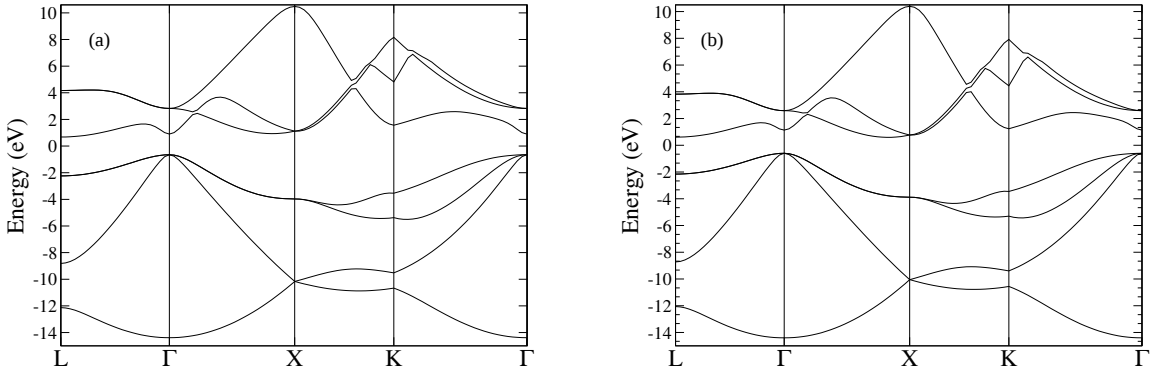


Figure 4.3: Ge bulk band structure, obtained using basis set of reference [87] and a 10x10x10 Monkhorst-Pack grid, with (a) B3LYP functional and (b) HSE06 functional.

We report in Table 4.3 the band gaps obtained by the use of B3LYP, HSE06, HSEsol and PBE0 functionals. The most evident result is that the gaps are highly overestimated. We then checked whether this problem could be healed adopting in the calculation a most accurate atomic basis set. We thus adopt the basis set of reference [91]. This basis set is a pseudopotential basis set, suitable for calculations with hybrids exchange-correlation functionals, particularly with the HSE06 one. We thus obtain the band structure of Figure 4.4. The main results of Figure 4.4 are that the calculated direct and indirect gaps are in good agreement with experimental values and that the bandwidth and degeneracy of the bands agree with the ones obtained by Chelikosky and Cohen [78]. Therefore,

Functional	Direct Gap $E_{\Gamma-\Gamma}$ (eV)	Indirect Gap $E_{L-\Gamma}$ (eV)
B3LYP	1.285	1.232
HSE06	1.783	1.191
HSEsol	1.938	1.087
PBE0	2.226	1.670

Table 4.3: Gaps with different functionals. For comparison, $E_{\Gamma-\Gamma}^{exp} = 0.898eV$, $E_{L-\Gamma}^{exp} = 0.744eV$.

comparison with experimental results is satisfactory. We believe that HSE06, in conjunction to the use of the pseudopotential basis set of reference [91], is the exchange-correlation functional which best reproduces the experimental data of Ge bulk and we shall use it for the following calculations. The most important bonuses of the use of HSE06 echange-correlation functional are summarized in Table 4.4.

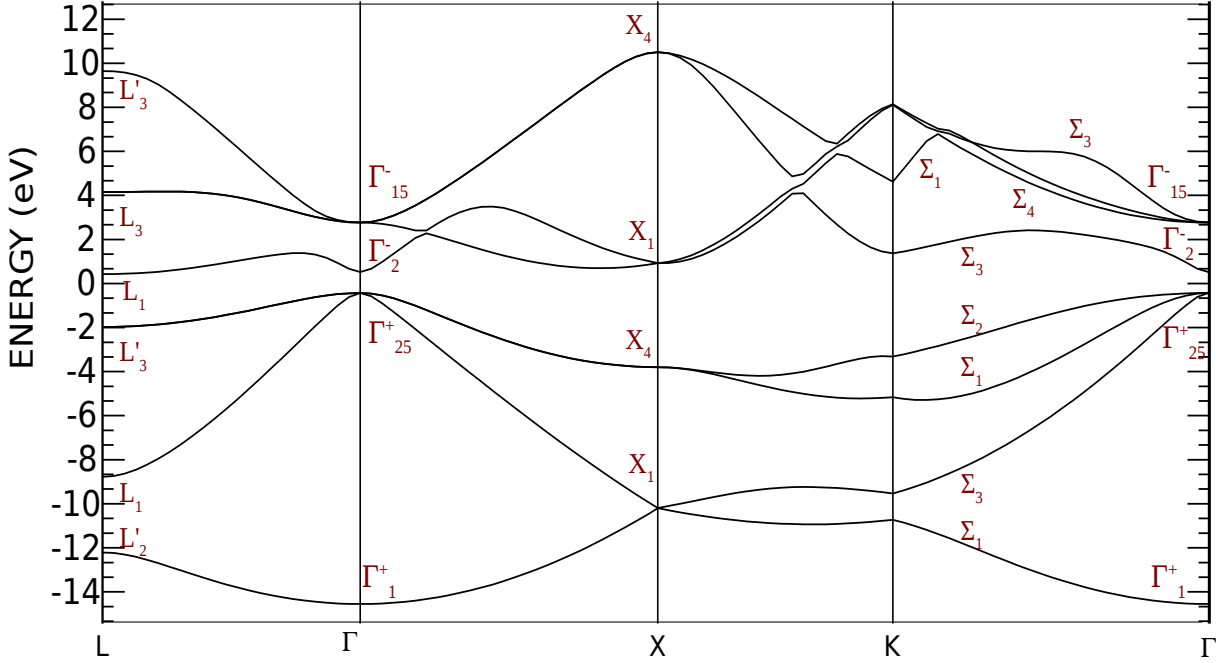


Figure 4.4: germanium bulk band structure, obtained using the pseudopotential-basis set of reference [91] with a 10x10x10 Monkhorst-Pack grid. Direct Gap= $E_{\Gamma-\Gamma}=0.957$ eV, Indirect Gap= $E_{L-\Gamma}=0.852$ eV. For comparison, $E_{\Gamma-\Gamma}^{exp} = 0.898eV$, $E_{L-\Gamma}^{exp} = 0.744eV$.

	Computed with HSE06	Experimental
Lattice parameter (\AA)	5.642	5.658
Fundamental/indirect gap (eV)	0.856	0.744
Optical/direct gap (eV)	0.952	0.898

Table 4.4: Comparison between experimental data and results of geometric optimization and band structure of germanium bulk, obtained using HSE06 with basis set of reference [91] and with a 10x10x10 Monkhorst-Pack grid.

Chapter 5

Structural and electronic properties of the (2x1)-(001) germanium surface

5.1 Introductory consideration

In this chapter we will study the Ge (001) surface, reconstructed in a p(2x1) asymmetric pattern, as shown in Figure 1.8 (d). As explained in section 1.2, the Ge (001) surface is obtained by the truncation of the Ge bulk structure orthogonally to the [0 0 1] direction: the result is a semi-infinite succession of Ge crystal planes, extending orthogonally to the [0 0 1] direction, below the surface plane, shown in Figure 5.1 (a). To evaluate the minimum energy configuration of the surface geometrical structure, i.e. the atomic relaxation, and successively the electronic properties of the Ge (001) surface, we have to simulate numerically the semi-infinite succession of Ge crystal planes of Figure 5.1 (a). Since the structural modifications due to the relaxation of Ge surface atoms involves mainly only the first 4/5 layers below the surface (as we will see later and as experimentally confirmed by high energy ion scattering experiments [92]), we can in practice approximate the semi-infinite system of Figure 5.1(a) with a finite system composed by a finite number of Ge layers, passivating the bottom surface with two Hydrogens per Ge atoms, as we will discuss in the following. The approximation of a finite number of

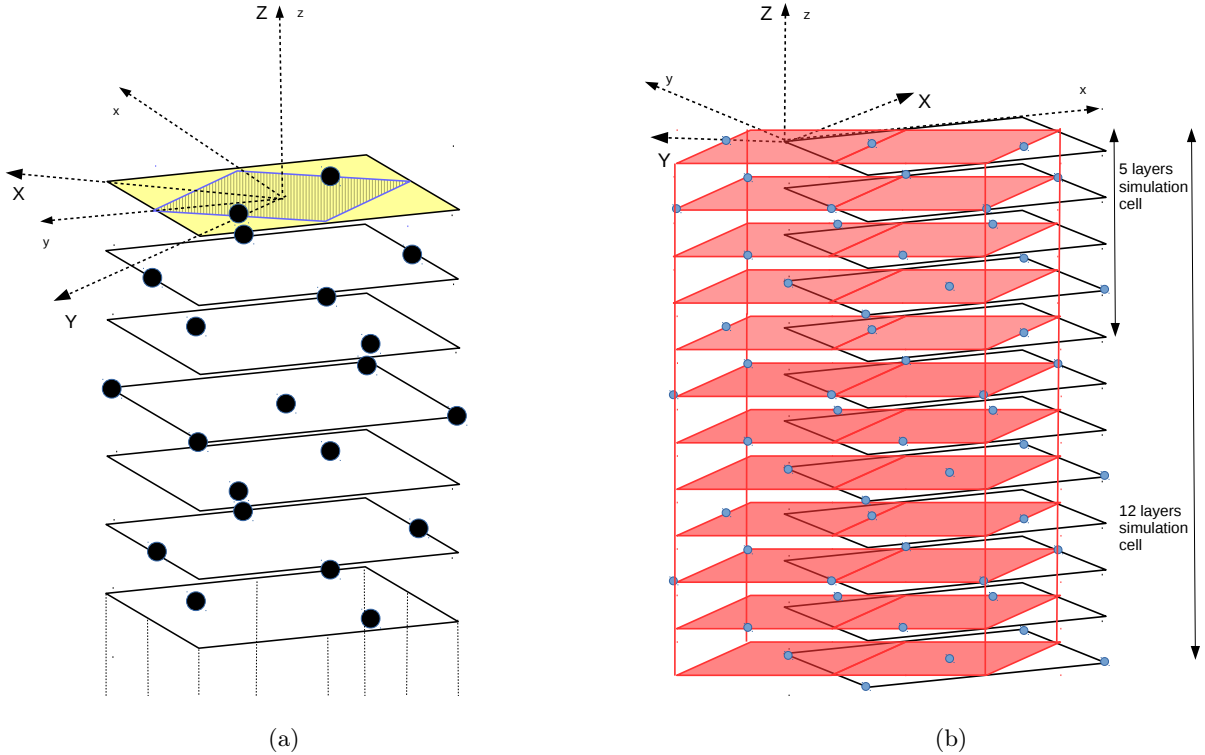


Figure 5.1: (a) Ideal semi-infinite succession of Ge crystal planes resulting after truncation of ideal bulk structure. The surface plane is coloured in yellow. The surface cell of Figure 1.8 (a) is reported in lined blue. (b) Finite succession of (2x1) Ge atomic crystal planes, coloured in red. The simulation cells for the Ge 5 layers slab (containing 10 Ge atoms) and for the Ge 12 layers slab (containing 24 Ge atoms) are contoured in red. Notice that the simulation cell for the Ge 5 layers is a subcell of the 12 layers one. For convenience, the coordinate system in (b) is shifted with respect to (a).

layers has been debated in the literature: as discussed by Radny et al. and Yan [93, 94, 95], the study of the properties of the germanium (001) surface is very sensitive to the number of layers implemented in the numerical simulations. In particular, a 5 layers slab approximation, i.e. a slab of width equal to the depth of the surface perturbation, is not sufficient to reproduce the structural relaxation and electronic properties of the Ge (001) surface with high precision. Anyway, in the following sections, we will first perform calculations on a Ge 5 layers and successively on a Ge 12 layers slab approximation to the semi-infinite p(2x1) Ge (001) surface (the asymmetric dimer configuration of the p(2x1) reconstruction scheme is obtained relaxing the degrees of freedom of the Ge atoms inside the simulations cells of

Figure 5.1 (b)). In fact, we can use the 5 Ge layers slab approximation to study *qualitatively* the most important features of structural relaxation and electronic properties of the Ge (001) surface with a smaller computational effort because of the smaller number of Ge atoms in the simulation cell (only 10 instead of 24). The *quantitative* analysis of these properties is demanded to the 12 Ge layers slab approximation.

5.2 Ge-(001) surface properties

As already mentioned in the first chapter of this thesis, the early important studies of the Ge-(001) surface date back to the 50's, when Schlier and Farnsworth [4] first proposed dimerization of surface atoms in germanium (as in silicon), i.e. neighbouring Ge surface atoms approach towards one another forming a chemical bond in order to lower the total energy of the system. Since then, as the semiconductor industry has longly searched for alternatives to the Si channel in field-effect transistors, many efforts have been addressed to study the properties of the Ge (001) surface. In fact, Ge (001) surface has the advantage that it is much less reactive with oxygen than silicon and can form a more stable interface with many large permittivity (high-k) dielectrics. Another recent source of interest for the Ge (001) surface comes from photonics [3]. Looking at the most important theoretical studies regarding the Ge (001) surface, already in 1979 Chadi [10] proposed that the surface dimers of Si and Ge(001) could buckle, i.e. create an asymmetric configuration where one atom is nearer to the surface than the other, using a tight binding scheme for his calculations. As already mentioned in the first chapter of this thesis, soon after in the 80s Tromp et al. [38] confirmed experimentally the asymmetric dimerization of top Ge atoms of the surface proposed by Chadi. In 1986 Pollmann and Krüger published the first of three most important works ([96, 11, 97]) on the p(2x1) Ge (001) surface calculating, via the Green's function method and empiric approach, the band structure of the Ge (001) surface. In these works they showed that the band structure of the Ge (001) surface with asymmetric dimers exhibits semi-conductive behaviour; most important, they showed that the bands generated by the Ge orbitals of the dimers

merge into the Ge bulk projected bands at $\mathbf{k} = 0$. As we shall see in this thesis, this result is confirmed by our ab initio calculations. Meanwhile, in 1987 Kubby et al. [19] measured the Ge (001) surface fundamental (direct) gap to be around 0.9eV , confirming the results of Pollmann and Krüger, and in 1992 Rossmann et al. [98] measured the Ge asymmetric dimer length to be around 2.46\AA .

Lately, the development of ab initio calculation techniques has renewed the interest in the computation of the Ge (001) surface properties, in order to gain further information on surface states potentiality and explore them for the design of new devices. We refer to the already mentioned works of Radny et al. and Yan [93, 94, 95] and of Hatch [99] as examples of recent ab initio evaluation of Ge (001) surface properties arriving to surface band structure in disagreement with experimental data, essentially because of difficulties regarding the proper choice of the exchange-correlation functional as already encountered in the case of bulk germanium. The ab initio reproduction of Ge (001) surface electronic bands remains thus an open problem.

5.3 Preliminary study of the 5 layers germanium slab

The number of 5 atomic layers, properly terminated by Hydrogen passivation was chosen to first represent the semi-infinite succession of Ge crystal planes of Figure 5.1 (a). The reason is that, as already mentioned in the introduction to this chapter, the fourth-fifth layers are often the discriminant layers after which the surface relaxation and reconstruction perturbations decay (see for instance the Ge (001) p(2x1) surface reconstruction in the work of Hatch et al. [17]) leaving place to the ideal bulk geometry for the successive layers. Moreover, as shown in Figure 1.3, the number of 5 layers is the least necessary choice to reproduce the [0 0 1] periodicity of the ideal bulk underlying the Ge (001) surface.

To study the p(2x1) asymmetric pattern of Figure 1.8 (c) with a 5 Ge layers slab, we adopt the simulation cell of Figure 5.1 (b). When we consider the Ge 5-layers slab, we see that the top and the bottom layers of the slab present two pending bonds (unsaturated) per Ge atom, which were saturated in the ideal bulk structure before the truncation. Since our aim is to reproduce the p(2x1) asymmetric

pattern of Figure 1.8 (d), we require the presence of the two pending bonds per Ge atom on the top layer of the Ge slab, because they are responsible for the dimerization of surface Ge atoms as explained in section 1.2. On the contrary, we want to avoid the effects of the two pending bonds per Ge atom present in the bottom layer of slab. To overcome this problem, it is common practice in such calculations [93] to *passivate* the bottom layer of Ge atoms with two Hydrogen atoms. Passivation means the creation of an outer layer of shield material that is applied as a microcoating. The choice of two Hydrogens atoms per Ge atom to saturate the pending bonds on the bottom layer of the Ge crystal slab has been investigated testing also, for comparison, the passivation by means of one Hydrogen per Ge atom. This last type of passivation was found to lead to undesired states in the surface electronic states. In general, we require that the relaxation, reconstruction and electronic properties of the Ge (001) surface are not affected by the type of passivation. We thus choose to attach two Hydrogens atoms to each bottom layer Ge; the Hydrogen-germanium bonding is very strong and spatially localized, so that it does not affect top surface dimerization and surface electronic properties. To efficiently simulate the p(2x1) asymmetric pattern of Figure 1.8, we start from the atomic configuration of the (2x1) simulation cell of Figure 5.1 (b) and arrange the surface atoms of the top layer of the Ge crystal slab into asymmetric dimers with dimer length and tilt angle equal to the ones of Figure 1.7. We use this guess configuration, which we expect to be similar to the minimum energy configuration, as the starting point for our geometrical optimization of the structure, in order to save computational time. Notice that QUANTUM ESPRESSO and CRYSTAL codes, being three-dimensional codes, can only simulate systems with three-dimensional periodicity. This means that, if we want to simulate a two-dimensional periodic system, we are forced to reproduce it periodically also in the third dimension. To have a surface calculation we must separate the periodical copies of the system along the Z axis by a sufficient amount of space, as shown below.

Surface geometry optimization of the p(2x1) Ge-(001) surface

The geometric optimization of the 5 Ge crystal layers slab is performed with QUANTUM ESPRESSO, using PBEsol as exchange-correlation functional and norm-conserving generated pseudopotentials for Ge

atoms. In the present step we disregard the relativistic effects due to spin-orbit interaction. As explained in the previous section, we minimize the total energy of the system to find the stable geometrical configuration, starting from a guess structure that we expect to be as near as possible to the stable configuration. The dimensions of the p(2x1) simulation cell of Figure 5.1 are the same ones of Figure 1.8 (c), provided that the lattice parameter is coherently chosen to be $a = 5.758\text{\AA}$, i.e. equal to the bulk relaxed lattice parameter obtained exploiting the PBEsol exchange-correlation functional (indeed, in section 4.2 we found $a = 5.728\text{\AA}$. We use here the improved value $a = 5.758\text{\AA}$ that will be deduced in section 7.2. We refer to that section also for the justification of this improvement). In the geometrical optimization process we choose to keep the dimensions of the surface simulation cell fixed and relax only the degrees of freedom inside the cell. In the geometrical optimization we use an energy cutoff of 35 Rydberg for the plane wave basis set and a Monkhorst-Pack grid of dimensions 6x3x1, with each index indicating the dimension of the grid along the (K_X, K_Y, K_Z) direction of Figure 1.9. The dimension of the Monkhorst-Pack grid is chosen in the form $i \times \frac{1}{2} \times 1$, where i is a integer number, because the Brillouin zone of the surface cell of the p(2x1) pattern is twice longer in the K_X direction than in the K_Y direction, as shown in Figure 1.9. The distance between two periodically reproduced Ge crystal slabs along the Z direction has been varied until the ground state energy calculation did not change up to a factor of 10^{-2}eV . We find that a distance of 25\AA is sufficient for the needed precision. Moreover, we consider the geometric optimization successful when the total energy difference between two successive geometric optimization steps is smaller than 10^{-4}Ry and when all the components of the force acting on each atom are smaller than 10^{-3}Ry/Bohr . With these computational parameters we perform geometrical optimization of the internal degrees of freedom of the surface simulation cell of Figure 5.1, obtaining the structure of Figure 5.2.

Electronic band structure of the p(2x1) Ge-(001) surface

Once obtained the minimum energy configuration of the p(2x1) reconstruction of the Ge (001) surface, we are ready to calculate the band structure of our 5-layers Ge slab. To perform the electronic band

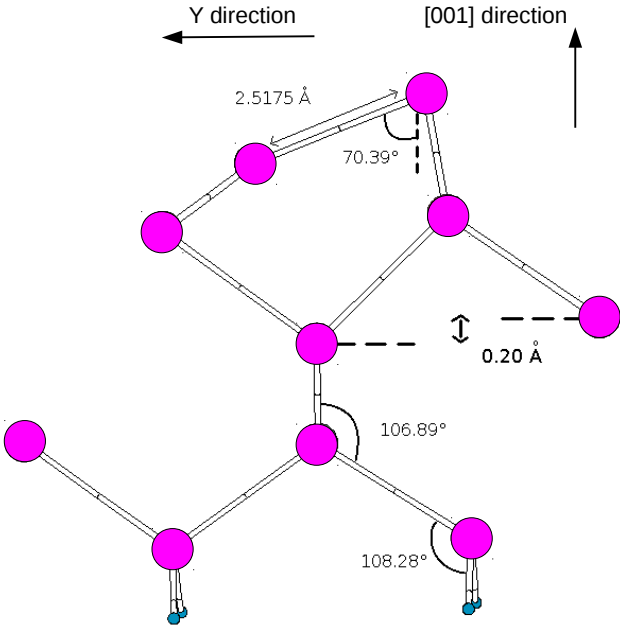


Figure 5.2: Side view of the geometrical optimization of the internal degrees of freedom of the surface cell of the p(2x1) reconstruction pattern, performed with PBEsol using a cutoff of 35 Rydberg and a Monkhorst-Pack grid of dimensions 3x6x1. The dimer length value is found to be 2.518Å against a 2.46Å experimental value [98]. The dimer bond angle is found to be 19.61° against a 19° experimental value [100].

calculation we adopt the same calculation method that gave us good result as regards the bulk band structure (in chapter 4). We therefore adopt the CRYSTAL14 code, using HSE06 as exchange-correlation functional and the pseudopotential-basis set of reference [91]. In principle, to coherently perform band calculation on the (2x1) surface cell of Figure 1.8 with HSE06, we should use the lattice parameter obtained by geometric optimization of Ge bulk structure with HSE06. Anyway, as explained in section 5.3, the Ge 5 layer slab approximation is intended to give a qualitative sketch of the properties of the Ge (001) surface; therefore, we postpone the question of how to choose the right lattice parameter to perform band structure calculation to the Ge 12 layers slab approximation.

We compare the p(2x1) Ge (001) surface band structure with the Ge bulk band structure projected on the surface band path, as explained in section 2.8. The result is shown in Figure 5.3.

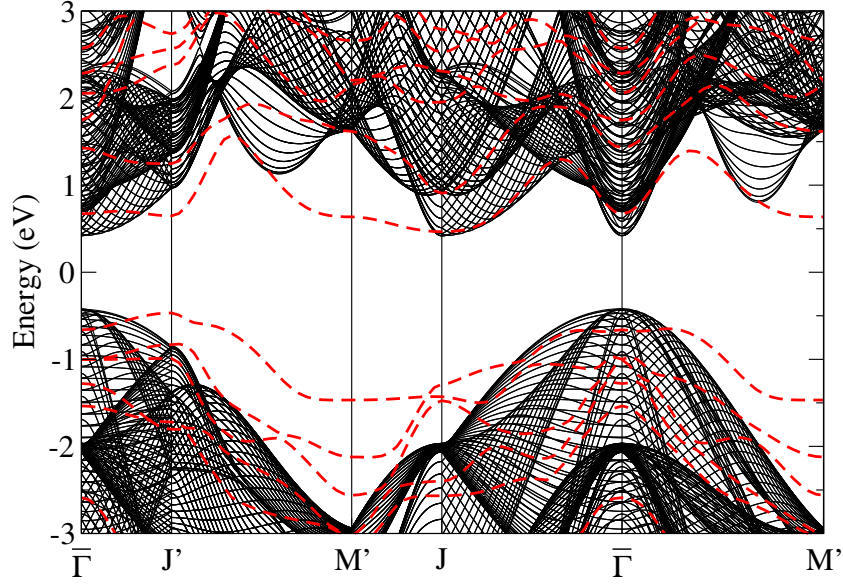


Figure 5.3: Projected band structure of the Ge crystal bulk on the surface Brillouin zone (black lines) and p(2x1) Ge (001) surface bands (red lines) in the 5 layers approximation. The bulk and surface electronic states are reported equalizing equalizing the Fermi levels.

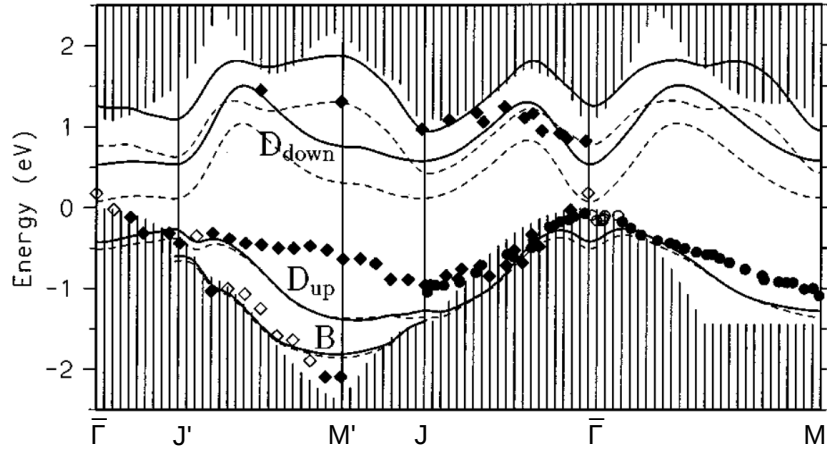


Figure 5.4: Bands for buckled dimer in Ge [101]. The bulk states are denoted by shaded areas, and surface states in the gap by lines. Bands denoted D_{up} and D_{down} surface states associated with the surface dantling bonds. The dashed lines are for the LDA (showing the zero-gap problem) and the solid lines are calculated in the GW approximation. Dots indicate experimental results referenced in [101].

The general shape of the electronic band structure is in good agreement with the original results of

Krüger and Pollmann [96], which we report in Figure 5.4 for comparison. A comparison between Figure 5.3 and Figure 5.4 shows that the shape of bottom conduction band and top valence band are in very good agreement. The immersion of valence surface band D_{up} into the bulk bands at $\bar{\Gamma}$ is more pronounced in Figure 5.4 than in Figure 5.3. Our band structure gives for the indirect fundamental gap the value $E_{gap} = 0.739\text{eV}$ between the bottom of the conduction band at J and the top of the valence band at J' . As we will see, the shape of the band structure and the value of the gap will be more realistic in the 12 layers approximation.

We resume all the results in Table 5.1.

Type	Dimer bond length (\AA)	Dimer tilt angle ($^\circ$)	Fundamental gap
Experimental	2.46[98]	14[2] or 19[100]	0.72[44] or 0.9[19, 44]
5 layers with Hydrogens	2.51	19.61	0.939

Table 5.1: Calculated dimer length, dimer tilt angle and surface band gap, in comparison with experimental values.

5.4 Quantitative study of the 12-layers germanium slab

As discussed in section 5.1, the number of 12 layers slab with H termination has been chosen to verify convergence of our results obtained for the case of the 5 layers germanium slab of the previous section.

We will consider in the following the 12 layers Ge slab simulation cell of Figure 5.1 (b). As in the 5 layers Ge slab, we passivate the bottom layer of the Ge 12 layers slab with two Hydrogen per Ge atom, thus saturating all the bottom surface dangling bonds; we then arrange the surface atoms of the top layer of the Ge crystal slab into asymmetric dimers with dimer length and tilt angle equal to the ones of Figure 1.7. This is the starting point for our geometrical optimization of the structure. The geometric optimization of the 12 Ge crystal layers slab is done by means of the QUANTUM ESPRESSO code, using PBEsol as exchange-correlation functional and norm-conserving generated pseudopotentials for

Ge atoms. We minimize the total energy of the system to find the stable geometrical configuration. The dimensions of the p(2x1) surface cell are the same of Figure 1.8, provided that the lattice parameter is coherently chosen to be $a = 5.758\text{\AA}$, i.e. equal to the bulk relaxed lattice parameter obtained with PBEsol exchange-correlation functional (indeed, in section 4.2 we found $a = 5.728\text{\AA}$. We use here the improved value $a = 5.758\text{\AA}$ that will be deduced in section 7.2. We refer to that section also for the justification of this improvement). In the geometrical optimization process we choose to keep the dimensions of the surface cell fixed and relax only the degrees of freedom inside the cell.

In order to generate high level accuracy of the results, in the geometrical optimization we use a cutoff of 100 Rydberg and a Monkhorst-Pack grid of dimensions 6x12x1, with each index indicating the dimension of the grid along the (K_X, K_Y, K_Z) directions of the first Brillouin zone (see Figure 1.9). The distance between two periodically repeated slabs has been increased from 25\AA , as in the case of the 5 layers approximation, to 30\AA . We consider the geometric optimization successful when the total energy difference between two successive geometric optimization steps is smaller than 10^{-6}Ry and when all the components of the force acting on each atom are smaller than 10^{-5}Ry/Bohr . With these computational parameters we perform geometrical optimization of the internal degrees of freedom of the surface cell of the p(2x1) pattern, obtaining the structure of Figure 5.5. To check the consistency and the computational stability of the geometrical structure of Figure 5.5, we repeat the geometric optimization varying the computational parameters *each one at a time*. We perform geometric optimization increasing the cutoff from 100Ry to 101Ry , doubling the Monkhorst-Pack grid dimensions from 12x6x1 to 24x12x1, changing the density mixing scheme during the SCF cycle, increasing the z-distance between two periodically repeated slabs from 30\AA to 31\AA and finally changing the solving precision in the SCF cycle. No differences are found within the requested precision on the total energy and on the forces in each change of computational parameters. Referring to Figure 5.5 (a) and (b), we can see that the perturbation induced by surface reconstruction decays rapidly within the first 5 layers, leaving place to the ideal bulk structure after the 5th layer. This is consistent with the result of Hatch et al. [17] and the experimental observations [92]. In details, referring to Figure 5.5 (b) we can see that, below the 5th

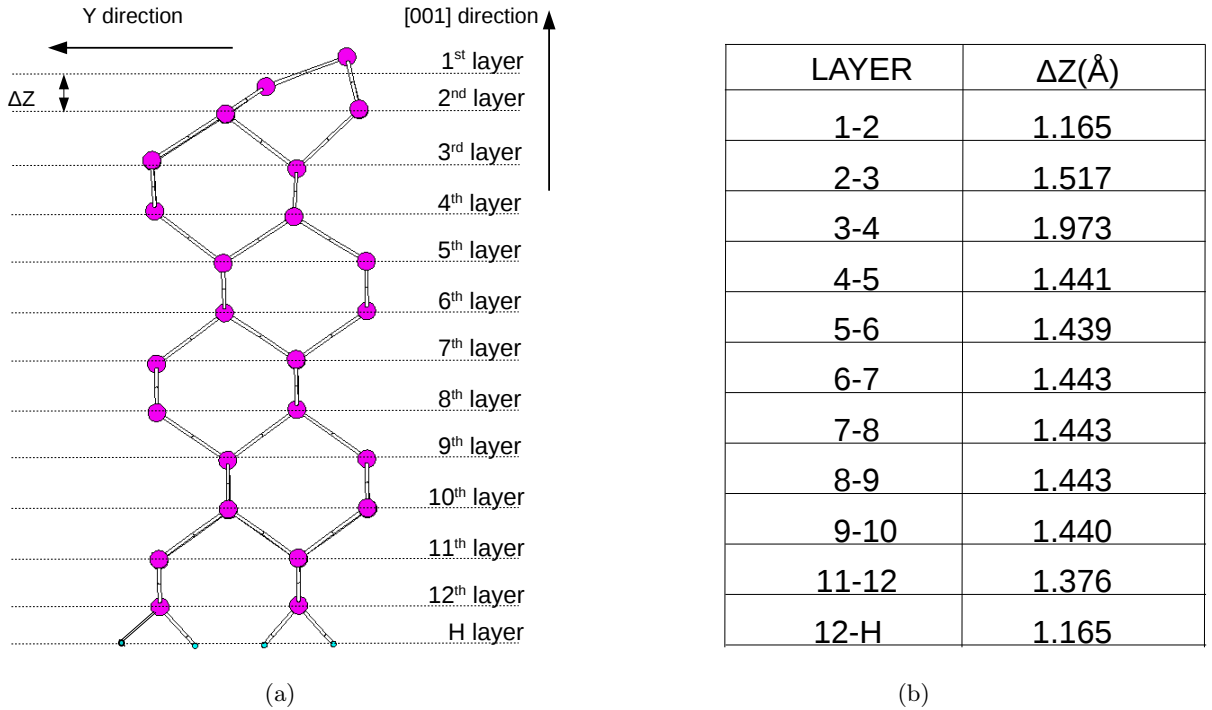


Figure 5.5: (a) Geometric optimization of p(2x1) Ge (001) surface in the 12 layers approximation (side view), performed with PBEsol using a cutoff of 100 Rydberg and a Monkhorst-Pack grid of dimensions 12x6x1. The dimer length is found to be 2.512 Å against the 2.46 Å experimental value [98]. The dimer bond angle is found to be 19.55 ° against the 19 ° experimental value [100]. The dashed lines represent schematically the optimized Ge atomic planes. (b) Distances along the [0 0 1] direction between different consecutive layers.

layer, the distance along the [0 0 1] direction between consecutive layers stabilizes around a value of 1.443 Å, according to the value of this distance in the ideal bulk configuration (1.439 Å). Anyway, we do not consider the fifth layer as part of the ideal bulk structure yet because the displacement of its two Ge atoms along the [0 0 1] direction with respect to the layer height is of 10^{-2} Å, whereas for the successive layers is of 10^{-3} Å. We also notice that the distance along the [0 0 1] direction between the eleventh and twelfth layer is 5% smaller than the 1.443 Å ideal bulk distance. We attribute this slight deviation from the ideal bulk behaviour to the presence of the Hydrogen passivation layer.

The band structure calculation of the p(2x1) Ge (001) surface starts from the geometrical structure

of Figure 5.5 and is done by means of the CRYSTAL14 code using HSE06 as exchange-correlation functional approximation and the same pseudopotential-basis set of reference [91] which we used to obtain the good results for the bulk band structure in chapter 4. As already pointed out in section 5.3, we cannot directly perform band calculation using HSE06 on the system optimized with PBEsol because the optimized PBEsol Ge bulk lattice parameter is 2% larger than the optimized HSE06 Ge bulk lattice parameter. In fact, the optimized Ge bulk lattice parameters corresponding to HSE06 and PBEsol are respectively 5.642 Å and 5.758 Å. We therefore make the following ansatz: performing a uniform scaling transformation on all the direct space vectors we transform the relaxed geometry obtained with PBEsol into the relaxed geometry corresponding to HSE06 geometric optimization. The uniform scaling transformation is defined as follows: for each position vector $\mathbf{r} = a\hat{X} + b\hat{Y} + c\hat{Z}$ belonging to the simulation cell of Figure 5.1 (b) we define a vector \mathbf{r}' such that:

$$\mathbf{r}' = \alpha \mathbf{r} \quad \alpha = \frac{5.642}{5.758} \quad (5.1)$$

The ansatz can be verified calculating, with HSE06, the magnitude of the forces acting on the transformed system. Indeed, the forces acting on the transformed configuration calculated with HSE06 are of the order of $10^{-4} Ry/Bohr$, so we are pretty confident in stating that our ansatz is correct. Performing a band calculation on the geometrical structure obtained thanks to the transformation of equation (5.1) we obtain the result of Figure 5.6. A comparison between Figure 5.6 and Figure 5.4 shows that the shape of the bottom conduction band and the top valence band are in very good agreement with the result of Pollman and Krüger of Figure 5.4. This indicates that the Ge 12 layers slab approximation is indeed a good approximation to the semi-infinite geometrical structure of Figure 5.1. The surface top band valence at $\bar{\Gamma}$ is practically indistinguishable from the bulk top valence band within 0.02eV (within our precision), therefore at $\bar{\Gamma}$ surface states and bulk states are mixed. Our band structure gives an indirect fundamental gap of $E_{gap} = 0.742eV$ between the lowest conduction band at J and the highest valence band energy, lying along the $\bar{\Gamma}$ -M' symmetry direction. We notice that in Kubby's work [19] it is stressed that the experimental value of the (direct) fundamental gap of 0.93V may be biased

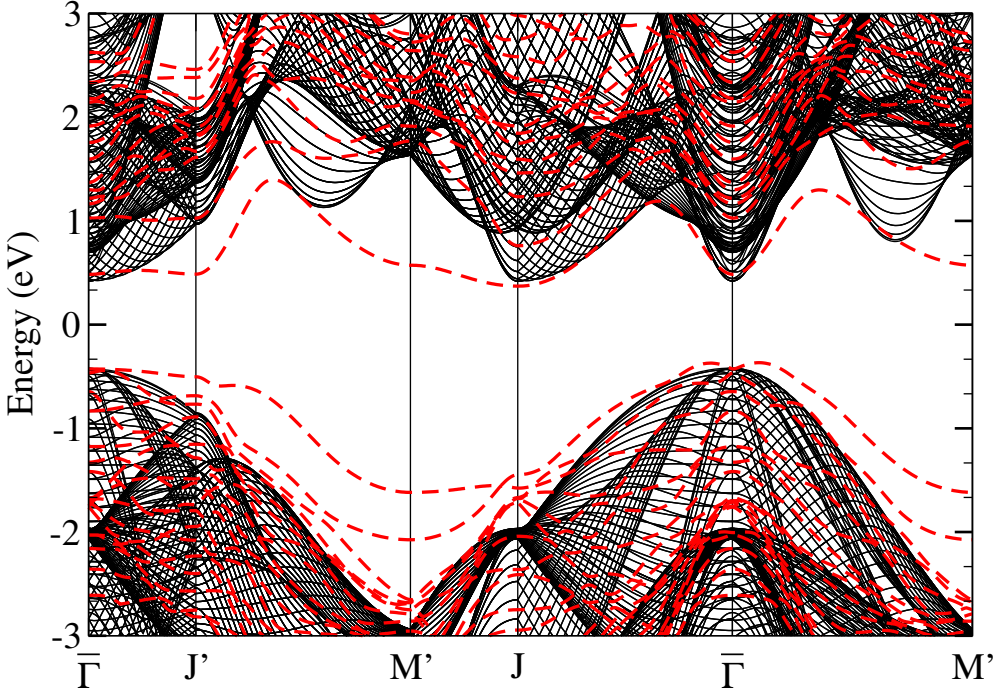


Figure 5.6: Ge bulk band structure projected on the (001) surface first Brillouin zone (black continuous lines) and p(2x1) Ge (001) surface bands (red dashed lines) for the 12 layers slab. The two band structures are compared equalizing the Fermi level.

by the high sensitivity of scanning tunnel microscopy technique to the Γ states. This means that the experimental 0.9eV value could represent the direct gap instead of the fundamental gap, therefore in agreement with our $E_{\bar{\Gamma}-\bar{\Gamma}} = 0.912\text{eV}$. In the absence of more confident experimental data, we think that our band structure is in good agreement with experimental data.

The contributions to the electronic density of Ge (001) surface states, in the energy range going from -3eV to 3eV , of the Ge dimer "up" and "down" atoms and of the first three Ge atomic layers defined in Figure 5.5 [obtained performing a Projected-Density-Of-States (PDOS)] is presented in the side panels of Figure 5.7. The PDOS of Figure 5.7 reveals that the (2x1) Ge (001) surface states are mostly localized on the first layer, but the components on the other two layers are not negligible, especially for the top valence band. As regards the projection on the Ge dimer atoms, the Ge surface top valence band wavefunctions are spatially localized on the "up" atom, whereas the bottom conduction eigenvectors are mostly localized on the "down" atom; this is in agreement with Figure 5.4 and with the results of

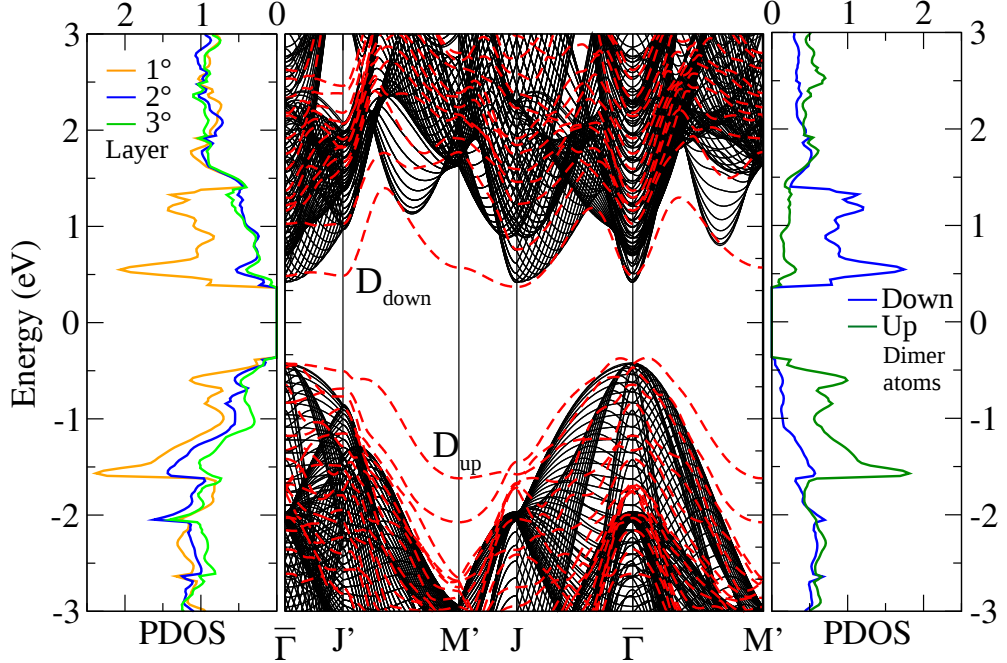


Figure 5.7: $p(2\times 1)$ Ge(001) surface band structure of Figure 5.6 in the energy range between -3eV and 3eV (in the central panel); in the same energy range the contributions to the electronic density (in states/eV/cell units) of surface states of the first three layers (in the left panel) and of the Ge dimer "up" and "down" atoms (in the right panel) are displayed.

Hatch [99]. We notice that two peaks in the density of states on the "up" atom of the Ge dimer are present at energies -0.6eV and -1.6eV in the valence region. In the work by Nelson et al. [16] it is reported evidence of surface resonances below the Fermi level, at energies -0.6eV and -1.3eV , with use of the ARPES technique. We consider this comparison as a hint of the goodness of our calculations.

Chapter 6

Theory of elastic deformations in crystals

6.1 Strain tensor

The mathematical description of deformations in solids requires the definition of the deformation vectors \mathbf{u} , which are given the difference between the positions of any material point before and after the deformation, in a given reference system (we use Cartesian coordinates (x, y, z) for simplicity):

$$\mathbf{u}_i(\mathbf{r}) = \mathbf{r}'_i - \mathbf{r}_i \quad (6.1)$$

where \mathbf{r}_i is the position of the point before the deformation and $\mathbf{r}'_i = \mathbf{r}'_i(\mathbf{r})$ is the position after the deformation. If we consider an infinitesimal deformation, the squared modulus of the distance between two infinitesimally near points $\mathbf{r}_1, \mathbf{r}_2$ before and after deformation can be written as:

$$d\mathbf{l}^2 = d(\mathbf{r}_1 - \mathbf{r}_2)^2 = \sum_{i=1}^3 d\mathbf{x}_i^2 \quad d\mathbf{l}'^2 = d(\mathbf{r}'_1 - \mathbf{r}'_2)^2 = \sum_{i=1}^3 d\mathbf{x}'_i^2 = \sum_{i=1}^3 (d\mathbf{x}_i + d\mathbf{u}_i)^2 \quad (6.2)$$

where $d\mathbf{u}_i = \mathbf{u}_i(\mathbf{r}_1) - \mathbf{u}_i(\mathbf{r}_2)$. We can now put, without loss of generality, $\mathbf{r}_2 = 0$ and $\mathbf{r}_1 = \mathbf{r}$. Straightforward manipulation of equation (6.2) in terms of \mathbf{r} , neglecting terms higher than first order in the strains, leads to:

$$d\mathbf{l}'^2 = d\mathbf{l}^2 + \sum_{i,k=1}^3 \left(\frac{d\mathbf{u}_i}{d\mathbf{x}_k} + \frac{d\mathbf{u}_k}{d\mathbf{x}_i} + \frac{d\mathbf{u}_j}{d\mathbf{x}_i} \frac{d\mathbf{u}_j}{d\mathbf{x}_k} \right) d\mathbf{x}_i d\mathbf{x}_k \cong d\mathbf{l}^2 + \sum_{i,k=1}^3 \left(\frac{d\mathbf{u}_i}{d\mathbf{x}_k} + \frac{d\mathbf{u}_k}{d\mathbf{x}_i} \right) d\mathbf{x}_i d\mathbf{x}_k \equiv d\mathbf{l}^2 + 2U_{ik} d\mathbf{x}_i d\mathbf{x}_k \quad (6.3)$$

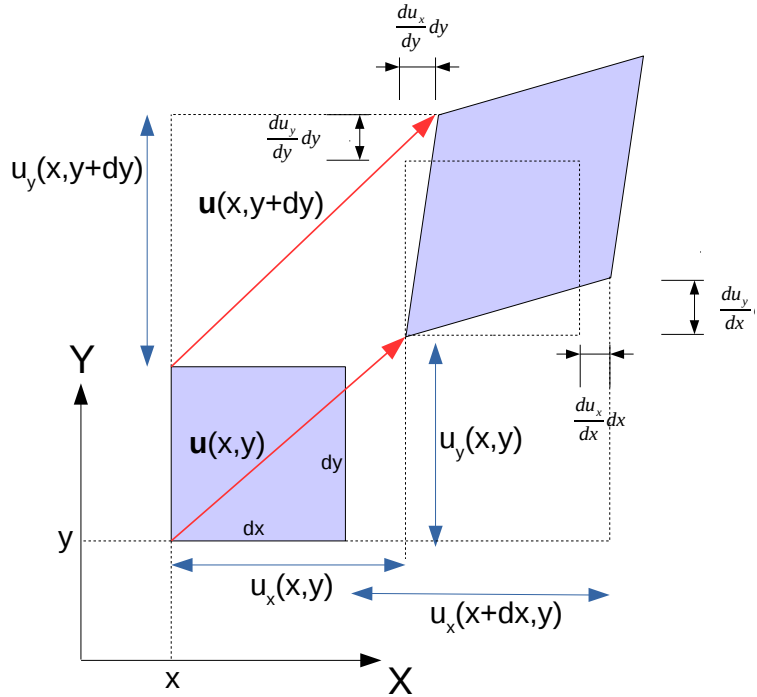


Figure 6.1: Graphical representation of the strain tensor components.

where the approximation is valid for small deformations, which is often the case. U_{ik} is a rank two tensor; it is named *strain tensor* and in general depends on the point of the sample; it is manifestly symmetric.

The fractional change of volume associated with a deformation can be evaluated considering an arbitrary volume dV (centred on a given point of the sample, say \mathbf{r}_0) and its expression dV' after the deformation. If we choose the principal axes of the strain tensor at \mathbf{r}_0 as reference system and call dx_1, dx_2, dx_3 the length elements along these directions, we have that $dx'_1 = (1 + U_{11})dx_1$ etc. Therefore we find that, at first order in the strain tensor components:

$$dV' = dV(1 + \text{Tr}(U)) \quad \text{Tr}(U) = \frac{V' - V}{V} \quad (6.4)$$

The trace of the strain tensor thus represents the local percentage of variation of volume during the deformation.

6.2 Stress tensor

We now define the stress tensor. The definition of stress is a generalization of the definition of pressure, i.e. force per unit area. Given a surface orthogonal to, say, the z direction, we can decompose the force (per unit area) acting on it in its three components along the axes (see Figure 6.2): we denote these components as Σ_{xz} , Σ_{yz} and Σ_{zz} . If we do the same with surfaces orthogonal to the x and y direction, we end up with the 3×3 *stress tensor*:

$$\Sigma = \begin{pmatrix} \Sigma_{xx} & \Sigma_{xy} & \Sigma_{xz} \\ \Sigma_{yx} & \Sigma_{yy} & \Sigma_{yz} \\ \Sigma_{zx} & \Sigma_{zy} & \Sigma_{zz} \end{pmatrix} \quad (6.5)$$

With the notation introduced, the first letter of the subscript is the direction of the force, while the second one is the direction of the normal to the plane on which the force is acting. The stress tensor is symmetric if we require that no torque is applied to an elementary cube of the system, so that there is no angular acceleration due to internal forces.

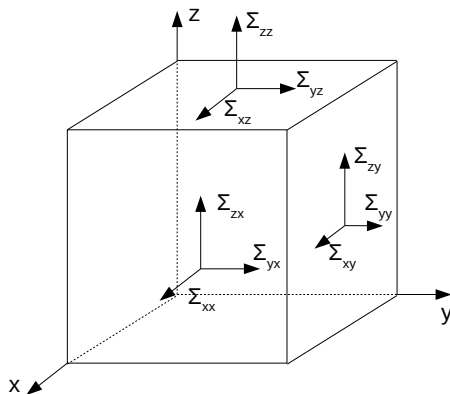


Figure 6.2: graphical representation of the stress components acting on the surfaces of an infinitesimal cube.

According to which components of the stress tensor Σ are non null, we can classify some useful types of stresses:

1. If we have that $\Sigma(\mathbf{r}_0) = \lambda I$ for a certain point \mathbf{r}_0 , we talk of *hydrostatic stress* at the point \mathbf{r}_0 .

2. If only two diagonal component, say $\Sigma_{xx}(\mathbf{r}_0), \Sigma_{yy}(\mathbf{r}_0)$ for simplicity, are the only ones different from zero at a certain point \mathbf{r}_0 and such that $\Sigma_{xx}(\mathbf{r}_0) = \Sigma_{yy}(\mathbf{r}_0)$, then we talk of in-plane (x, y) biaxial stress at the point \mathbf{r}_0 .
3. If only one diagonal component, say $\Sigma_{xx}(\mathbf{r}_0)$ for semplicity, is the only one different from zero at a certain point \mathbf{r}_0 , then we talk of *uniaxial stress* along the \hat{x} direction at the point \mathbf{r}_0 .

Since stress and strain tensors are related (as we will see in the following), it is usual to refer to these classifications as hydrostatic, biaxial and uniaxial *strain*. For instance, we talk of 1% hydrostatic strain value at the point \mathbf{r}_0 when the stress tensor is such that the corresponding hydrostatic strain value is of 1%; or we talk of 1% in plane (x, y) biaxial strain value at the point \mathbf{r}_0 when the stress tensor is such that we have $U_{xx}(\mathbf{r}_0) = U_{yy}(\mathbf{r}_0) = 1\%$ (the value of the other strain components depends on the system in consideration).

6.3 Stress-strain relation

The stress and strain tensors are useful in describing the response of a solid to an external load. The description of the state of deformation of the solid needs to invoke all the strain components; this task is usually performed through the elastic constants of the solid. These are represented by a tensor of rank 4, C_{ijkl} , where each index assumes three values, corresponding to x, y, z , called the *elastic stiffness* tensor. The generalized Hooke's law is expressed, in this notation, as:

$$\Sigma_{ij} = \sum_{k,l=1}^3 C_{ijkl} U_{kl} \quad (6.6)$$

Not all the values of the C_{ijkl} tensor are independent, because of symmetry of strain and stress tensors. In general, only 21 components of the C_{ijkl} tensor are independent.

A mostly used notation for the elastic stiffness tensor is the Voigt notation. We build a two-index symmetric 6x6 matrix, C_{ij} , containing all the 21 independent components of the C_{ijkl} tensor, and 6-dimensional vectors containing the strain and the stress tensors components with the following rule:

every couple of indexes of C_{ijkl} , Σ_{ij} and U_{ij} must be converted to one index only through the associations of equation (6.7).

$$1 \rightarrow xx \quad 2 \rightarrow yy \quad 3 \rightarrow zz \quad 4 \rightarrow yz \quad 5 \rightarrow xz \quad 6 \rightarrow xy \quad (6.7)$$

Using the above rule we can write:

$$\begin{aligned} \Sigma_1 &= C_{11}U_1 + C_{12}U_2 + C_{13}U_3 + C_{14}U_4 + C_{15}U_5 + C_{16}U_6 \\ \Sigma_2 &= C_{21}U_1 + C_{22}U_2 + C_{23}U_3 + C_{24}U_4 + C_{25}U_5 + C_{26}U_6 \\ \Sigma_3 &= C_{31}U_1 + C_{32}U_2 + C_{33}U_3 + C_{34}U_4 + C_{35}U_5 + C_{36}U_6 \\ \Sigma_4 &= C_{41}U_1 + C_{42}U_2 + C_{43}U_3 + C_{44}U_4 + C_{45}U_5 + C_{46}U_6 \\ \Sigma_5 &= C_{51}U_1 + C_{52}U_2 + C_{53}U_3 + C_{54}U_4 + C_{55}U_5 + C_{56}U_6 \\ \Sigma_6 &= C_{61}U_1 + C_{62}U_2 + C_{63}U_3 + C_{64}U_4 + C_{65}U_5 + C_{66}U_6 \end{aligned} \quad (6.8)$$

The set of equations (6.8) can be condensed in the following compact expression:

$$\Sigma = \mathbf{C}U \quad (6.9)$$

also expanded in the form (6.6). The stiffness constants have dimension of [Energy]/[Volume]. Conversely, the strain components linearly depend on the stress components as follows:

$$U = \Lambda\Sigma \quad U_{ij} = \sum_{k,l=1}^3 \Lambda_{ijkl}\Sigma_{kl} \quad (6.10)$$

where Λ is the elastic compliance matrix, inverse of the elastic stiffness matrix.

6.3.1 Application of elasticity theory to solids

We examine the example of an isotropic, elastic solid. First, we consider a normal stress Σ_{xx} which is applied in the x direction. The solid is deformed in the x direction, according to:

$$U_{xx} = \frac{1}{Y}\Sigma_{xx} \quad (6.11)$$

where Y is the Young's modulus (i.e. the response coefficient of the material in the direction parallel to the stress). The solid can also be strained along the y and z directions:

$$U_{yy} = U_{zz} = -\nu U_{xx} = -\nu \frac{\Sigma_{xx}}{Y} \quad (6.12)$$

where ν is called Poisson ratio. The Poisson's ratio is usually a positive quantity: when a material is pulled in one direction, its section perpendicular to the pulling direction becomes smaller. If three normal stresses $\Sigma_{xx}, \Sigma_{yy}, \Sigma_{zz}$ are applied to an orthogonal parallelepiped with faces normal to the x, y, z axes, its state of deformation will be:

$$\begin{aligned} U_{xx} &= \frac{1}{Y} [\Sigma_{xx} - \nu(\Sigma_{yy} + \Sigma_{zz})] \\ U_{yy} &= \frac{1}{Y} [\Sigma_{yy} - \nu(\Sigma_{xx} + \Sigma_{zz})] \\ U_{zz} &= \frac{1}{Y} [\Sigma_{zz} - \nu(\Sigma_{xx} + \Sigma_{yy})]. \end{aligned} \quad (6.13)$$

An analogous expression can be obtained for shear stresses. In fact, if a shear stress Σ_{xy} is applied to a solid, the corresponding shear strain is given by:

$$U_{xy} = \frac{1}{\mu} \Sigma_{xy} \quad (6.14)$$

where μ is the shear modulus.

Independent components of the elastic stiffness/compliance tensors for the germanium structure

In general, due to the symmetry of the stress and strain tensors the stiffness tensor C has 21 independent components. We want to study if it is possible to reduce the number of independent components of the elastic tensor in the case of the germanium diamond structure of Figure (1.1). In the case of cubic symmetry, our system is left invariant by the following symmetry operations:

$$\begin{aligned} x &\rightarrow -x, y \rightarrow y, z \rightarrow z \\ x &\rightarrow x, y \rightarrow -y, z \rightarrow z \\ x &\rightarrow x, y \rightarrow y, z \rightarrow -z \\ x &\rightarrow y, y \rightarrow -x, z \rightarrow z \\ x &\rightarrow x, y \rightarrow -z, z \rightarrow y \\ x &\rightarrow z, y \rightarrow y, z \rightarrow -x \end{aligned} \quad (6.15)$$

To derive the independent components of the elastic constant tensor it is useful to use the expression of the strain energy density [102]:

$$W = \sum_{i,j=1}^3 \frac{1}{2} \Sigma_{ij} U_{ij} = \sum_{i,j,l,k=1}^3 \frac{1}{2} C_{ijkl} U_{lk} U_{ij} \quad (6.16)$$

From the first three transformations of equation (6.15) and equation (6.16) it follows that any C_{ijkl} with an odd number of identical indexes is null. From the last three relations of equation (6.15) and equation (6.16) we obtain instead that:

$$C_{xxxx} = C_{yyyy} = C_{zzzz} \quad C_{xxyy} = C_{xxzz} = C_{yyzz} \quad C_{xzxz} = C_{yzyz} = C_{xyxy} \quad (6.17)$$

Thus we are left with 3 independent components of the stiffness tensor C , namely:

$$C_{xxxx} = C_{11} \quad C_{xxyy} = C_{12} \quad C_{yzyz} = C_{44}. \quad (6.18)$$

Following the same symmetry considerations, we have that also the elastic compliance Λ tensor has 3 independent components, namely:

$$\Lambda_{xxxx} = \Lambda_{11} \quad \Lambda_{xxyy} = \Lambda_{12} \quad \Lambda_{yzyz} = \Lambda_{44}. \quad (6.19)$$

As in our work we find convenient to describe the Ge crystal in the (X, Y, Z) reference system of Figure 1.3, we consider the elastic tensor referred to those axes, which we call C' . In this case, it can be shown by the transformation properties of the stiffness tensor [103, 104] that the independent components of C' are 6, namely:

$$\begin{aligned} C'_{XXXX} &= C'_{11} & C'_{ZZZZ} &= C'_{33} & C'_{XXZZ} &= C'_{13} \\ C'_{XXYY} &= C'_{12} & C'_{XYXY} &= C'_{66} & C'_{YZYZ} &= C'_{44} \end{aligned} \quad (6.20)$$

Analogous relations hold for Λ' :

$$\begin{aligned} \Lambda'_{XXXX} &= \Lambda'_{11} & \Lambda'_{ZZZZ} &= \Lambda'_{33} & \Lambda'_{XXZZ} &= \Lambda'_{13} \\ \Lambda'_{XXYY} &= \Lambda'_{12} & \Lambda'_{XYXY} &= \Lambda'_{66} & \Lambda'_{YZYZ} &= \Lambda'_{44} \end{aligned} \quad (6.21)$$

6.4 Ab-initio computation of the Ge bulk elastic compliance moduli tensor

As in our thesis we will work in the (X, Y, Z) reference frame, we start considering the Ge bulk crystal tetragonal simulation cell of Figure 1.3. Our aim is to calculate the elastic compliance constants Λ_{ijkl} , for the Ge bulk crystal, *referred to the (X, Y, Z) axes*. We therefore start looking for the minimum energy structural configuration of the simulation cell of Figure 1.3 and of the Ge atoms inside it, through the process of geometric optimization (as presented in chapter 3). Once found the equilibrium configuration, i.e. when no forces and no stresses act on our simulation cell, we apply a known percentage of strain (hydrostatic, biaxial or uniaxial in dependence of the working case) in the simulation cell. If we know the stresses arising in the system in consequence of the strain application, we can exploit the relation (6.10) in order to deduce the matrix elements of the elastic compliance tensor Λ' . Indeed, a workable expression for the calculation of stresses in a quantum system has been given in the paper by Nielsen and Martin ([105]). As it will be highlighted in chapter 7, the application of the numerical procedure described above needs a very high computational precision in order to give safe values for the components of the tensor Λ because of the sensitivity of the values of the stresses to the computed equilibrium configuration.

Chapter 7

Strained Ge bulk crystal

7.1 Introductory considerations

In chapter 4 we presented the ab-initio study of the structural and electronic properties of the Ge bulk crystal. We discussed the performances of various functional forms of the exchange-correlation potential, and of different basis sets to solve equation (2.8). Within the HSE06 hybrid functional formulation and localized Gaussians basis sets we were able to reproduce the experimental crystal lattice parameter and the shape of the electronic band structure of relaxed Ge bulk within a good precision. We then focused, in chapter 5, on the minimum energy structure and electronic states of the p(2x1)-reconstructed Ge (001) surface shown in Figure 1.8 (d), and we have demonstrated that it is possible to describe the semi-infinite crystal in terms of a slab of 12 atomic layers of Ge, properly Hydrogen-saturated on the bottom slab layer. In this chapter and in chapter 8 we report our ab-initio study of the effects of strain on Ge bulk crystal and on p(2x1) Ge (001) surface, respectively. As we shall discuss in the following sections, strain modifies both structural and electronic properties of the system under consideration; in particular the strain-induced shifts and the splitting of the energy levels of the conduction and valence bands are relevant even for small strain amount.

In the 40's Burenkov et al. [106] measured the elastic moduli costants of Ge bulk crystal using ultrasound spectroscopic techniques. The earliest theoretical milestone in the study of strain effects on

the electronic properties of semiconductors is represented by the work of Bardeen and Shockley in the 50's [107]. In the latter work it was firstly developed the deformation potential theory, i.e. a framework to calculate the electronic band structure modifications in consequence of strain application, by means of an effective interaction in the Hamiltonian of equation (2.8). The theory was later generalized by Herring and Vogt and by Picus and Bir [108]. In 60's Picus and Bir studied various semiconductors via group theory and expanded the deformation potential theory including the spin-orbit effect. One of the most important application of deformation potential theory with spin-orbit interaction, as developed by Picus and Bir, is due to Pollack and Cardona in 1968[109]. It took more than two decades from the work of the Bardeen and Shockley to perform a measurement of deformation potentials for Ge crystal (1975 Wiley [110]).

Ab-initio calculations, as theoretical and numerical methods for the evaluation of total energies, are most useful to study the strain effects on Ge bulk structural and electronic properties. As examples of recent studies of the electronic properties of Ge crystal under strain application, we mention the works of El Kurdi et al. [23, 24], where a $\mathbf{k} \cdot \mathbf{p}$ method is used, Gupta et al. [25], who implemented an empirical pseudopotential method (EPM) for the calculations, and Sakata et al. [83], where different DFT exchange-correlation functional performances are compared.

7.2 Tetragonal cell choice for surface description

As explained in the introduction to this chapter, the final aim of this thesis is the theoretical and numerical study of the effects of strain applied on the p(2x1) Ge (001) surface and in particular of the behaviour of surface states of the strained surface. For this reason it is convenient to study first the effects of strain on the Ge bulk crystal of Figure 1.3. In this section we calculate the components of the elastic compliance tensor Λ_{ij} , defined in equation (6.10), referred to (X, Y, Z) axes of Figure 1.3, and we then study the effects of the application of (i) hydrostatic stress, (ii) in-plane (X, Y) biaxial stress and (iii) uniaxial stress along Y direction (i.e. the direction of the Ge (001) surface dimers) on the Ge

bulk crystal.

We refer to equation (6.10) for the definition of the elastic compliance tensor Λ_{ij} and to chapter 6 for the considerations on the symmetry of this tensor and for the definitions of the various types of strains.

7.2.1 Elastic compliance tensor calculation

In this section we perform the ab-initio computation of the components of the elastic compliance tensor Λ_{ij} , which are essential for the determination of interlayer distances in the strained Ge slab geometry.

To compute the Λ matrix referred to (X, Y, Z) axes we consider the starting simulation cell represented in Figure 1.3, containing 4 Ge atoms. As explained in section 6.4, the first step is to look for the structural configuration which minimizes the unstrained Ge crystal ground state energy, where, consequently, no stresses act on the system. This is performed by means of the QUANTUM ESPRESSO code. Before presenting the computational results, we highlight the importance of obtaining a very precise value of the minimum energy configuration of the geometrical structure. In this section we improve the computational precision reached in chapter 4 to calculate the relaxed minimum energy geometrical configuration. We thus use a cutoff of 100 Ry for the plane-wave basis set, and the PBEsol exchange correlation functional with norm conserving generated pseudopotentials for Ge atoms. We have left the cell edges free to relax until a minimum energy configuration was reached, with a convergence on the forces on each atom of $10^{-6} \text{Ry}/\text{Bohr}$, and a convergence on the total energy per simulation cell of 10^{-7}eV . The relaxed structure is presented in Figure 7.1.

We can see that the conventional cell of Figure 7.1 slightly differs from the one of Figure 1.3 because it has different proportions between p and q . In fact, in Figure 1.3 we have $q = a = p\sqrt{2} = 5.758 \text{\AA}$, whereas in Figure 7.1 $p'\sqrt{2} = p = 4.071 \text{\AA}$ and $q' = 5.752 \text{\AA}$. Since we expect from symmetry consideration that the relaxed (unstrained) conventional cell should have maintained the proportions between p and q , we will consider this discrepancy between q and q' , which is of the order of 10^{-3} , as the computational error on the relaxed structure. We anticipate that, in order to consider the consequences of this error, we performed the computation of elastic compliance matrix and band structure of Ge crystal starting

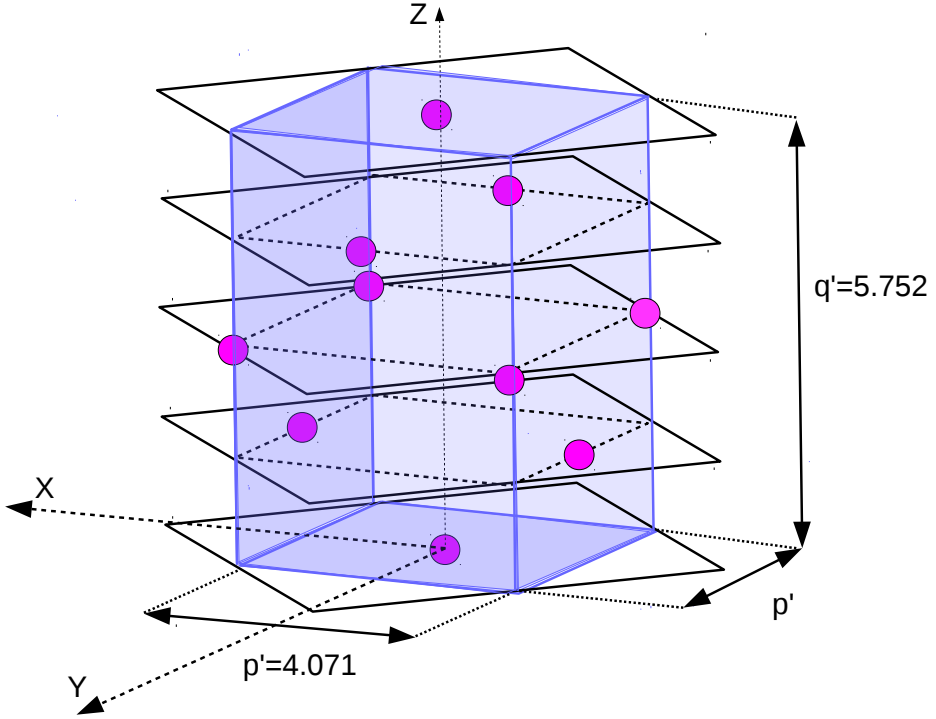


Figure 7.1: Minimum energy configuration of the Ge tetragonal conventional cell. After the energy minimization procedure, the conventional cell (shaded in blue) remains tetragonal with dimensions $p' = p = 4.071\text{\AA}$ and $q' = 5.752\text{\AA}$. Notice that for the cell in Figure 1.3 we had $q = a = p\sqrt{2} = 5.758\text{\AA}$.

both from the geometrical structure of Figure 7.1 with the computed values of p' and q' and from the geometrical structure of Figure 1.3 with the value $q = p\sqrt{2} = 5.758\text{\AA}$. The elastic compliance matrix in both cases satisfies equation (6.10) with differences up to 10^{-4} strain values and the eigenvalues of the band structures differ in the two cases less than 10^{-2}eV . We can thus proceed using as relaxed Ge bulk structure the experimental geometrical structure of Figure 1.3 with $q = p\sqrt{2}$, $p = 4.071\text{\AA}$ and $q = 5.758\text{\AA}$.

Once obtained the relaxed geometrical structure of the unstrained Ge bulk, we can proceed applying deformations and, as explained in chapter 6, calculating stresses arising in the system. We preliminary consider stresses acting on the simulation cell and calculate derivative of the electronic ground state energy with respect to deformation, and we then exploit the relation (6.10) between stresses and strains to obtain the Λ_{ij} matrix, referred to the (X, Y, Z) axes. We have obtained for the Λ_{ij} matrix the

following values, in units of Bohr^3/Ry :

$$\Lambda' = \Lambda_{XYZ} = \begin{pmatrix} 110.07 & 14.37 & -53.55 & 0 & 0 & 0 \\ 14.37 & 110.07 & -53.55 & 0 & 0 & 0 \\ -53.55 & -53.55 & 192.39 & 0 & 0 & 0 \\ 0 & 0 & 0 & 98.435 & 0 & 0 \\ 0 & 0 & 0 & 0 & 98.435 & 0 \\ 0 & 0 & 0 & 0 & 0 & 220.994 \end{pmatrix} \quad (7.1)$$

Comparing (7.1) with conditions of equation (6.21), we see that the computation correctly gives $\Lambda'_{11} = \Lambda'_{22}$, $\Lambda'_{12} = \Lambda'_{21}$, $\Lambda'_{13} = \Lambda'_{23} = \Lambda'_{31} = \Lambda'_{32}$. To directly compare with experimental data, we have to refer the Λ'_{ij} matrix of equation (7.1) to the crystallographic axes (x, y, z) , which are the axes used in the experiments. To rotate the components of the elastic compliance matrix we used the formula given in the work by Wortman et al. [104]. Expressing the elastic compliance tensor in the (x, y, z) reference frame, in $10^{-12}\text{cm}^2/\text{dyne}$ for comparison with experimental values, we have:

$$\Lambda_{xyz} = \begin{pmatrix} 1.17 & -0.33 & -0.36 & 0 & 0 & 0 \\ -0.33 & 1.17 & -0.36 & 0 & 0 & 0 \\ -0.36 & -0.36 & 1.30 & 0 & 0 & 0 \\ 0 & 0 & 0 & 1.33 & 0 & 0 \\ 0 & 0 & 0 & 0 & 1.33 & 0 \\ 0 & 0 & 0 & 0 & 0 & 1.30 \end{pmatrix} \quad (7.2)$$

In the same units the experimental value of the tensor is, at 300K [104],:

$$\Lambda_{exp} = \begin{pmatrix} 0.97 & -0.26 & -0.26 & 0 & 0 & 0 \\ -0.26 & 0.97 & -0.26 & 0 & 0 & 0 \\ -0.26 & -0.26 & 0.97 & 0 & 0 & 0 \\ 0 & 0 & 0 & 1.49 & 0 & 0 \\ 0 & 0 & 0 & 0 & 1.49 & 0 \\ 0 & 0 & 0 & 0 & 0 & 1.49 \end{pmatrix} \quad (7.3)$$

It is possible also to compare the elastic constant tensor C with experimental results, remembering that:

$$\mathbf{C} = \mathbf{\Lambda}^{-1} \quad (7.4)$$

Expressing the elastic constant tensor in units 10^{12}dyne/cm^2 , for comparison with experimental values, we have:

$$C_{xyz} = \begin{pmatrix} 1.11 & 0.45 & 0.43 & 0 & 0 & 0 \\ 0.45 & 1.11 & 0.43 & 0 & 0 & 0 \\ 0.43 & 0.43 & 1.01 & 0 & 0 & 0 \\ 0 & 0 & 0 & 0.75 & 0 & 0 \\ 0 & 0 & 0 & 0 & 0.75 & 0 \\ 0 & 0 & 0 & 0 & 0 & 0.75 \end{pmatrix} \quad (7.5)$$

The experimental value of the tensor is, at 300K [106],:

$$C_{exp} = \begin{pmatrix} 1.24 & 0.41 & 0.41 & 0 & 0 & 0 \\ 0.41 & 1.24 & 0.41 & 0 & 0 & 0 \\ 0.41 & 0.41 & 1.24 & 0 & 0 & 0 \\ 0 & 0 & 0 & 0.68 & 0 & 0 \\ 0 & 0 & 0 & 0 & 0.68 & 0 \\ 0 & 0 & 0 & 0 & 0 & 0.68 \end{pmatrix} \quad (7.6)$$

Looking at the values in the expression (7.5) we note that C_{12} is not exactly equal to C_{13} , as it would be required by the cubic symmetry of the crystal in the (x, y, z) reference system. Anyway, we see that $\frac{C_{12}-C_{13}}{C_{13}} = 0.02$. The same reasoning holds for C_{44} and C_{66} , with $\frac{C_{44}-C_{66}}{C_{66}} = 0.03$. We think that these discrepancies are within the computational errors and can be disregarded. The comparison with the experimental data at room temperature is satisfactory even if it shows that the value of C_{11} is underestimated, in accordance with the general output of PBEsol functional for the evaluation of elastic tensor constants in semiconductors [82].

7.2.2 Hydrostatic strain on bulk Ge

We now study the effects of hydrostatic strain (defined in chapter 6) on electronic properties of the Ge bulk crystal. We perform electronic band calculation starting from the conventional simulation cell of Figure 1.1, as obtained changing the cell parameter value, under hydrostatic strains of -3% , -2% , -1% , 0% , 1% , 2% , 3% . The calculations have been performed by means of the CRYSTAL14 code using the HSE06 exchange-correlation functional and the same basis set which was used in chapter 4 for the reproduction of relaxed Ge bulk properties. To be coherent with the choice of the exchange-correlation functional adopted, the starting simulation cell is the one obtained with the HSE06 exchange-correlation functional, with lattice parameter $a = 5.642\text{\AA}$, as shown in chapter 4.

We report in Figure 7.2 and Table 7.1 the behaviour of the indirect gap $E_{L-\Gamma}$ and the direct gap $E_{\Gamma-\Gamma}$ as function of the strain conditions. As mentioned in the introduction to this chapter, we can see from Figure 7.2 and Table 7.1 that even a small percentage of strain changes drastically the value of the various gaps. For instance, we can see that the fundamental gap converts from indirect ($L - \Gamma$) to direct

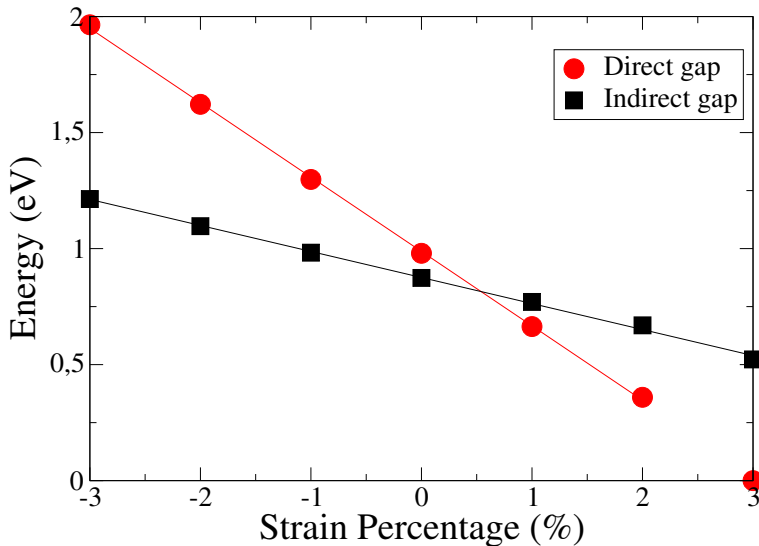


Figure 7.2: Direct (red circles) and indirect (black squares) gap energies (eV) in function of the applied hydrostatic strain percentage to Ge bulk, obtained using CRYSTAL14 and HSE06 as exchange-correlation functional. The metallic behaviour for 3% tensile strain value should be further investigated because the performance of hybrid functionals on such cases has not been tested in this work.

$(\Gamma - \Gamma)$ between 0.5% and 1% tensile strain percentage. As an example of Ge bulk electronic band structure under hydrostatic strain, we report in Figure 7.3 the results relative to 2% strain. Differently from Figure 4.4, in Figure 7.3 the fundamental gap is direct and positioned at Γ , in agreement with Figure 7.2. We can also notice that the bands degeneracy at high symmetry points is the same as in Figure 4.4. This is consequence of the isotropic action of the hydrostatic strain. In fact, the structural effect of hydrostatic strain is to change the value of the lattice parameter only, without affecting the symmetries of the system. Therefore, the classification of band degeneracies is the same as for relaxed unstrained Ge bulk.

Strain %	Indirect gap	Direct gap
-3%	1.193	1.943
-2%	1.076	1.599
-1%	0.961	1.275
0%	0.852	0.957
1%	0.749	0.641
2%	0.648	0.336
3%	0.501	0.000

Table 7.1: Indirect and direct gaps behaviour fg Ge bulk under hydrostatic strain.

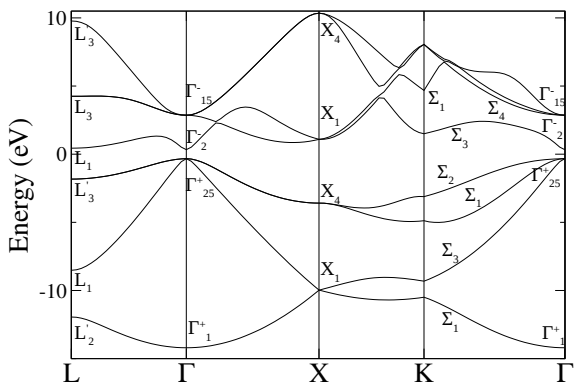


Figure 7.3: Ge bulk electronic band structure corresponding to an application of 2% hydrostatic tensile strain, obtained with HSE06 using a 6x6x6 Monkhorst-Pack grid.

We finally mention that from Figure 7.2 we have hints of metallic behaviour of Ge bulk for 3% hydrostatic tensile strain. This result is consistent with the work of Yang et al.[81].

7.2.3 Biaxial strain on Ge bulk

We now deal with in-plane (X, Y) biaxial strain on Ge, considering the simulation cell reported in Figure 7.4.

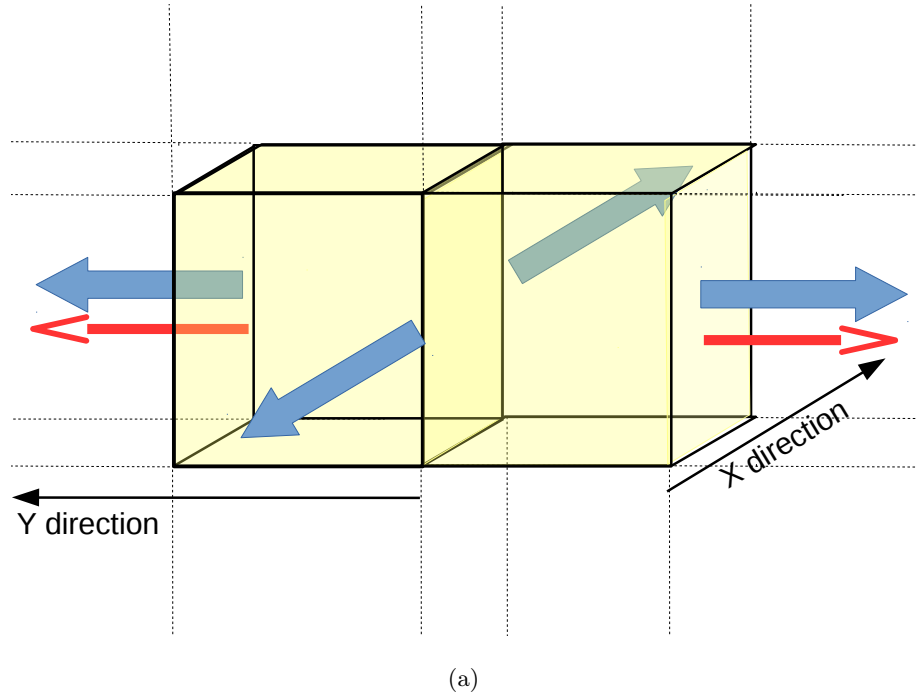


Figure 7.4: Ge bulk simulation cell on which biaxial tensile (blue arrows) and uniaxial tensile (red arrows) strains are applied. The arrows are directed inward in the case of compressive strains.

We consider in-plane (X, Y) biaxial strains of $-2\%, -1.5\%, -1\%, 0.5\%, 0\%, 0.5\%, 1\%, 1.5\%, 2\%$. Calculations are performed with CRYSTAL14 code using HSE06 as exchange-correlation functional and the same pseudopotential-basis set which was used in chapter 4. We apply strains to the simulation cell with relaxed lattice parameter $a = 5.642\text{\AA}$. As example, for value of 2% tensile (X, Y) biaxial strain, shown in Figure 7.4, we obtain the band structure of Figure 7.5. It is useful to report the behaviour of Ge bulk indirect and direct gap under strain application. We present in Figure 7.6 and in Table 7.2 the results of our calculations for the behaviour of direct and indirect gaps of bulk Ge under in plane (X, Y)

biaxial strain. The crossing between direct and indirect gap is around 1.7% tensile biaxial strain.

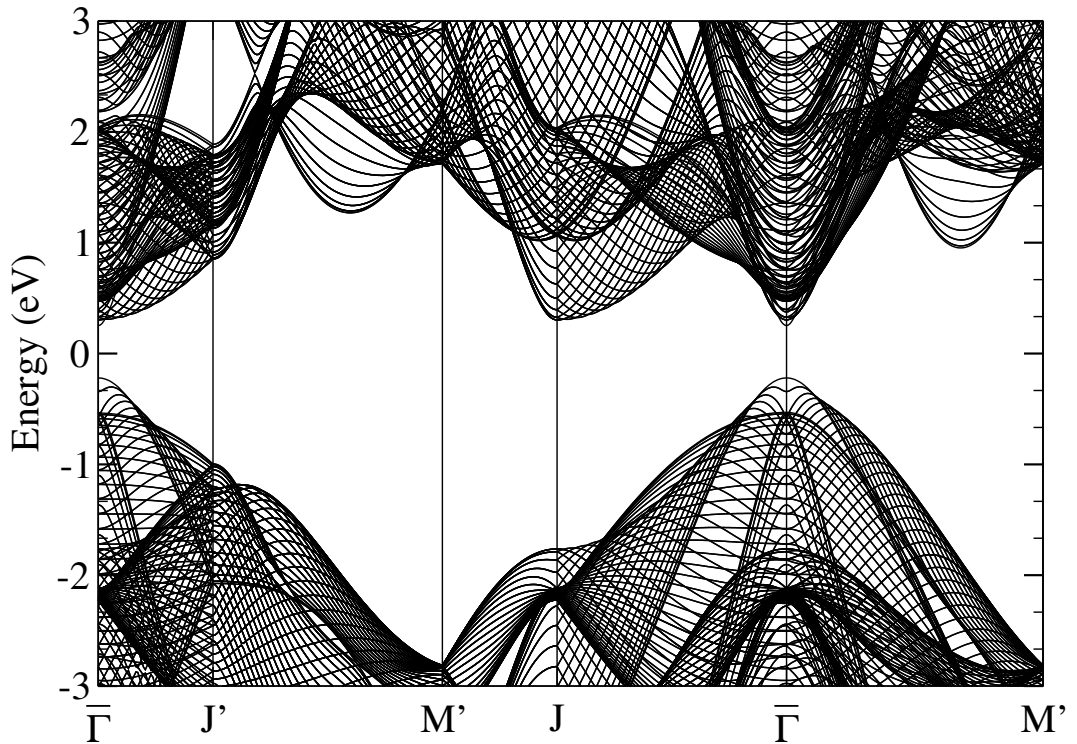


Figure 7.5: Electronic bulk bands of bulk Ge, under 2% tensile biaxial strain, projected on the (2x1) Ge (001) strained surface Brillouin zone. The energy bands are obtained with HSE06 exchange-correlation functional using a 6x6x6 Monkhorst-Pack grid. The fundamental gap between top valence and bottom conduction bands is at $\bar{\Gamma}$ point.

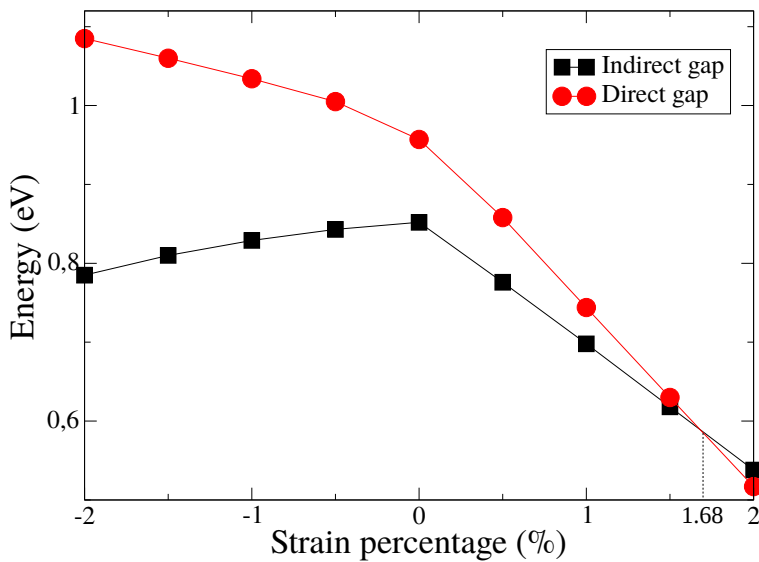


Figure 7.6: Indirect and direct band gap energies for biaxially strained bulk Ge.

Strain %	Fundamental gap	Optical (direct) gap
-2%	0.785	1.085
-1.5%	0.810	1.060
-1%	0.829	1.034
-0.5%	0.843	1.005
0%	0.852	0.957
0.5%	0.776	0.858
1%	0.698	0.744
1.5%	0.618	0.630
2%	0.538	0.517

Table 7.2: Fundamental and optical gaps behaviour of the bulk Ge under in-plane (X, Y) biaxial strain application. The direct gap becomes the fundamental energy gap for tensile biaxial strains larger than 1.7%.

To compare with other works we remember that a biaxial strain of a certain percentage along (X, Y) direction corresponds to a biaxial strain along (x, y) direction with the same strain percentage. For comparison, in the work of El Kurdi et al. based on a 30 $\mathbf{k} \cdot \mathbf{p}$ -formalism [23] the crossing is found around 1.9% of in plane (x, y) tensile biaxial strain.

7.2.4 Uniaxial In-Plane Strain on Ge bulk

We now deal with uniaxial strain along Y direction (see Figure 7.4). As it was done for the study of in plane (X, Y) biaxial strain, we consider the simulation cell of Figure 7.4. We apply uniaxial strains, along Y direction, with percent values of $-2\%, -1.5\%, -1\%, 0.5\%, 0\%, 0.5\%, 1\%, 1.5\%, 2\%$. We choose the Y axis as the direction of uniaxial strain application because it corresponds to the surface dimer direction on the p(2x1)-(001) Ge surface. Calculations are performed by means of the CRYSTAL14

code using HSE06 exchange-correlation functional and the same pseudopotential-basis set which was used in chapter 4. We project the Ge bulk bands of the uniaxially strained Ge onto the first Brillouin zone of the equally strained p(2x1) surface and obtain, in the case of 1% tensile uniaxial strain, the band structure of Figure 7.7. We can see that the bottom of the conduction bands for 1% tensile uniaxial strain along Y direction occurs at the J point, almost degenerate with the $\bar{\Gamma}$ energy.

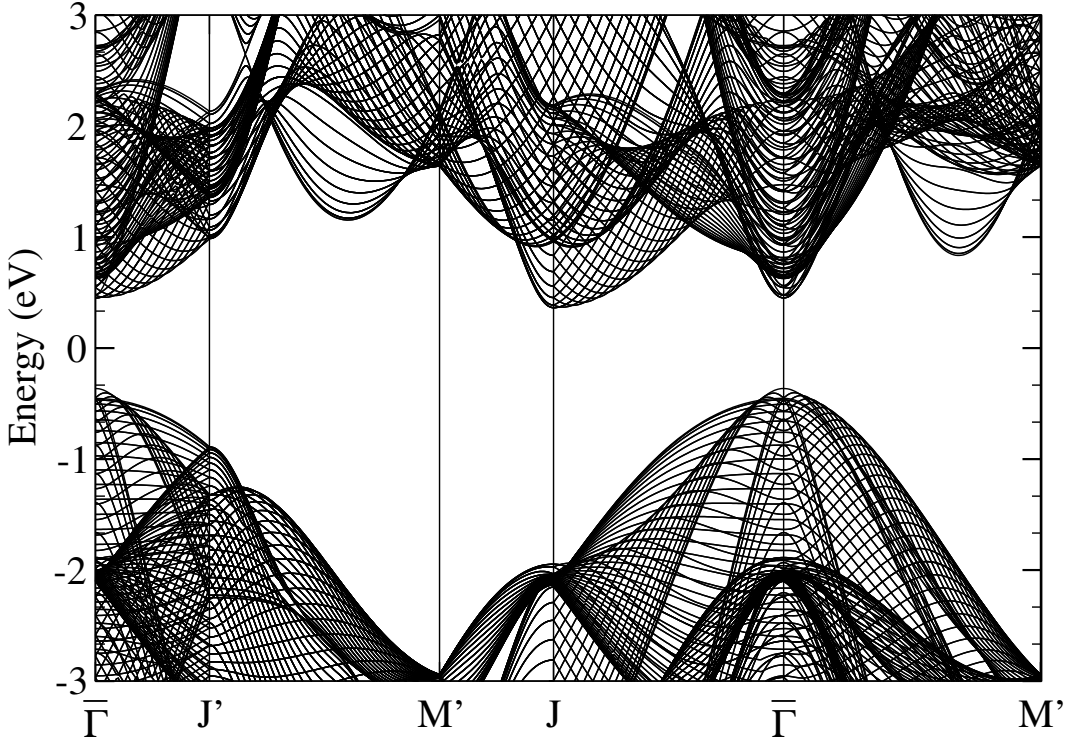


Figure 7.7: Electronic bulk bands of bulk Ge, under 1% uniaxial strain along Y direction, projected on the (2x1) Ge (001) strained surface Brillouin zone. The energy bands are obtained with HSE06 exchange-correlation functional using a 6x6x6 Monkhorst-Pack grid.

We present in Figure 7.6 and in Table 7.2 the results of our calculations for the behaviour of direct and indirect gaps in the case of uniaxial strained Ge along the Y direction. It is to note that in Figure 7.8 no crossing between direct and indirect gap appears in the studied range of strains, in contrast with the results of hydrostatic and biaxial strain. Indeed, this result is not surprising because a certain percentage of hydrostatic strain induces a volume change larger than the change obtained for the same percentage of biaxial strain, which in turn induces a volume change larger than for the same percentage

of uniaxial strain; since the band gaps behaviour highly depends on the total volume change, we should need an higher uniaxial strain to realize possible crossing, if it is present.

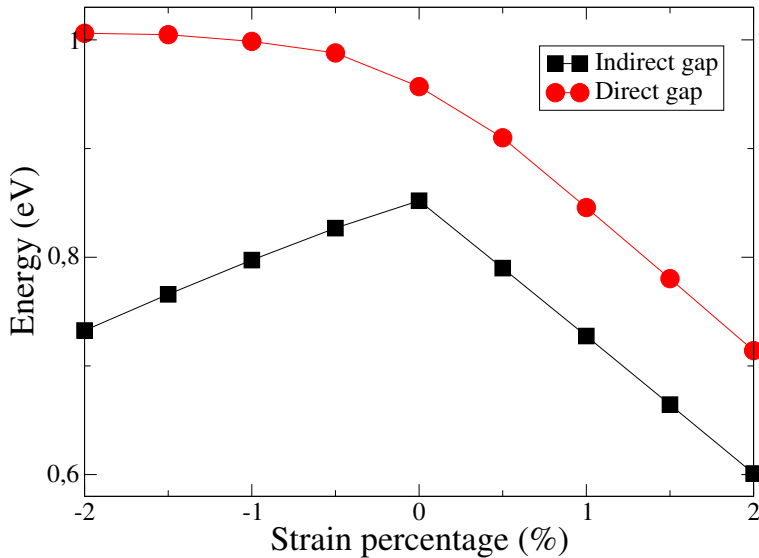


Figure 7.8: Indirect and direct band gap energies in function of the uniaxial strain percentage along the Y direction.

Strain %	Fundamental gap	Optical (direct)gap
-2%	0.7326	1.0061
-1.5%	0.7659	1.0048
-1%	0.7974	0.9986
-0.5%	0.8268	0.9880
0%	0.852	0.957
0.5%	0.7900	0.9099
1%	0.7275	0.8457
1.5%	0.6644	0.7803
2%	0.6010	0.7141

Table 7.3: Fundamental and optical gaps behaviour under uniaxial strain application along the Y direction.

Chapter 8

Strained Ge-(001) surface

8.1 Introductory considerations

We present in this chapter our ab-initio calculations on the structural and the electronic properties of the p(2x1) Ge (001) surface under in plane (X, Y) biaxial strain and uniaxial strain along the Y direction. To our knowledge no studies of this system have been performed in the literature up to now, either experimentally or theoretically; only recently a similar approach for silicon surface states has been presented in the work of Miao Zhou et al. [29]. The importance of surface band engineering by strain in the p(2x1) Ge (001) surface is of central interest in many fields such as electronic and photonics, where Ge is an actual important material. We show in Figure 8.1 the simulation cell that will be used in the following of this chapter.

8.2 In plane (X, Y) biaxial strained p(2x1) Ge (001) surface

In chapter 5 we discussed how the displacements of the Ge (001) surface atomic positions from the ideal configuration of Figure 1.3 decay within the first 5 surface layers. In fact, from Figure 5.5 we can see that below the fifth Ge layer from the surface the geometry is bulk-like and practically the same of Figure 1.3. Moreover, as discussed in chapter 5, the study of the first 5 layers alone was not sufficient to

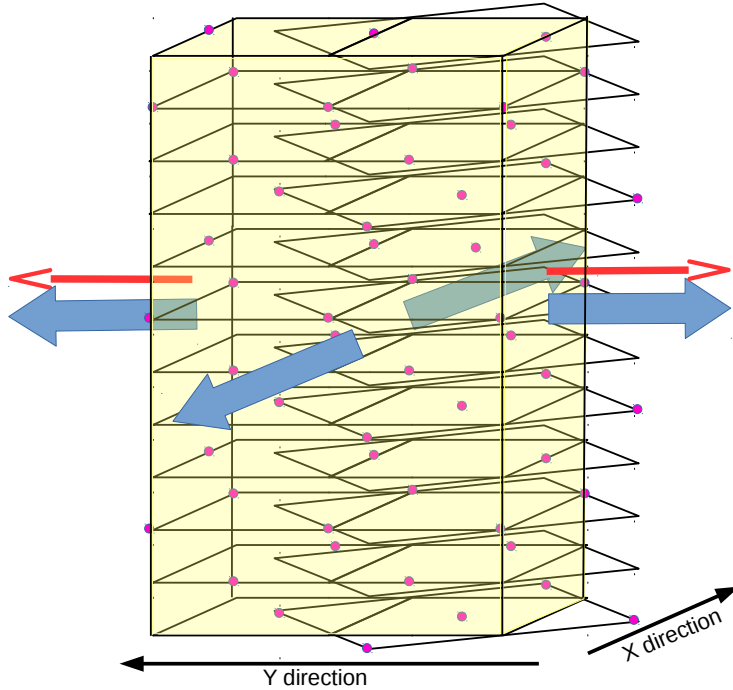


Figure 8.1: 12 layer (2x1) Ge (001) surface simulation cell. Schematic action of tensile in plane (X, Y) biaxial strain (blue arrows) and tensile uniaxial strain along Y direction (red arrows) is represented. The arrows are directed inward in the case of compressive strains.

reproduce the p(2x1) Ge surface electronic properties with high precision; we thus had to increment, in our numerical simulations, the number of Ge layers up to 12. Putting these considerations together, we conclude that the study of the p(2x1) Ge (001) surface needs the numerical simulation of a 12 layers Ge slab, but at the same time we can freeze the degrees of freedom of the Ge bulk-like atoms belonging to the layers below the first five, fixing their atomic positions to the bulk-like configuration of Figure 1.3. We will consider this reduction of degrees of freedom, which speeds up our calculations and efficiently simulate the effect of the ideal bulk underlying the Ge (001) surface, also as working procedure in the case of strain application.

We notice that, in the last few years, Ge nanomembranes have received steadily growing interests because they are promising tools to develop new electronic and photonic materials, and can be fabricated with precise orientation and sizes. In fact, for low-dimensional as well as for three-dimensional crystalline

materials a rich family of properties and functionalities can be tuned by strain-engineering, i.e., varying structural parameters, with the practical advantages following from the reduction of dimensionality. Significative strain values have been recently experimentally obtained on these germanium thin films by means of (mainly) mechanical deformation, epitaxial growth or stressor layers; some of these techniques are represented in Figure 8.2. The (unstrained and unreconstructed) geometrical configuration of these Ge thin films can be schematically represented as in Figure 8.1; this novel experimental interest in the behaviour of Ge nanomembranes under deformation closely connects to the concerns of this chapter.

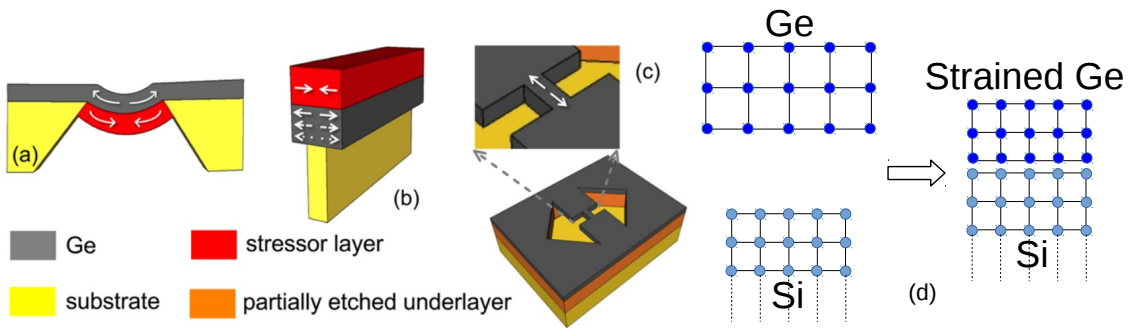


Figure 8.2: Schematic illustrations of the use of stressor layers to introduce tensile strain in Ge. (a) Cross-sectional image of the geometry used to obtain nominally biaxial tensile strain in an edge-clamped suspended Ge film. (b) Three-dimensional view of the uniaxially strained Ge photonic wires. (c) Uniaxially strained Ge microbridge geometry. In all figures, the arrows pointing outward (inward) indicate tensile (compressive) strain [1]. The solid, dashed, and dotted arrows in (b) indicate regions of progressively weaker tensile strain. Schematic representation of the epitaxial deposition process of Ge atoms (blue dots) on a Si substrate (light blue dots) used to obtain biaxial compressive strain on the Ge crystal due to lattice mismatch. To obtain tensile strain, a substrate of Sn is often used.

We start from the simulation cell of Figure 8.1, with the Ge atoms inside the cell arranged in the relaxed configuration specified in Figure 5.5. If we consider a certain percentage of in plane (X, Y) biaxial strain on the simulation cell of Figure 8.1, we have a consequent modification of the cell edges and of layer interspacing along the Z direction (as explained in chapter 6). If the strain percentage is small enough to consider the linear strain regime, the modification of the structure

below the fifth Ge layer from the surface can be obtained from the computed compliance tensor of equation (7.1). The Ge atomic positions of the first 5 layers below the surface are instead considered free to relax under each value of strain application. We now apply in-plane (X, Y) biaxial strain of $-2\%, -1.5\%, -1\%, 0.5\%, 0\%, 0.5\%, 1\%, 1.5\%, 2\%$ on the simulation cell of Figure 8.1 and evaluate geometrical structure and electronic bands by means of the QUANTUM ESPRESSO with PBESol as exchange-correlation functional. Notice that the elastic compliance constant of equation (7.1) was obtained with QUANTUM ESPRESSO with PBESol so that the modifications of the Ge atomic positions of the first 5 layers and of the layers below are considered coherently. Since we do not know the intensity of the relaxation process of the first 5 layers, we consider convenient to start the relaxation process from a configuration where all the Ge atomic position are calculated according to the elasticity theory reported in chapters 6 and 7. We use a cutoff of 100 Ry for the plane wave basis-set and a Monkhorst-Pack grid of dimensions $12 \times 6 \times 1$. The dimension of the Monkhorst-Pack grid is chosen in the form $i \times \frac{1}{2} \times 1$ along the (K_X, K_Y, K_Z) axes, where i is an integer number, because the Brillouin zone of the surface cell of the p(2x1) pattern is twice longer in the K_X direction than in the K_Y direction, as shown in Figure 1.9. We stop the geometric optimization process when we find the minimum energy configuration with a convergence on the forces on each atom of the order of $10^{-5} \text{Ry}/\text{Bohr}$ and a convergence on the total energy per cell of 10^{-6}eV . We show the results of the geometrical optimization process for -1% and 1% in plane (X, Y) biaxial strain values in Figure 8.3 (a) and (b), respectively.

Similarly as we discussed in chapter 5, also under strain the Projected-Density-Of-States (PDOS) of the top valence band and of the bottom conduction band of p(2x1) Ge (001) surface, show that these states are spatially localized on the Ge dimer. Consequently, it can be useful to display the behaviour of dimer length and dimer bond angle under in plane (X, Y) biaxial strain. The results are shown in Figure 8.4 (a) and (b), respectively. We notice from Figure 8.4 that the dimer length and the bond angle seem to be unaffected by the strain of the simulation cell. We checked that the results of Figure 8.4 (a) and (b) are not affected by the computational precision of the elastic compliance tensor of equation (7.1), repeating the geometric optimizations using the upper and lower limits of our precision

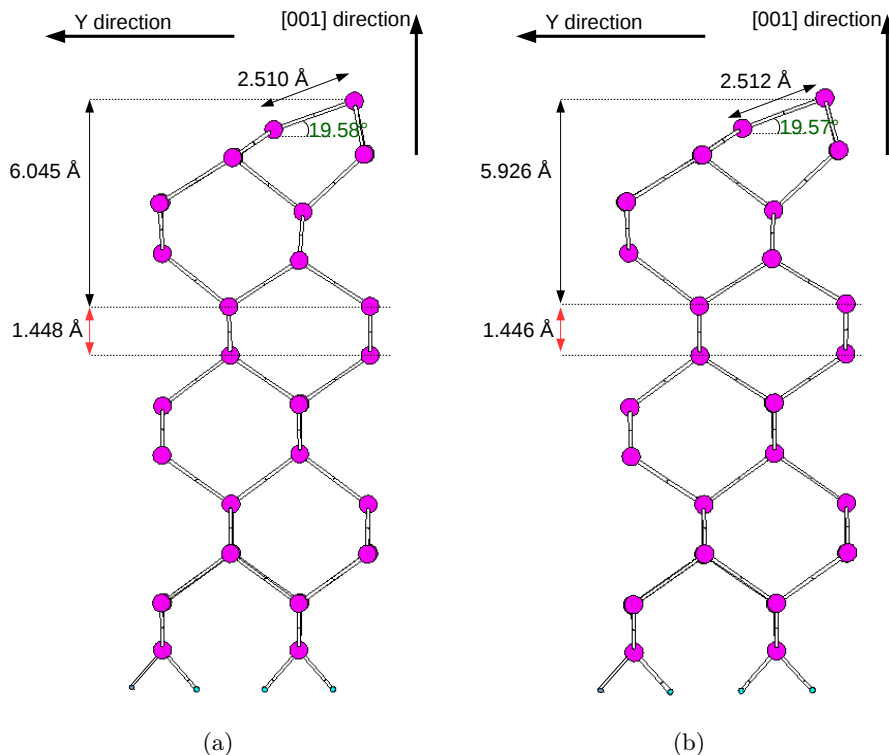


Figure 8.3: Final geometry after the relaxation process of the Ge atomic positions inside the simulation cell of Figure 8.1, under in plane (X, Y) biaxial strain of (a) -1% (compressive) and (b) 1% (tensile). The interspacing between fifth and sixth layers along [001] direction and total width of the first 5 layers are shown.

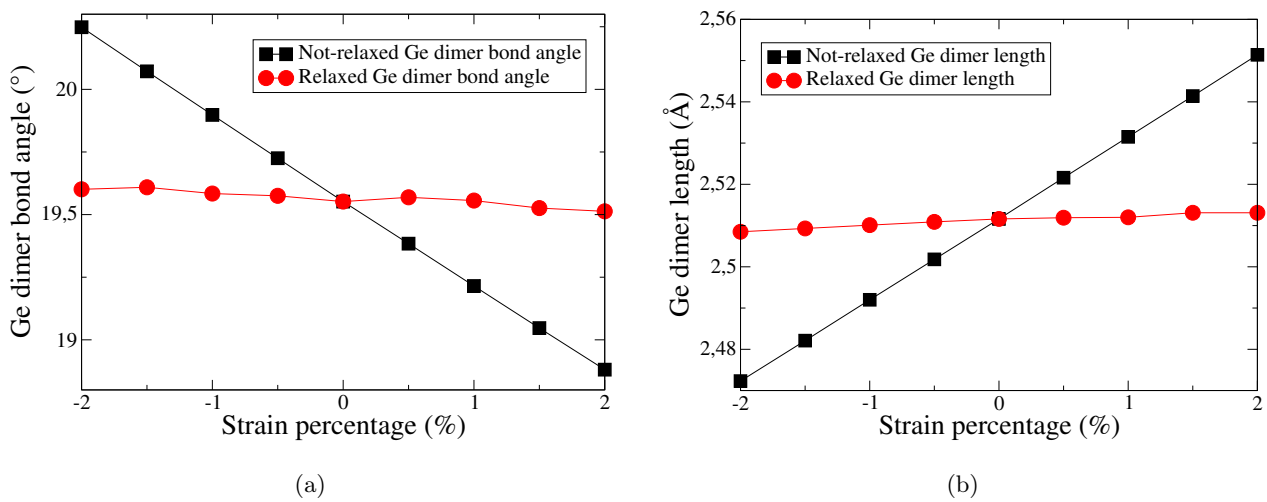


Figure 8.4: (a) Asymmetric dimer length and (b) bond angle behaviour, belonging to the p(2x1) Ge (001) surface under in plane (X, Y) biaxial strain before (black symbols) and after (red symbols) relaxation of Ge atomic positions.

(estimated to be of 10^{-4} strain value) to compute the fixed positions of the Ge atoms from the 6th to the 12th layer, and finding no relevant discrepancies. We then investigated the behaviour of the mean interspacing along the [001] direction between the fifth and sixth layers and of the total width of the first 5 layers along the Z direction, as indicated in Figure 8.3, under in plane (X, Y) biaxial strain. The results are shown in Figure 8.5 (a) and (b). We can see from Figure 8.5 (a) that for negative

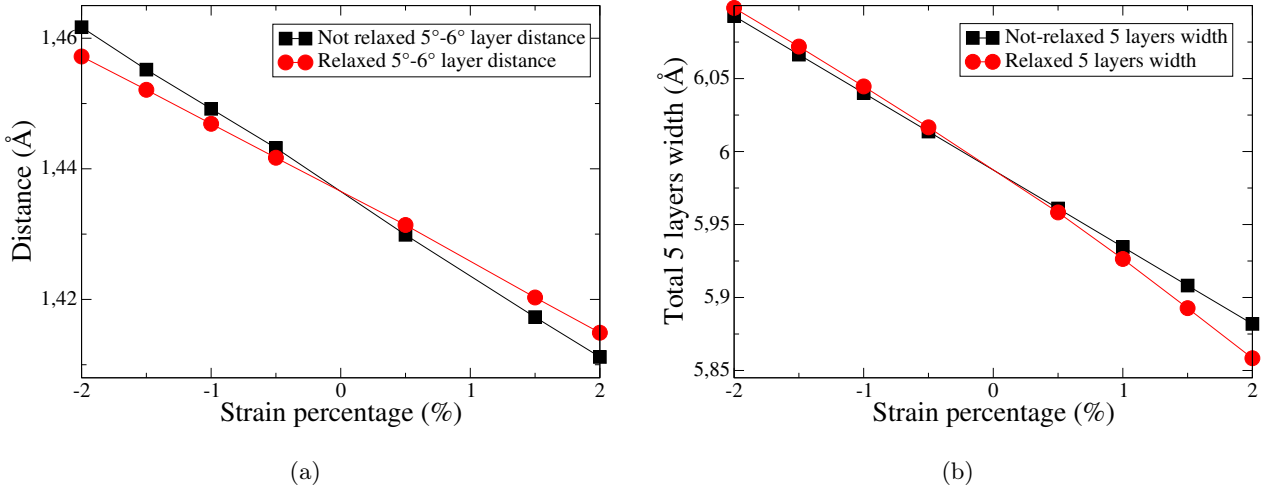


Figure 8.5: In plane (X, Y) biaxial strain effects on (a) the interspacing between the fifth and sixth layers and on (b) the total width of the first 5 layers of the simulation cell.

(compressive) values of in plane (X, Y) biaxial tensile strain the distance between the fifth and sixth layers, from the initial to the final configuration of the atomic relaxation process, is reduced whereas it increases for positive (dilatation) values of the strain. To be sure that this effect is not ascribable to the working procedure of relaxing the first five layers only, we repeated again the geometric relaxation considering the position of the Ge atoms of the sixth layer free to move, obtaining the same result. On the contrary, we can see from Figure 8.5 (b) that, for negative values of in plane (X, Y) biaxial tensile strain, the total width of the first five layers of the Ge (001) surface along the Z direction, from the initial to the final configuration of the atomic relaxation process, is increased whereas it decreases for positive values of the strain.

Once obtained the various relaxed geometries of the strained p(2x1) Ge (001) surface, we computed the electronic band structure under $-2\%, -1.5\%, -1\%, 0.5\%, 0\%, 0.5\%, 1\%, 1.5\%, 2\%$ in plane (X, Y)

biaxial strain. Calculations are performed with CRYSTAL14 using HSE06 as exchange-correlation approximation and the pseudopotential-basis set used in chapter 4. It is useful to compare the strained p(2x1) Ge (001) surface electronic band structure with the strained Ge bulk crystal band structure projected onto the surface first Brillouin zone, that we deduced in section 7.2. We show for example the results of this comparison for -1.5% and 1% of in plane (X, Y) biaxial strain in Figure 8.6 and 8.7.

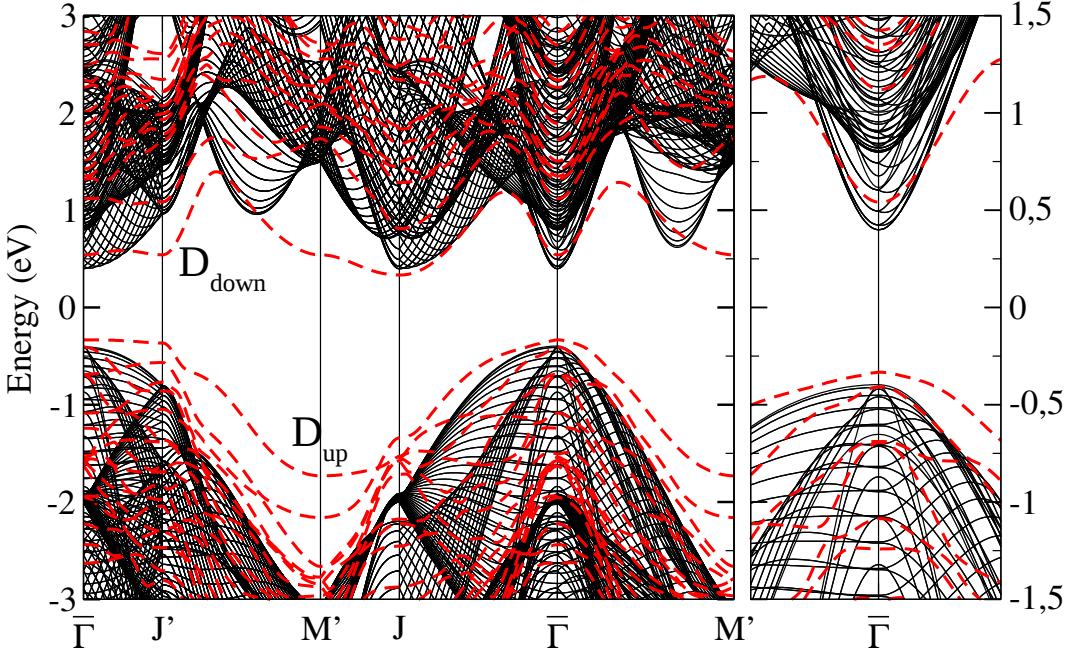


Figure 8.6: Strained Ge bulk band structure projected on the (001) surface first Brillouin zone (black lines) and strained p(2x1) Ge (001) surface bands (red lines) for -1.5% compressive in plane (X, Y) biaxial strain (in the left panel) with zoom on the bands around the $\bar{\Gamma}$ point (in the right panel). The Fermi level of the bulk and surface energies are equalized and put to zero.

From Figures 8.6 and 8.7 we can see that the top valence band of the 1% strained p(2x1) Ge (001) surface electronic band structure is buried into bulk energies at $\bar{\Gamma}$ point, similarly to the unstrained case (Figure 5.6), whereas in the -1.5% case the surface top valence band emerges from the bulk energies, isolating a surface state within the gap. The immersion of strained Ge (001) surface energies into bulk energies results for each positive value of the in plane (X, Y) biaxial strain. For each negative (compressive) value instead, the surface top valence band is outside the bulk energies.

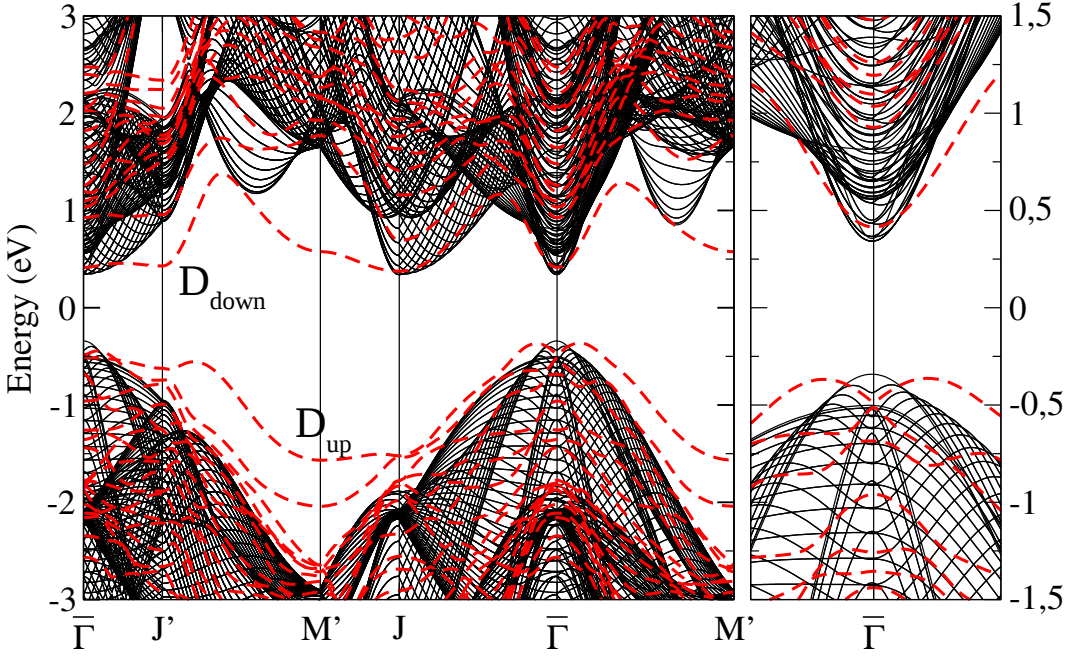


Figure 8.7: Strained Ge bulk band structure projected on the (001) surface Brillouin zone (black continuous lines) and strained p(2x1) Ge (001) surface bands (red dashed lines) for 1% tensile in plane (X, Y) biaxial strain (in the left panel) with zoom on the bands around the $\bar{\Gamma}$ point (in the right panel). The Fermi level of the bulk and surface energies are equalized and put to zero.

For the case of -1.5% biaxial strain, we show in Figure 8.8 the contributions to the electronic density of surface states of the s and p_X, p_Y, p_Z atomic orbitals of the "up" and "down" Ge dimer atom (by inspection, d orbitals can be neglected), in the energy range from 3eV to 3eV. The contributions of the electronic eigenfunctions on the p -type orbitals, and in particular on the p_Z components, are prevalent both in the valence and in the conduction bands. We performed this analysis also in the case of 1% biaxial tensile strain; the comparison of the PDOS between the -1.5% and the 1% biaxial strain values is shown in Figure 8.9. The main difference between the two projections is that in the case of -1.5% biaxial strain the top valence band eigenfunctions are mostly composed by p_X orbitals, whereas in the 1% case they are mostly p_Z . This observation suggests that complete isolation of surface states, under negative values of biaxial strain, may be associated to a spatial rearrangement of the chemical bond charge density between the surface Ge dimer atoms.

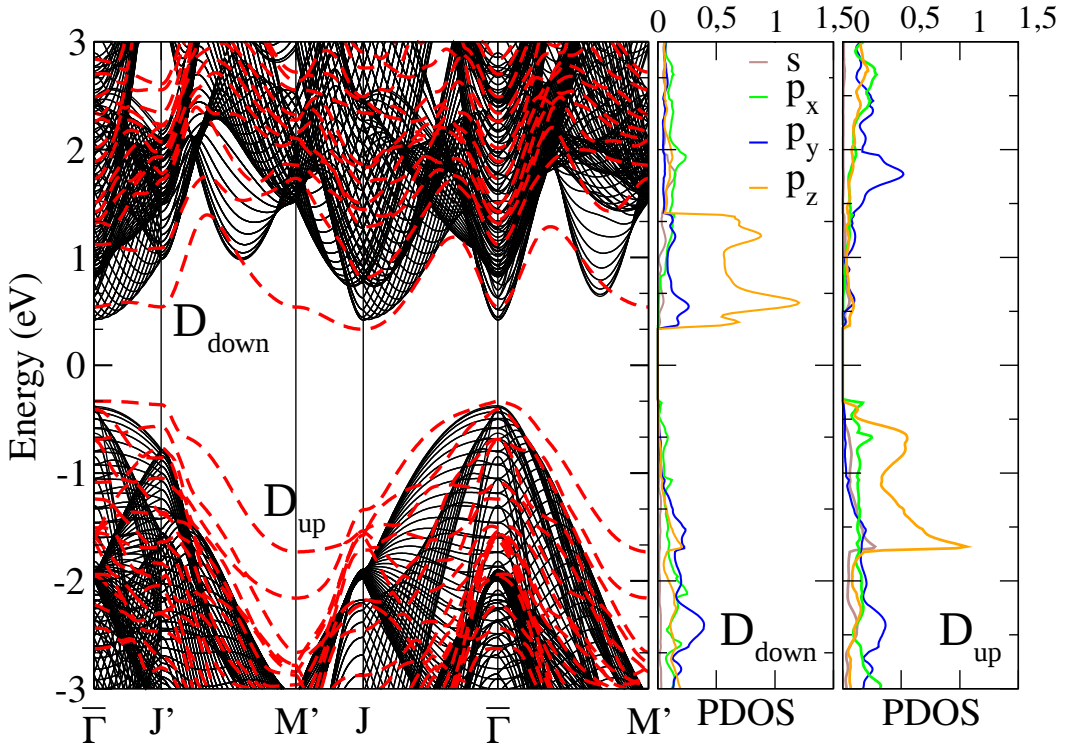


Figure 8.8: Strained Ge bulk band structure of Figure 8.6 with the resolved projected density of states (in units of states/eV/cell) on the D_{up} and on the D_{down} atoms.

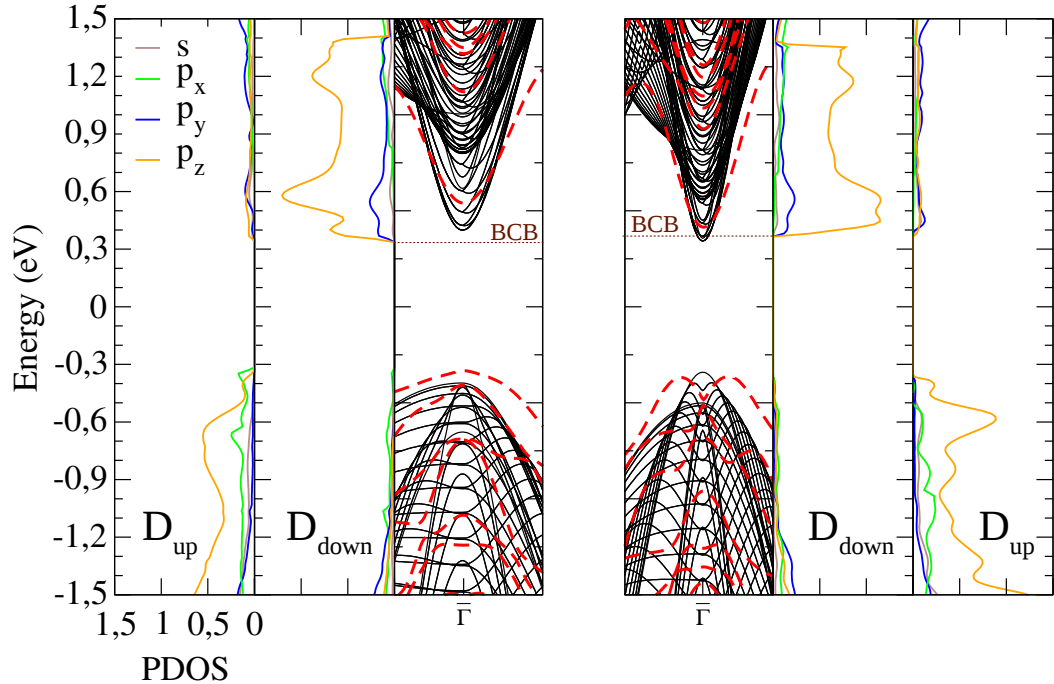


Figure 8.9: Comparison between projected density of the dimer surface states in the case of -1.5% compressive (in three left panels) and 1% tensile biaxial strain values (in the three right panels). The energy levels of the bottom of the conduction bands (BCB) are indicated by dashed brown lines.

For completeness, we present in Figure 8.10 and Table 8.1 the behaviour of p(2x1) Ge (001) surface fundamental energy gap under in plane (X, Y) biaxial strain, compared to the Ge crystal bulk direct and indirect energy gap energies under the same strain conditions. In conclusion we notice that, in contrast with the work of Miao Zhou et al. [29] on the (2x1) Si-(001) surface, we cannot isolate the D_{up} bands from the bulk energies for tensile strain values of biaxial strain, but only for compressive ones. A drawback is that, as it can be seen from Figure 8.6, the isolated valence surface states at $\bar{\Gamma}$ point have lower curvature (and therefore larger effective masses) than the bulk top valence band at $\bar{\Gamma}$. The whole of the behaviours of the Ge (001) surface structural and electronic properties presented in this chapter, i.e. the substantial soft dependence of the dimer spatial configuration and of the electronic band fundamental gap upon deformations, may be finally reconducted to the very tight chemical bond between surface Ge dimer atoms, which is highly localized and seems to be practically unaffected by moderate changes of the surface cell dimensions.

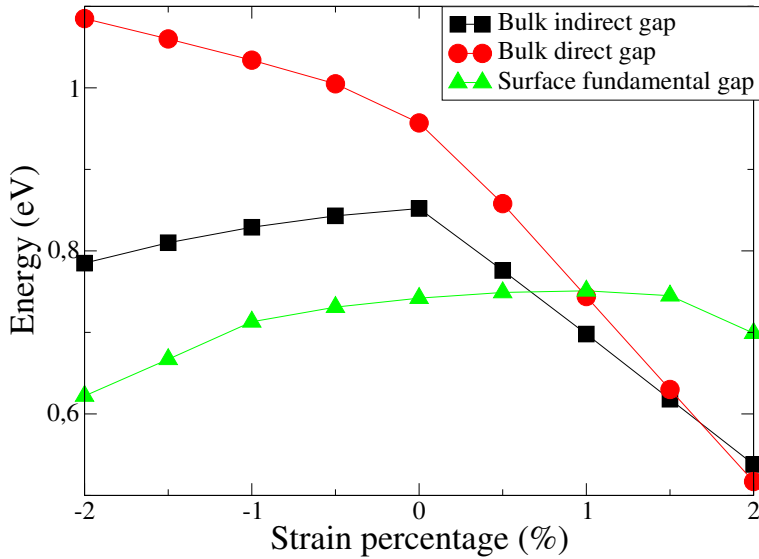


Figure 8.10: Comparison between p(2x1) Ge (001) surface fundamental gap energy (green symbols) and Ge bulk crystal behaviour direct and indirect gap energies (red and black symbols) under in plane (X, Y) strain application.

Strain %	Ge bulk fundamental gap	Ge bulk direct gap	Ge surface fundamental gap
-2%	0.785	1.085	0.622
-1.5%	0.810	1.060	0.667
-1%	0.829	1.034	0.713
-0.5%	0.843	1.005	0.731
0%	0.852	0.957	0.742
0.5%	0.776	0.858	0.749
1%	0.698	0.744	0.751
1.5%	0.618	0.630	0.745
2%	0.517	0.517	0.699

Table 8.1: Direct and indirect energy gap values for the Ge bulk crystal and for the p(2x1) Ge (001) surface under in-plane (X, Y) biaxial strain application.

8.3 Uniaxial strain along Y direction on p(2x1) Ge (001) surface

We present finally our results of the study of uniaxial strain along the Y direction on the p(2x1) Ge (001) surface, adopting the same method discussed for the biaxial strain.

We therefore consider uniaxial strain along the Y direction of percent values $-2\%, -1.5\%, -1\%, 0.5\%, 0\%, 0.5\%, 1\%, 1.5\%, 2\%$ of the simulation cell of Figure 8.1, and relax the degrees of freedom of the Ge atoms belonging to the first five layers of the Ge (001) surface, by means of the QUANTUM ESPRESSO code with the PBEsol exchange-correlation functional. As for the case of in plane (X, Y) biaxial strain, we consider convenient to start the relaxation process from a configuration where all the Ge atomic position are calculated according the elasticity theory. We use a cutoff of 100 Ry for the plane wave basis-set and a Monkhorst-Pack grid of dimensions 12x6x1. We display the behaviour of dimer length and dimer bond angle under uniaxial strain in Figure 8.11 (a) and (b), respectively. We notice from

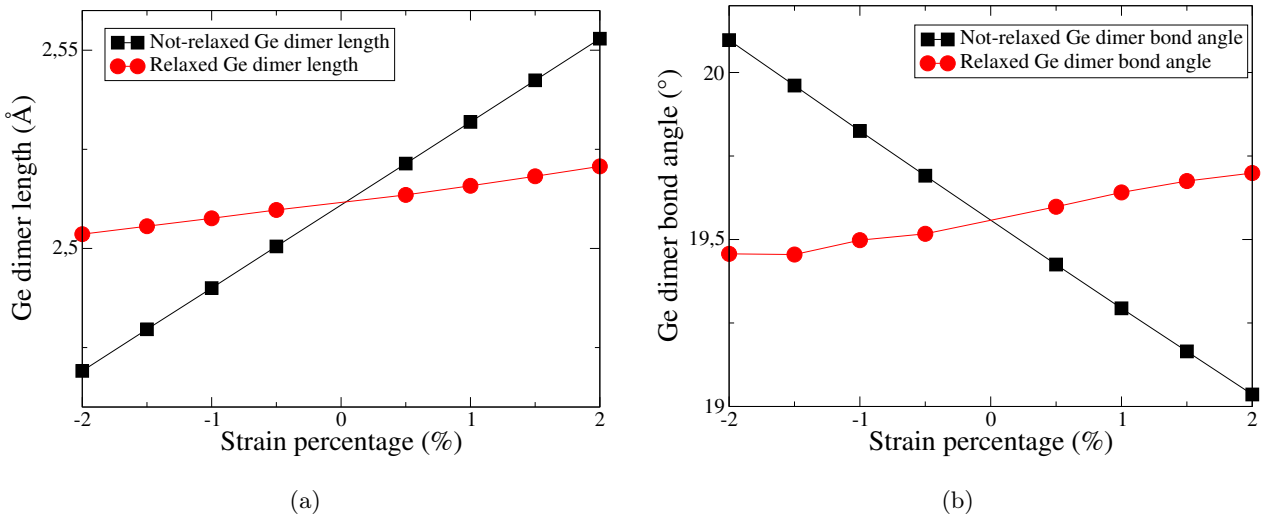
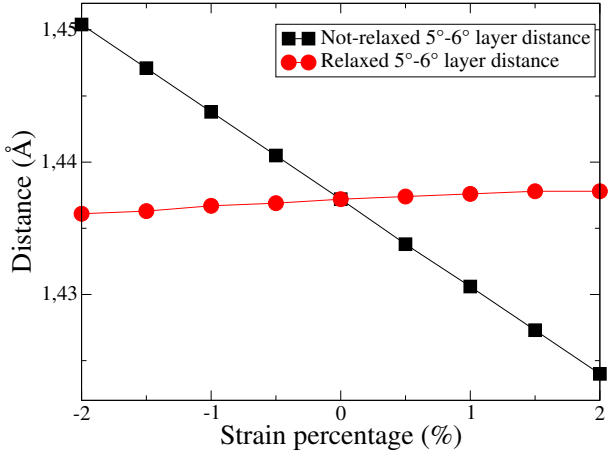


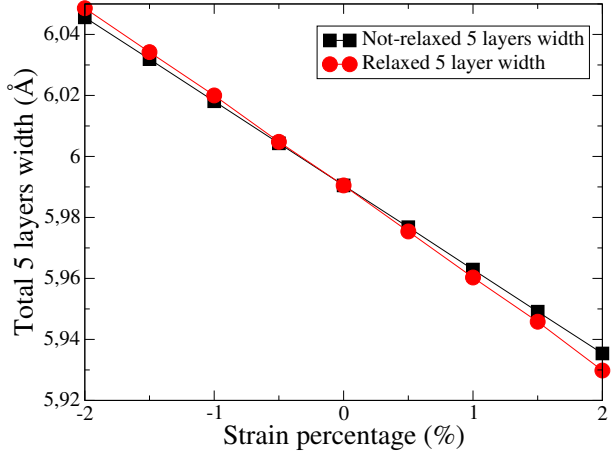
Figure 8.11: (a) Dimer length and (b) bond angle behaviour of the p(2x1) Ge (001) surface asymmetric dimer under uniaxial strain along the Y direction before (black symbols) and after (red symbols) relaxation of Ge atomic positions.

Figure 8.11 that, as in the case of biaxial strain, the dimer length is only slightly affected by uniaxial strain, whereas the bond angle increases proportionally to the uniaxial strain percentage. We checked that the results of Figure 8.11 (a) and (b) are not affected by the computational precision of the elastic compliance tensor, repeating the geometric optimizations using the upper and lower limits of our precision (estimated to be of 10^{-4} strain value) to compute the fixed positions of the Ge atoms from the 6th to the 12th layer. We then investigated the behaviour of the mean interlayer interspacing between the fifth and sixth layers and of the total width of the first 5 layers along the Z direction, as indicated in Figure 8.3, under uniaxial strain. The results are shown in Figure 8.12 (a) and (b).

Once obtained the various relaxed geometries of the strained p(2x1) Ge (001) surface, we computed the electronic band structure under -2% , -1.5% , -1% , 0.5% , 0% , 0.5% , 1% , 1.5% , 2% uniaxial strain along the Y direction. Calculations are performed with CRYSTAL14 using HSE06 as exchange-correlation approximation and the pseudopotential basis set used in chapter 4. If we compare the strained p(2x1) Ge (001) surface electronic band structure with the strained Ge bulk crystal band structure projected onto the surface Brillouin zone, obtained in section 7.2, we find, for example for the case of -1% and



(a)



(b)

Figure 8.12: (a) Interspacing between the fifth and sixth layers and (b) total width of the first 5 layers, for the Ge surface uniaxially strained along the Y direction.

1% of uniaxial strain, the results reported in Figures 8.13 and 8.14. We can see that for both cases the tops of the valence bands are buried into the bulk energies at $\bar{\Gamma}$ point, similarly to the unstrained case of Figure 5.6. This immersion of strained Ge (001) surface energies into bulk energies, differently from the biaxial case, happens for each studied value of the uniaxial strain along the Y direction. For completeness, we present in Figure 8.15 and Table 8.2 the behaviour of p(2x1) Ge (001) surface fundamental gap energy value under uniaxial strain along the Y direction, compared to the Ge crystal bulk direct and indirect gap energies behaviour under the same strain conditions.

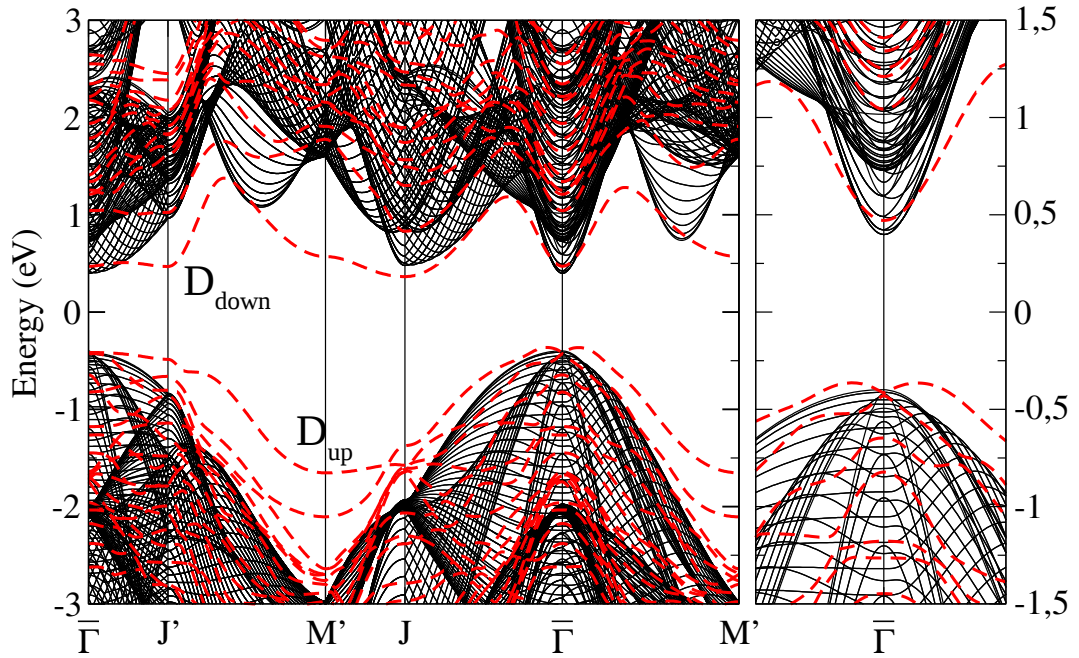


Figure 8.13: Strained Ge bulk band structure projected on the (001) surface first Brillouin zone (black continuous lines) and strained p(2x1) Ge (001) surface bands (red dashed lines) for -1% compressive strain along the Y direction (in the left panel) with zoom around the $\bar{\Gamma}$ point (in the right panel).

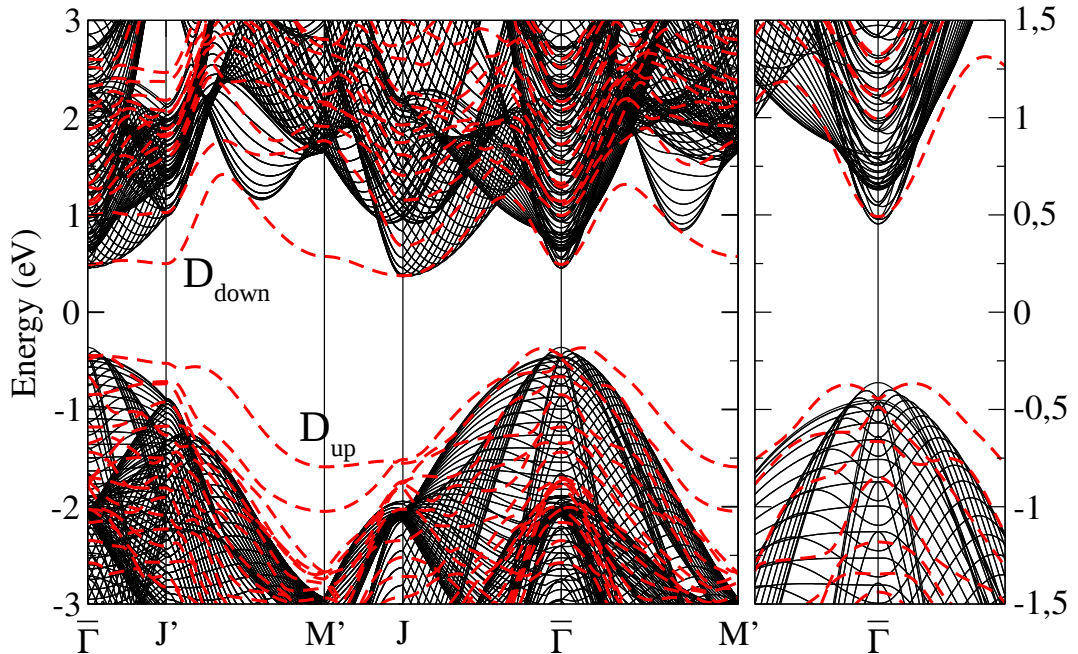


Figure 8.14: Strained Ge bulk band structure projected on the (001) surface first Brillouin zone (black continuous lines) and strained p(2x1) Ge (001) surface bands (red dashed lines) for 1% tensile strain along the Y direction (in the left panel) with zoom on the bands around the $\bar{\Gamma}$ point (in the right panel).

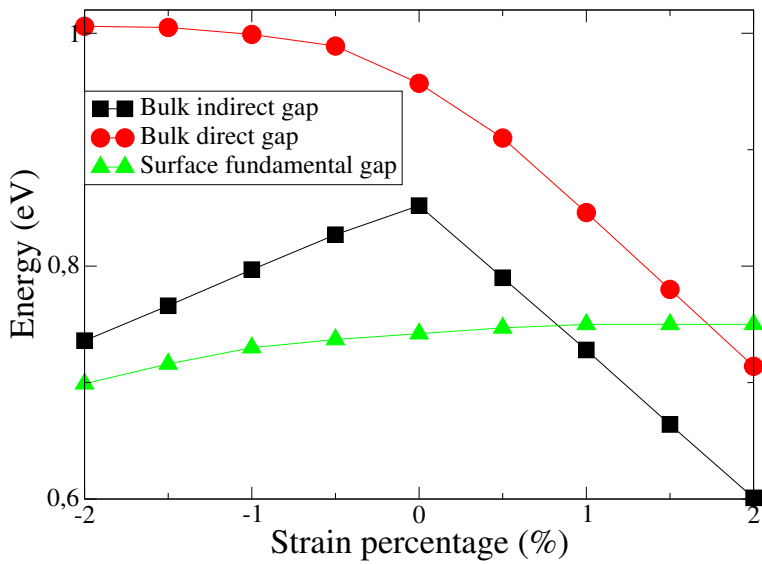


Figure 8.15: Comparison between p(2x1) Ge (001) surface fundamental gap energy (green symbols) and Ge bulk crystal behaviour direct and indirect gap energies (red and black symbols) under uniaxial strain along Y direction.

Strain %	Ge bulk fundamental gap	Ge bulk direct gap	Ge surface fundamental gap
-2%	0.736	1.006	0.699
-1.5%	0.766	1.005	0.716
-1%	0.797	0.999	0.730
-0.5%	0.827	0.989	0.737
0%	0.852	0.957	0.742
0.5%	0.790	0.910	0.747
1%	0.728	0.846	0.750
1.5%	0.664	0.780	0.750
2%	0.601	0.714	0.751

Table 8.2: Direct and indirect energy gap values for the Ge bulk crystal and for the p(2x1) Ge (001) surface under uniaxial strain along the Y direction.

Conclusions and outlook

Nowadays the research in low-dimensional structures (surfaces, interfaces, nanomembranes, nanowires, nanotubes, quantum dots and many others) is witnessing a growing focus. Such materials are of practical appeal because their two (or one) dimensional geometries are a fascinating laboratory for research, aimed to the development of applications of electronic or photonic-based devices. This physical and technological allure, together with novel understanding on fabrication methods, has lately driven many theoretical and experimental investigations in this active and promising field. In this perspective, the electronic band-gap engineering of the group IV semiconductors is surely one of the most intriguing and challenging areas. This work connects with this widespread focus on two dimensional materials, with the aim of working out a novel understanding of the electronic band-gap engineering (through strain) of the (2x1)-reconstructed Ge(001) surface, by means of ab-initio density functional theory techniques, motivated by the lack of results in this fascinating argument.

The Ge (001) surface, which is originated from the Ge bulk diamond crystalline structure truncation along the [001] crystallographic direction, is reconstructed at room temperature in a (2x1) pattern, which means that its two-dimensional periodicity is doubled along the [$\bar{1}10$] crystallographic direction; this reconstruction is due to surface atoms rearrangement into asymmetric dimers, which process is driven by halving of dandling bonds per surface atom created as consequence of the truncation of the crystalline structure. The asymmetry of the dimers plays a central role in the electronic properties of the surface, allowing a rehybridization of the remaining dandling bonds of the surface atoms which ends up in a net charge transfer from the "down" Ge dimer atom to the "up" one. This charge transfer is

the main responsible for the (experimentally observed) semiconductive behaviour of the (2x1) Ge (001) surface. In order to go to the roots of a coherent and clear ab-initio understanding of the electronic band-gap engineering of the (2x1)-reconstructed Ge (001) surface, it is needed to first study the Ge bulk crystal, under relaxed and strained conditions, and the unstrained (2x1)-reconstructed Ge (001) surface, to rightly tune the ab-initio choices as regards pseudopotentials, exchange-correlation functional and working procedures by comparison with experimental data. In the present work our first concern was to show that, even in a simple structure such as the Ge bulk crystal, typical density functional formulations of the exchange-correlation functional such as Local Density Approximation (LDA) and Generalized Gradient Approximation (GGA) lead to misleading results both in the structural and in the electronic properties. To find workable and satisfying expressions of the exchange-correlation approximation we had to implement hybrid functional calculations (HSE06 in particular), at the price of an heavier computational effort, but with the benefits of the satisfactory reproduction of the experimental data (both structural and electronic). As first example of germanium band-gap engineering, we studied the effects of strain application on the Ge bulk crystal; we primarily deduced by ab-initio computation the compliance matrix Λ for the Ge bulk to test the validity of our working procedures in the case of elastic deformation in crystals, by comparison with experimental data; we then showed that, under proper strain application, the position of the electronic band fundamental gap energy changes from indirect to direct (with respect to electronic crystal momenta), in accordance with previous studies. This last result (yet known in the literature) is to be held in high regard because the native indirect nature of the Ge bulk crystal fundamental gap energy would make germanium unfit to light-emitting and laser diodes, because radiative recombination is typically far lower for indirect gap materials; in recent works, Ge nanomembranes have been mechanically strained beyond the accepted threshold for direct-band gap behaviour, leading to strong strain-enhanced luminescence and evidence of population inversion under optical pumping.

For what concerns the numerical simulation of unstrained Ge (001) surface and of its properties, we considered a (2x1) simulation cell consisting in 12 consecutive atomic layers of germanium (extending

orthogonally to the [001] crystallographic direction) properly terminated on the bottom atomic plane by an out-layer of Hydrogen working as passivation element. The number of 12 layers as an approximation to the ideally semi-infinite succession of atomic planes along the [001] direction has been investigated in this thesis by the direct comparison with a 5 layers approximation, which was instead found to be not acceptable for a precise reproduction of structural and electronic properties of the (2x1) Ge (001) surface, as yet known in the literature. We showed numerically, by relaxing the atomic degrees of freedom, that the asymmetric dimers (2x1) reconstruction is indeed a minimum energy configuration and we were able to reproduce the surface dimer bond length, angle and the subsurface dimer-induced strain penetration with very good agreement with previous experimental observations, thus confirming the goodness of our working procedures and the performances of the codes adopted. Once established the steadiness of the (2x1) asymmetric dimer reconstruction, the focus was moved on the computation of the electronic band structure and of the spatial localization of the electronic states of the 12 layer Ge (001) slab. This surface was found to be semiconducting by angle resolved photoemissions and scanning tunneling microscopy observations.

Since surface states isolation in the neighbourhood of the $\mathbf{k} = 0$ electronic crystal momentum has been numerically discovered in the case of the (2x1) Si (001) surface by means of strain application, we wondered if the same goal could be achieved for the (2x1)-reconstructed Ge (001) surface, thus providing another issue of band-structure modulation and engineering for germanium. In this perspective we applied biaxial and uniaxial strain (in our case respectively homogeneous tension along the dimer direction and the orthogonal one, and along the dimer direction only) to the (2x1) Ge (001) surface simulation cell and studied the changes in structural and electronic properties. The first remarkable discovery was the substantial steadiness of the dimer bond length and angle values under external elastic perturbations. This behaviour of the Ge surface dimer (which has not been reported instead for the Si surface dimer) highlights the role played by the strong chemical bond between Ge surface dimer atoms in stabilizing the (2x1) Ge (001) surface atomic configuration. The analysis of the electronic band structure revealed that the threshold for complete isolation of valence surface states for each value of the

electron crystal momentum \mathbf{k} , included the $\mathbf{k} = 0$ region, is below -0.5% (compressive) in plane biaxial strain. Complete isolation of surface states is important in the perspective of designing new devices based on integrated photonic or on surface transport; in this last context, the presence of electronic band energies corresponding to forbidden bulk energies allows to separate surface transport from bulk transport, so as to study the mobility difference between surface and bulk carriers and interaction of surface states with bulk bands. The resulting electronic transport properties are intriguing, and as microelectronic devices shrink even further, and surface-to-volume ratios increase, surfaces will play an increasingly important role and a complete atomic description of the (2x1) Ge (001) surface and of its structural and electronic properties, under strained conditions, is of high interest for interfaces and heterostructures [111].

In order to provide another possible example of surface band-gap engineering, we wondered whether the p(2x1) Ge(001) surface electronic fundamental gap, which is indirect in relaxed conditions, may become direct under strained conditions. Unfortunately, for all the studied strain values of the Ge(001) surface simulation cell, the surface fundamental band gap is indirect. Precisely, for all the biaxial strain negative (compressive) values the top of the surface valence bands occurs at the $\bar{\Gamma}$ point of the Brillouin zone and the bottom of the surface conduction bands at the J' point. This behaviour is shown in Figure 8.16 (a), specialized to the case of -1.5% biaxial compressive strain. For positive (tensile) biaxial strains, but under the value of 1.7%, the top of the surface valence bands occurs in the neighbourhood of $\bar{\Gamma}$ while the bottom of surface conduction bands is at J' (Figure 8.16 (b)), whereas for values larger than 1.7% the bottom of surface conduction bands is at $\bar{\Gamma}$ (Figure 8.16 (c)). Finally, the position of the Ge(001) surface fundamental gap, for all the studied uniaxial strain values, is indirect between the neighbourhood of $\bar{\Gamma}$ and the J' point, as shown in Figure 8.16 (d). Unfortunately, the indirect nature of the p(2x1) Ge (001) surface fundamental gap limits the possibilities for the development of optical devices exploiting surface states of germanium.

In all the ab-initio structural and electronic band structure calculations presented in this thesis I disregarded the relativistic spin-orbit effects. Indeed, spin-orbit effects on the electronic energies

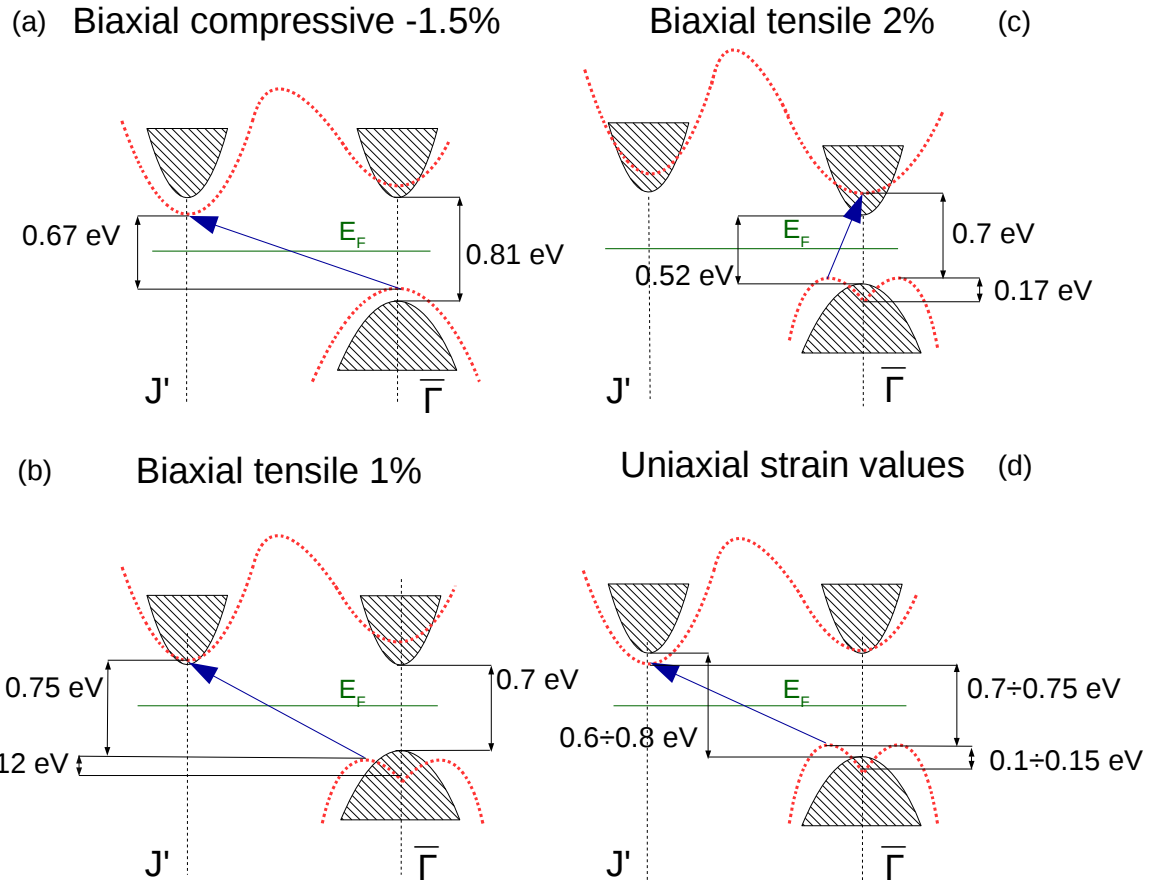


Figure 8.16: Schematic of the p(2x1) Ge(001) band structure in the case of (a) -1.5 % biaxial compressive strain, (b) 1% and (c) 2% biaxial tensile strain, and (d) a generic studied value of the uniaxial strain. The bulk energies correspond to black shaded areas, the surface band energies are represented by dashed red lines. The blue arrows indicate the top of the surface valence bands (tail) and the bottom of the surface conduction bands (head). The bulk and surface energies are compared equalizing the Fermi levels.

become very important for the heavy elements of the periodic table (such as germanium, where the spin orbit splitting of the valence band at $\mathbf{k} = 0$ is of about $\Delta_{S.O.} = 0.29\text{eV}$ against a fundamental gap of 0.744eV [37]). At present most of the ab-initio computational codes provide tools to implement the spin-orbit interaction only with non hybrid functionals (such as LDA and GGA), which we showed to be unable to reproduce the structural and electronic properties of germanium crystal. In the germanium bulk crystal, both in relaxed or strained conditions, this technical limit can be overcome thanks to

the deformation potential theory; this technique, developed through the years by several authors (for instance Kleiner and Roth [112], Bardeen and Shockley [107], Pollack and Cardona [109, 113], Van de Walle and Martin [114], and Picus and Bir [108]) provide perturbative analytical working expressions to take into account (*a posteriori*) the spin-orbit and strain effects on the Ge diamond bulk crystal. Since at the Ge (001) surface the ideal crystal symmetry is broken (especially for the (2x1)-reconstructed surface) this deformation potential technique should be applied with some caution; anyway, we expect that the spin-orbit effects on the surface states energies are of the same magnitude as in the bulk case. To validate the analysis of surface states presented in this work, or to see whether spin-orbit interaction opens the doors to other types of applications, we intend to investigate coherently, in future developments, the ab-initio inclusion of spin-orbit effects. Moreover the band structures obtained in the different cases and the analysis of the density of states will allow us to evaluate the optical properties and in particular the conditions for optical gain of the samples under strained conditions. Eventually the present calculation is a starting step for the evaluation of quantum transport of properly designed germanium nanostructures.

Bibliography

- [1] C. Boztug, J.R. Sánchez-Pérez, F. Cavallo, M.G. Lagally and R. Paiella, *Strained-Germanium Nanostructures for Infrared Photonics*, *ACS Nano* **8**, 3136 (2012).
- [2] H.J.W. Zandvliet, *The Ge(001) surface*, *Phys. Rep.* **338**, 1 (2003).
- [3] K. Wada and L.C. Kimerling, *Photonics and electronics with Germanium*, (Wiley-VCH, Singapore 2015).
- [4] R.E. Schlier and H.E. Farnsworth, *Structure and Adsorption Characteristics of Clean Surfaces of Germanium and Silicon*, *J. Chem. Phys.* **30**, 917 (1959).
- [5] W. Mönch, *Nonlinear optimization*, (Springer-Verlag, Berlin 1982).
- [6] W.S. Yang, F. Jona and P.M. Marcus, *The (2x1) structural reconstruction of Si(001)*, *Solid State Commun.* **43**, 847 (1981).
- [7] G. Jayaram, P. Xu and L.D. Marks, *Structure of Si(100)-(2x1) surface using UHV transmission electron diffraction*, *Phys. Rev. Lett.* **71**, 3489 (1993).
- [8] E.L. Bullock, R. Gunnella, L. Patthey, T. Abukawa, S. Kono, C.R. Natoli and L.S.O. Johansson, *Surface Core-Level Photoelectron Diffraction from Si Dimers at the Si(001)-(2x1) Surface*, *Phys. Rev. Lett.* **74**, 2756 (1995).
- [9] C.A. Lucas, C.S. Dower, D.F. McMorrow, G.C.L. Wong, F.J. Lamelas and P.H. Fuoss, *Order-*

- disorder c(4x2)-(2x1) transition on Ge(001): An in situ X-ray scattering study, Phys. Rev. B* **47**, 10275 (1993).
- [10] D.J. Chadi, *Atomic and Electronic Structures of Reconstructed Si(100) Surfaces, Phys. Rev. Lett.* **43**, 43 (1979).
- [11] P. Krüger, A. Mazur, J. Pollmann and G. Wolfgarten, *First-Principles Electronic Structure Theory for Semi-infinite Semiconductors with Applications to Ge(001) (2×1) and Si(001) (2×1), Phys. Rev. Lett.* **57**, 1468 (1986).
- [12] M. Needels, M.C. Payne and J.D. Joannopoulos, *Ab initio molecular dynamics on the Ge(100) surface, Phys. Rev. Lett.* **58**, 1765 (1987).
- [13] J.A. Appelbaum and D.R. Hamann, *Theory of reconstruction induced subsurface strain-application to Si(100), Surf. Sci.* **74**, 21 (1978).
- [14] H. Ibach and H. Lüth, *Solid-State Physics*, (Springer-Verlag, Berlin 2009).
- [15] J.G. Nelson, R.S. Williams, S.W. Robey, J.G. Tobin and D.A. Shirley, *Mapping bulk Ge electronic energy bands along Δ using ARPES spectra of the (001) 2x1 surface, Surf. Sci.* **131**, 290 (1983).
- [16] J.G. Nelson, W.J. Gignac, R.S. Williams, S.W. Robey, J.G. Tobin and D.A. Shirley, *Angle-resolved photoelectron spectroscopy investigation of intrinsic surface states on the Ge(001)-(2x1) reconstructed surface, Phys. Rev. B* **27**, 3924 (1983).
- [17] H. Seo, R.C. Hatch, P. Ponath, M. Choi, A.B. Posadas and A.A. Demkov, *Supplementary material for: Critical differences in the surface electronic structure of Ge(001) and Si(001): ab-initio theory and angle-resolved photoemission spectroscopy, Phys. Rev. B* **89**, 115318 (2014).
- [18] L. Kipp, R. Manzke and M. Skibowski, *The surface band gaps of Ge(001)2×1, Surf. Sci.* **269**, 854 (1992).

- [19] J.A. Kubby, J.E. Griffith, R.S. Becker and J.S. Vickers, *Tunneling microscopy of Ge(001)*, *Phys. Rev. B* **36**, 6079 (1987).
- [20] H. Neddermeyer, *Scanning tunneling microscopy of semiconductor surfaces*, *Rep. Prog. Phys.* **59**, 701 (1996).
- [21] P. Handler and W.M. Portnoy, *Electronic Surface States and the Cleaned Germanium Surface*, *Phys. Rev.* **116**, 516 (1959).
- [22] S. Yang, F. Liu, C. Wu and S. Yang, *Tuning Surface Properties of Low Dimensional Materials via Strain Engineering*, *Small* **12**, 4028 (2016).
- [23] M. El Kurdi, G. Fishman, S. Sauvage and P. Boucaud, *Band structure and optical gain of tensile-strained germanium based on a 30 band $k\cdot p$ formalism*, *J. App. Phys.* **107**, 013710 (2010).
- [24] M. El Kurdi, H. Bertin, E. Martincic, G. Fishman, S. Sauvage, P. Boucaud and A. Bosseboeuf, *Control of direct band gap emission of bulk germanium by mechanical tensile strain*, *J. App. Phys.* **96**, 041909 (2010).
- [25] S. Gupta, B. Magyari-Kope, Y. Nishi and K.C. Saraswat, *Achieving direct band gap in germanium through integration of Sn alloying and external strain*, *J. App. Phys.* **113**, 073707 (2013).
- [26] G. Pizzi, M. Virgilio and G. Grossi, *Tight-Binding Calculation of Optical Gain in Tensile Strained [001]-Ge/SiGe Quantum Wells*, *Nanotechnology* **21**, 055202 (2010).
- [27] H. Tahini, A. Chroneos, R.W. Grimes, U. Schwingenschlögl and A. Dimoulas, *Strain-Induced Changes to the Electronic Structure of Germanium*, *J. Phys. Condens. Matter* **24**, 195802 (2012).
- [28] J. Munguía, G. Bremond, J.M. Bluet, J.M. Hartmann and M. Mermoux, *Strain dependence of indirect band gap for strained silicon on insulator wafers*, *Appl. Phys. Lett.* **93**, 102101 (2008).
- [29] M. Zhou, Z. Liu, Z. Wang, Z. Bai, Y. Feng, M.G. Lagally and F. Liu, *Strain-Engineered Surface*

Transport in Si(001): Complete Isolation of the Surface State via Tensile Strain, Phys. Rev. B **111**, 246801 (2013).

- [30] P. Giannozzi, S. Baroni, N. Bonini, M. Calandra, R. Car, C. Cavazzoni, D. Ceresoli, G.L. Chiarotti, M. Cococcioni, I. Dabo, A. Dal Corso, S. Fabris, G. Fratesi, S. de Gironcoli, R. Gebauer, U. Gerstmann, C. Gougoussis, A. Kokalj, M. Lazzeri, L. Martin-Samos, N. Marzari, F. Mauri, R. Mazzarello, S. Paolini, A. Pasquarello, L. Paulatto, C. Sbraccia, S. Scandolo, G. Sclauzero, A. P. Seitsonen, A. Smogunov, and P. Umari and R. M. Wentzcovitch, *QUANTUM ESPRESSO: a modular and open-source software project for quantum simulations of materials.*, *J. Phys. Condens. Matter* **21**, 246807 (2009).
- [31] R. Dovesi, R. Orlando, A. Erba, C.M. Zicovich-Wilson, B. Civalleri, S. Casassa, L. Maschio, M. Ferrabone, M. De La Pierre, P. D'Arco, Y. Noel, M. Causa, M. Rerat and B. Kirtman, *CRYSTAL14: A program for the ab initio investigation of crystalline solids*, *Int. J. Quantum Chem.* **114**, 1287 (2014).
- [32] A. J. Cohen, P. Mori-Sánchez and W. Yang, *Insights into Current Limitations of Density Functional Theory*, *Phys. Rev. B* **77**, 115123 (2008).
- [33] A.J. Cohen, P. Mori-Sánchez and W. Yang, *Localization and Delocalization Errors in Density Functional Theory and Implications for Band-Gap Prediction*, *Phys. Rev. Lett.* **100**, 146401 (2008).
- [34] J. Heyd, G.E. Scuseria and M. Ernzerhof, *Hybrid functionals based on a screened Coulomb potential*, *J. Chem. Phys.* **118**, 8207 (2003).
- [35] J. Heyd, G.E. Scuseria and M. Ernzerhof, *Erratum: "Hybrid functionals based on a screened Coulomb potential" [J. Chem. Phys. 118, 8207 (2003)]*, *J. Chem. Phys.* **124**, 219906 (2006).
- [36] J. Heyd and G.E. Scuseria, *Efficient hybrid density functional calculations in solids: assessment*

of the Heyd-Scuseria-Ernzerhof screened Coulomb hybrid functional., J. Chem. Phys. **121**, 1187 (2004).

- [37] O. Madelung, *Semiconductors: Data Handbook*, (Springer-Verlag, Berlin 2004).
- [38] R.M Tromp, R.J. Hamers and J.E. Demuth, *Si(001) Dimer Structure Observed with Scanning Tunneling Microscopy*, *Phys. Rev. Lett.* **55**, 1303 (1985).
- [39] T. Sato, T. Iwatsuki and H. Tachihara, *Detection of the flip-flop motion of buckled dimers on a Ge(001) surface by STM*, *J. Electron Microsc.* **48**, 1 (1999).
- [40] H. Shigekawa, K. Hata, K. Miyake, M. Ishida and S. Ozawa, *Origin of the symmetric dimers in the Si(100) surface*, *Phys. Rev. B* **55**, 15448 (1997).
- [41] X.R. Qin and M.G. Lagally, *View of the empty states of the Si(100)-(2×1) surface via scanning tunneling microscopy imaging at very low biases*, *Phys. Rev. B* **59**, 7293 (1999).
- [42] M. Needels, M.C. Payne and J.D. Joannopoulos, *High-order reconstructions of the Ge(100) surface*, *Phys. Rev. Lett.* **38**, 5543 (1988).
- [43] Y. Yoshimoto, Y. Nakamura, H. Kawai, M. Tsukada and M. Nakayama, *Ge(001) surface reconstruction studied using a first-principles calculation and a Monte Carlo simulation*, *Phys. Rev. B* **61**, 1965 (2000).
- [44] O. Gurlu, H.J.W. Zandvliet and B. Poelsema, *Electronic Properties of (2x1) and c(4x2) Domains on Ge(001) Studied by Scanning Tunneling Spectroscopy*, *Phys. Rev. Lett.* **93**, 6 (2004).
- [45] R.M. Dreizler and E.K.U. Gross, *Density Functional Theory*, (Springer-Verlag, Berlin 1990).
- [46] R.M. Martin, *Electronic structure. Basic theory and practical methods*, (Cambridge University Press, Cambridge 2004).
- [47] G.F. Giuliani and G. Vignale, *Quantum Theory of the Electron Liquid*, (Cambridge University Press, Cambridge 2005).

- [48] G. Grosso and G.P. Parravicini, *Solid State Physics*, (Elsevier, Oxford 2014).
- [49] P. Hohenberg and W. Kohn, *Inhomogeneous Electron Gas*, *Phys. Rev.* **136**, B864 (1964).
- [50] W. Kohn and L. J. Sham, *Self-Consistent Equations Including Exchange and Correlation Effects*, *Phys. Rev.* **A1133**, 140 (1965).
- [51] C.G. Broyden, *A Class of Methods for Solving Nonlinear Simultaneous Equations*, *Math. Comp.* **19**, 577 (1965).
- [52] D.G. Anderson, *Iterative procedures for non-linear integral equations*, *J. Assoc. Comput. Mach.* **12**, 547 (1965).
- [53] J.P. Perdew and A. Zunger, *Self-interaction correction to density-functional approximations for many-electron systems*, *Phys. Rev. B* **23**, 5048 (1981).
- [54] J.P. Perdew, K.Burke and M.Ernzerhof, *Generalized Gradient Approximation Made Simple*, *Phys. Rev. Lett.* **77**, 3865 (1996).
- [55] A.D. Becke, *Density-functional thermochemistry. III. The role of exact exchange*, *J. Chem. Phys.* **98**, 5648 (1993).
- [56] S.J. Clarck and J. Robertson, *Screened exchange density functional applied to solids*, *Phys. Rev. B* **82**, 085208 (2010).
- [57] D.H. Hamann, M. Schluter and C. Chiang, *Norm-Conserving Pseudopotentials*, *Phys. Rev. Lett.* **43**, 1494 (1979).
- [58] V.R. Saunders, *Ab initio Hartree-Fock calculations for periodic systems*, *Faraday Symp. Chem. S.* **19**, 79 (1984).
- [59] F. Gygi and A. Baldereschi, *Self-consistent Hartree-Fock and screened-exchange calculations in solids: Application to silicon*, *Phys. Rev.* **34**, 4405 (1986).

- [60] C. Pisani et al., *Quantum-Mechanical Ab-initio Calculation of the Properties of Crystalline Materials*, (Springer-Verlag, Berlin 1996).
- [61] P. Pulay, *Ab initio calculation of force constants and equilibrium geometries in polyatomic molecules*, *Mol. Phys.* **17**, 197 (1969).
- [62] H.B. Schlegel, *Estimating the Hessian for gradient-type geometry optimizations*, *Theor. Chim. Acta* **66**, 333 (1984).
- [63] J.M. Wittbrodt and H.B. Schlegel, *Estimating stretching force constants for geometry optimization*, *Comp. Theor. Chem.* **398**, 55 (1997).
- [64] R. Lindh, A. Bernhardsson, G. Ktlström and P.A. Malmqvist, *On the use of a Hessian model function in molecular geometry optimizations*, *Chem. Phys. Lett.* **241**, 423 (1995).
- [65] H.B. Schlegel, *Theory and Applications of Computational Chemistry: The First Forty Years*, (Elsevier, Amsterdam 2005).
- [66] H.B. Schlegel, *Optimization of equilibrium and transition structures*, *J. Comput. Chem.* **3**, 214 (1982).
- [67] M.J.D. Powell, *Nonlinear optimization*, (New York Academic Press, New York 1982).
- [68] F. Herman, *The Electronic Energy Band Structure of Silicon and Germanium*, *Proceedings of the IRE* **12**, 1703 (1955).
- [69] W. Shockley, *Electrons and Holes in Semiconductors*, (D. Van Nostrand and Company, New York 1950).
- [70] F. Herman, *Calculation of the Energy Band Structures of the Diamond and Germanium Crystals by the Method of Orthogonalized Plane Waves*, *Phys. Rev.* **93**, 1214 (1955).
- [71] G.G. Macfarlane, T.P. McLean, J.E. Quarrington and V. Roberts, *Fine Structure in the Absorption-Edge Spectrum of Ge*, *Phys. Rev.* **108**, 1337 (1957).

- [72] G. Dresselhaus, A.F. Kip and C. Kittel, *Observation of Cyclotron Resonance in Germanium Crystals*, *Phys. Rev.* **92**, 827 (1953).
- [73] G. Dresselhaus, A.F. Kip and C. Kittel, *Cyclotron Resonance of Electrons and Holes in Silicon and Germanium Crystals*, *Phys. Rev.* **98**, 368 (1955).
- [74] G. Dresselhaus, *Spin-Orbit Coupling Effects in Zinc Blende Structures*, *Phys. Rev.* **100**, 580 (1955).
- [75] M.E. Straumanis and E.Z. Aka, *Lattice Parameters, Coefficients of Thermal Expansion, and Atomic Weights of Purest Silicon and Germanium*, *J. App. Phys.* **23**, 330 (1952).
- [76] L.M. Roth, B. Lax and S. Zwerdling, *Theory of Optical Magneto-Absorption Effects in Semiconductors*, *Phys. Rev.* **114**, 90 (1959).
- [77] M. Cardona and G.H. Pollak, *Energy-Band Structure of Germanium and Silicon: The $k \cdot p$ Method*, *Phys. Rev.* **142**, 530 (1966).
- [78] R. Chelikosky and M.L. Cohen, *Nonlocal pseudopotential calculations for the electronic structure of eleven diamond and zinc-blende semiconductors*, *Phys. Rev. B* **14**, 556 (1976).
- [79] M.T. Yin and M.L. Cohen, *Theory of static structural properties, crystal stability, and phase transformations: Application to Si and Ge*, *Phys. Rev. B* **26**, 5668 (1982).
- [80] J.F.C. Baker and M.Hart, *An absolute measurement of the lattice parameter of germanium using multiple-beam X-ray diffractometry*, *Acta Crystallogr. Sect. A* **31**, 2297 (1975).
- [81] C.H. Yang, Z.Y. Yu, Y.M. Liu, P.F. Lu, T. Gao, M. Li and S. Manzoor, *Dependence of electronic properties of germanium on the in-plane biaxial tensile strains*, *Phys. Rev. B* **427**, 62 (2013).
- [82] K. Hummer, J. Harl and G. Kresse, *Heyd-Scuseria-Ernzerhof hybrid functional for calculating the lattice dynamics of semiconductors*, *Phys. Rev. B* **80**, 115205 (2009).

- [83] K. Sakata, B. Magyari-Kope, S. Gupta, Y. Nishi, A. Blom and P. Deak, *The effects of uniaxial and biaxial strain on the electronic structure of germanium*, *Comp. Mater. Sci.* **112**, 263 (2016).
- [84] A. Fleszar, *LDA, GW, and exact-exchange Kohn-Sham scheme calculations of the electronic structure of sp semiconductors*, *Phys. Rev. B* **64**, 245204 (2001).
- [85] W. Ku and A.G. Eguiluz, *Band-Gap Problem in Semiconductors Revisited: Effects of Core States and Many-Body Self-Consistency*, *Phys. Rev. Lett.* **89**, 126401 (2002).
- [86] W.G. Aulbur, M. Stadele and A. Gorling, *Exact-exchange-based quasiparticle calculations*, *Phys. Rev. B* **62**, 7121 (2000).
- [87] M.F. Peintinger, D.V. Oliveira and T. Bredow, *Consistent Gaussian basis sets of triple-zeta valence with polarization quality for solid-state calculations.*, *J. Comput. Chem.* **34**, 451 (2012).
- [88] C. Lee, W. Yang and R.G. Parr, *Development of the Colle-Salvetti correlation-energy formula into a functional of the electron density*, *Phys. Rev. B* **37**, 785 (1988).
- [89] J.P. Perdew, M. Ernzerhof and K. Burke, *Rationale for mixing exact exchange with density functional approximations*, *J. Chem. Phys.* **105**, 9982 (1996).
- [90] L. Schimka, J. Harl and G. Kresse, *Improved hybrid functional for solids: the HSEsol functional.*, *J. Chem. Phys.* **134**, 024116 (2011).
- [91] J. Heyd, J.E. Peralta, G.E. Scuseria and R. Martin, *Energy Band Gaps and Lattice Parameters Evaluated with the Heyd-Scuseria-Ernzerhof Screened Hybrid Functional*, *J. Chem. Phys.* **123**, 174101 (2005).
- [92] R.J. Culbertson, *Subsurface strain in the Ge(001) and Ge(111) surfaces and comparison to silicon*, *Surf. Sci.* **167**, 1 (1986).
- [93] M.W. Radny, G.A. Shah, S.R. Schofield, P.V. Smith and N.J. Curson, *Valence Surface Electronic States on Ge(001)*, *Phys. Rev. Lett.* **100**, 395502 (2008).

- [94] B. Yan, C. Yam, A.L. da Rosa and T. Frauenheim, *Comment on "Valence Surface Electronic States on Ge(001)"*, *Phys. Rev. B* **103**, 189701 (2009).
- [95] M.W. Radny, G.A. Shah, S.R. Schofield, P.V. Smith and N.J. Curson, *Radny et al. reply*, *Phys. Rev. Lett.* **103**, 189702 (2009).
- [96] P. Krüger and J. Pollmann, *Dimer Reconstruction of Diamond, Si, and Ge (001) Surfaces*, *Phys. Rev. Lett.* **74**, 1155 (1995).
- [97] P. Krüger and J. Pollmann, *Theory of adsorption: Ordered monolayers from Na to Cl on Si(001) and Ge(001)*, *Appl. Phys. A* **59**, 5 (1994).
- [98] R. Rossmann, H.L. Meyerheim, V. Jahns, J. Wever, W. Moritz, D. Wolf, D. Dornisch and H. Schulz, *The Ge(001) (2x1) reconstruction: asymmetric dimers and multilayer relaxation observed by grazing incidence X-ray diffraction*, *Surf. Sci.* **279**, 199 (1992).
- [99] H. Seo, R.C. Hatch, P. Ponath, M. Choi, A.B. Posadas and A.A. Demkov, *Critical differences in the surface electronic structure of Ge(001) and Si(001): ab-initio theory and angle-resolved photoemission spectroscopy*, *Phys. Rev. B* **89**, 115318 (2014).
- [100] S. Ferrer, X. Torrelles, V.H. Etgens, H. A. van der Vegt and P. Fajardo, *Atomic Structure of the c(4x2) Surface Reconstruction of Ge(001) as Determined by X-Ray Diffraction*, *Phys. Rev. Lett.* **75**, 1771 (1995).
- [101] P. Krüger M. Rohlfing and J. Pollmann, *Quasiparticle band structure of clean, hydrogen and sulfur-terminated Ge(001) surfaces*, *Phys. Rev. B* **54**, 13759 (1996).
- [102] L.D. Landau and E.M. Lifshitz, *Theory of elasticity*, (Elsevier, Oxford 1986).
- [103] M.A. Hopcroft, W.D. Nix, and T.W. Kenny, *What is the Young's Modulus of Silicon?*, *J. Microelectromech. Syst.* **19**, 229 (2010).

- [104] J.J. Wortman and R.A. Evans, *Young's modulus, shear modulus and Poisson ratios in Silicon and Germanium*, *J. App. Phys.* **36**, 153 (1965).
- [105] O.H. Nielsen and R. Martin, *Quantum mechanical theory of stress and force*, *Phys. Rev. B* **32**, 3780 (1985).
- [106] Yu.A. Burenkov, S.P. Nikanorov and A.V. Stepanov, *Elastic properties of germanium*, *Sov. Phys. Solid State (English Transl.)* **12**, 2428 (1940).
- [107] J. Bardeen and W. Shockley, *Deformation Potentials and Mobilities in Non-Polar Crystals*, *Phys. Rev.* **80**, 72 (1950).
- [108] G.L. Bir and G.E. Picus, *Symmetry and Strain-Induced Effects in Semiconductors*, (Wiley, New York 1974).
- [109] F.H. Pollack and M. Cardona, *Piezo-Electroreflectance in Ge, GaAs, and Si*, *Phys. Rev.* **172**, 3 (1968).
- [110] J.D. Wiley, *Semiconductors and Semimetals* **10** (1975).
- [111] B. Kiraly, R.M. Jacobberger, A.J. Mannix, G.P. Campbell, M.J. Bedzyk, M.S. Arnold, M.C. Hersam and N.P. Guisinger, *Electronic and Mechanical Properties of Graphene-Germanium Interfaces Grown by Chemical Vapor Deposition*, *Nano Lett.* **15**, 7414 (2015).
- [112] W.H. Kleiner and L.M. Roth, *Deformation Potential in Germanium from Optical Absorption Lines for Exciton Formation*, *Phys. Rev. Lett.* **2**, 334 (1959).
- [113] L. Laude, F.H. Pollack and M. Cardona, *Effects of Uniaxial Stress on the Indirect Exciton Spectrum of Silicon*, *Phys. Rev. B* **3**, 2623 (1971).
- [114] C.G. Van de Walle and R.M. Martin, *Theoretical calculations of heterojunction discontinuities in the Si/Ge system*, *Phys. Rev. B* **34**, 5621 (1986).